University of Alberta

Fluorescence Detection Schemes for Capillary Electrophoresis

by

Ebbing Pieter de Jong

A thesis submitted to the Faculty of Graduate Studies and Research
in partial fulfillment of the requirements for the degree of

Doctor of Philosophy

Department of Chemistry

Edmonton, Alberta
Spring 2007

Your file Votre référence
ISBN: 978-0-494-29778-0
Our file Notre référence
ISBN: 978-0-494-29778-0

"I would rather be ashes than dust! I would rather that my spark should burn out in a brilliant blaze than it should be stifled by dry-rot. I would rather be a superb meteor, every atom of me in magnificent glow, than a sleepy and permanent planet. The function of man is to live, not to exist. I shall not waste my days trying to prolong them. I shall use my time."

Jack London

ABSTRACT

Capillary electrophoresis (CE) is a widely accepted separation method for biological applications due to its small sample compatibility. Small sample volumes demand high-sensitivity detection, most commonly laser-induced fluorescence (LIF). Typical lasers used in LIF are large and expensive; qualities which are contrary to the nature of CE. This thesis investigates alternative light sources for high-sensitivity fluorescence detection.

The first light source explored was the violet diode laser, emitting 5 mW at 400 nm. Compared to gas-phase lasers typically used for LIF, the violet diode laser is considerably smaller, about half the price, but significantly less powerful. To demonstrate the abilities of the violet diode laser, labelling and detection of the protein myoglobin was performed. The non-fluorescent heme group of myoglobin was replaced with a fluorescent porphyrin. The labelling is unaffected by a 2000-fold excess of bovine serum albumin, a potential interferent, and produces a detection limit of 50 nM for myoglobin.

Another light source with reduced cost and size is a light-emitting diode (LED). At $1 to $25, the cost of an LED is trivial and its size is approximately an order of magnitude smaller than most lasers. The optical properties of LEDs present several challenges due to their large emitter size and highly divergent, polychromatic light output. An epi-fluorescence detection geometry focussed the LED light to a ~ 150 μm spot, slightly larger than the capillary inner channel. The LEDs' polychromatic light gives an extremely high background signal due to scatter of the LED light at the detection wavelength. A bandpass filter between the LED and the capillary reduces this

background signal and increases the signal-to-noise of the detector by a factor of ≥ 70. A detection limit of 3 nM was achieved using $1, low-power LEDs and 3 pM with a $25, high-power LEDs. This level of sensitivity rivals that achieved using gas-phase lasers. The detector was applied to monitoring protein purification as well as DNA separations. DNA was detectable at 40 μg/mL. In sacrificing perhaps an order of magnitude in detection limit, LEDs give two or three orders of magnitude savings in cost, relative to gas-phase lasers.

ACKNOWLEDGEMENTS

I would like to thank Dr. Charles Lucy for his support, patience and dedication to educating his students. Several people made daily life in the department enjoyable, notably Glen, Sarah, Chris, Panos and Donna. I owe many thanks to Dieter Starke, Vincent Bizon and Al Chilton from the machine and electronics shops for all their help in designing, improving and fixing various instrument components. Thanks also to Sandra Marcus for help with DNA sequencing and Wayne Moffat for collecting spectra of filters and LEDs.

Gary Edwards of Polymicro Technologies graciously donated samples of capillary tubing.

Financial support from the University of Alberta and the Natural Sciences and Engineering Research Council of Canada in the form of a research grant and a postgraduate fellowship are gratefully acknowledged.

TABLE OF CONTENTS

CHAPTER ONE. Introduction

Chapter Two. Non-Covalent Labelling of Myoglobin by Reconstitution with a Fluorescent Porphyrin

CHAPTER FIVE. DNA Separations

CHAPTER SIX. Conclusions and Future Work

LIST OF TABLES

LIST OF FIGURES

LIST OF NOMENCLATURE

A	adenine nucleobase
α	selectivity factor
BSA	bovine serum albumin
BGE	background electrolyte
C	cytosine nucleobase
CCD	charge-couple device (camera)
CE / CZE	capillary electrophoresis / capillary zone electrophoresis (interchangeable)
CGE	capillary gel electrophoresis
cIEF	capillary isoelectric focussing
cITP	capillary isotachophoresis
cmc	critical micelle concentration
D	diffusion coefficient
d	(capillary) diameter
DL	detection limit (interchangeable with LOD)
ddNTP	dideoxynucleotide triphosphate
DNA	deoxyribonucleic acid
dNTP	deoxynucleotide triphosphate
DR	dynamic range
E	electric field strength
E_c	energy of the conductance band
EDTA	ethylenediaminetetraacetic acid

E_g	energy gap between the conductance and valence bands
ELFSE	end-labelled free solution electrophoresis
eof	electroosmotic flow
E_v	energy of the valence band
ET	energy transfer
ε_0	permittivity of a vacuum
ε_r	dielectric constant relative to vacuum
f_1, f_2	focal lengths of lenses 1 and 2
FITC	fluorescein isothiocyanate
FRET	Förster (of fluorescence) resonance energy transfer
FWHM	full width at half-maximum
Φ_F	fluorescence quantum yield
G	guanine nucleobase
GFC	gel filtration chromatography
HAc	acetic acid
HEC	hydroxyethylcellulose
HeCd	helium-cadmium laser
HeNe	helium-neon laser
HEPES	4-(2-hydroxyethyl)piperazine-1-ethanesulfonic acid
HPC	hydroxypropylcellulose
HPMC	hydroxypropylmethylcellulose
η	(solvent) viscosity
i.d.	(capillary) inner diameter

IR	infrared
k'	partition coefficient
$\widetilde{k}'$	MEKC retention factor
L	(capillary) length
L_d	(capillary) length to detector
LED	light-emitting diode
LIF	laser-induced fluorescence
l_{inj}	injection length
l_{det}	detection length
LPA	linear poly(acrylamide)
LOD	limit of detection (interchangeable with DL)
$\lambda_{1/2}$	spectral half-width
m	optical magnification of a system
MAPS	γ-methacryloxypropyltrimethoxysilane
MC	methylcellulose
MEKC	micellar electrokinetic chromatography
MES	4-morpholineethanesulfonic acid
M_n	number average molecular weight
M_w	weight average molecular weight
$\Delta\mu$	difference in mobility between two species
μ_{eof}	electoosmotic flow mobility
μ_{ep}	electrophoretic mobility
μ_{net}	net mobility

$\overline{\mu}_{net}$	average net mobility
N	efficiency of separation
n-type	negative-type material
NA	numerical aperture
o.d.	(capillary) outer diameter
OD	optical density
ΔP	pressure difference
p-type	positive-type material
PA	poly(acrylamide)
PAGE	poly(acrylamide) gel electrophoresis
PCR	polymerase chain reaction
PDMA	poly(*N*,*N*-dimethylacrylamide)
PEG	poly(ethylene glycol)
PEO	poly(ethylene oxide)
PMT	photomultiplier tube
PPIX	protoporphyrin IX
PVP	poly(vinyl pyrrolidone)
q	elementary charge
r	(capillary) radius
RNA	ribonucleic acid
R_s	resolution of adjacent peaks
RSD	relative standard deviation
SDS	sodium dodecyl sulfate

SDS-PAGE	sodium dodecyl sulfate polyacrylamide electrophoresis
ssDNA	single-stranded DNA
σ	standard deviation of a Gaussian distribution
σ_{det}	standard deviation due to detector bandbroadening
σ_{diff}	standard deviation due to longitudinal diffusion bandbroadening
σ_{HF}	standard deviation due to hydrodynamic flow bandbroadening
σ_{inj}	standard deviation due to injector bandbroadening
σ_J	standard deviation due to Joule heating bandbroadening
σ_{tot}	total standard deviation due to bandbroadening
T	thymine nucleobase
t	student's t
t_0	eof migration time in MEKC separation
Taq	DNA polymerase enzyme from *Thermus aquaticus*
TBE	tris-borate-EDTA buffer
TE	tris-EDTA buffer
TEMED	*N,N,N',N'*-tetramethylethylenediamine
t_m	analyte migration time
t_{mc}	micelle migration time
t_r	migration time in MEKC separation
tris	tris(hydroxymethyl)aminomethane
UV(/vis)	ultraviolet (/visible) absorbance detection
V	voltage
V_0	built-in voltage

v_{eof}	electroosmotic flow velocity
v_{ep}	electrophoretic velocity
w_b	peak width measured at baseline
ζ	zeta potential of a surface
Zn-PPIX	zinc-protoporphyrin IX complex

CHAPTER ONE. Introduction

1.1 History of Capillary Electrophoresis

Electrophoresis is a separation technique which exploits mobility differences between analytes under the influence of an electric field. From its inception in 1937 by Tiselius, electrophoresis has been used widely in the separation of biomolecules.[1] Tiselius separated serum proteins using a "moving boundary" apparatus. The efficiency of this instrument was limited by Joule heating-induced convection currents, leading future efforts to work with anti-convective supports. Paper electrophoresis of copper-complexed amino acids was performed by Wieland and Fischer[a] in 1948,[2] followed by starch[3-5] and agarose[6] support media. Again, amino acids and serum proteins were separated in these studies. Crosslinked polyacrylamide gels were eventually developed, and now polyacrylamide gel electrophoresis (PAGE) represents one of the most widely used biochemical techniques.[7] Joule (resistive) heating (Section 1.2.5.1) continues to hinder the maximum applicable voltage for these separations, leading to long run times of up to 12 hours. High-performance zone electrophoresis was first performed in 0.2 mm tubes in 1979,[8] but even better efficiency was observed in 1981 when true capillary-dimension glass tubes were made.[9] With an inner diameter of 75 μm, these capillaries were able to effectively dissipate the Joule heating, and allowed application of up to 30

---

[a] It is interesting to note that this article has been consistently mis-referenced. The authors have published two papers that start on the same page of the journal. The first article has been cited 236 times. The second article, the only one to discuss paper electrophoresis, has never been cited.

kV to induce separation. Commercial availability of high-quality fused silica capillary tubing with inner diameters as small as 2 μm has made capillary electrophoresis (CE) a relatively inexpensive and simple analytical method. Today the vast majority of CE is performed in capillaries of 10 – 100 μm inner diameter. Capillary electrophoresis plays an important role in the separation of biopolymers, as was the case in early electrophoretic experiments. But CE has since found use in separating small molecules (drugs,[10] vitamins,[11] metabolites[12]) and inorganic ions.[13, 14]

CE is generally viewed as a relatively new analytical technique. This perception is due largely to a period of disuse caused by a technological bottleneck in the manufacturing of appropriate capillary tubing. However, the role of CE has clearly reached the fifth "life stage" according to Laitinen's "Seven Ages of an Analytical Method".[15] In the fourth stage, a fundamental understanding of principle and mechanism was developed. With this knowledge base, the fifth stage commences, putting CE in position to tackle an ever-widening scope of applications.

1.2 Principles of Capillary Electrophoresis

1.2.1 CE Instrumentation

The instrumentation for CE is rather simple, as shown in Figure 1.1. A typical instrument consists of a carousel of sample vials, a cartridge which holds the capillary and allows for coolant to flow over the capillary and two electrodes connected to a high-voltage power supply and a detector. The detectors used in CE will be discussed in Section 1.3. The capillary tubing used in CE is typically made of high-purity fused silica,

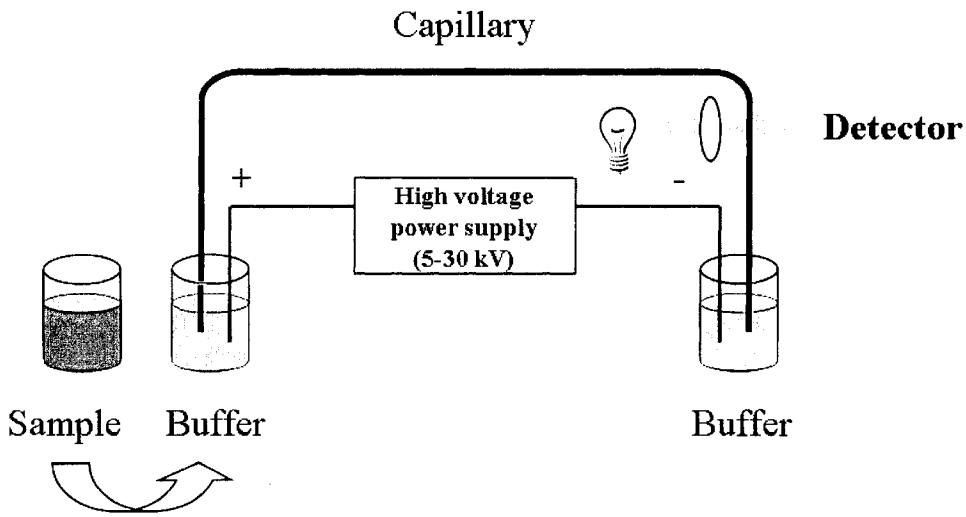

Figure 1.1 Schematic of CE instrumentation. The capillary is first filled with buffer, then a small injection of sample is made. Leads from the high voltage power supply are placed in the buffer vials at the inlet and outlet ends of the capillary. Shown here is an absorbance detector.

coated with a ~ 5 μm outer coating of polyimide. The polyimide allows the fused silica to bend without breaking. Capillaries typically have an inner diameter (i.d.) of 10 – 100 μm and outer diameter (o.d.) of 150 or 365 μm.

First, the capillary is filled with a buffer solution, also called the background electrolyte (BGE). Then a small injection of sample is made at the inlet end by either applying pressure (hydrodynamic injection) or voltage (electrokinetic injection) with the sample vial in place. The injected volume is typically between 1-10 nL. Both ends of the capillary are placed in vials containing the buffer solution and the electrodes. Application of voltage commences electrophoresis, under an electric field of 100 to 1000 V/cm. Electroosmosis and electrophoresis govern the motion of analyte molecules in the separation.

1.2.2 Electroosmotic Flow[16, 17]

A phenomenon whereby bulk flow of liquid occurs, called electroosmotic flow (eof), is observed in electrophoretic separations. Electroosmotic flow is relevant only in capillary-scale separations due to the high field strengths used and low viscosity of the solution. The electroosmotic flow is caused by the charged capillary inner surface. In a fused silica capillary, as is used almost exclusively in capillary electrophoresis, Si-OH bonds at the surface are deprotonated above pH 5.3, giving the surface a negative charge. Cations will be strongly attracted to the negatively charged surface, giving rise to an electrical double layer. There exists a layer of immobilized, unsolvated cations, making up the Inner Helmholtz plane. Outside this layer, cations are solvated in the Outer Helmholtz plane. Together, the Inner and Outer Helmholtz planes are also referred to as

the Stern Layer. Beyond the Outer Helmholtz plane is the diffuse layer where both hydrated cations and anions are found, with an excess of cations necessary to maintain electroneutrality. Finally, beyond the diffuse layer, the bulk solution is found where cations and anions exist in equal proportions. Under the influence of an electric field, the hydrated cations in the diffuse layer migrate towards the cathode. Since the cations are fully solvated, their movement results in bulk flow through the capillary. The immobilized cations at the capillary surface do not migrate and consequently there is no flow of solution at the surface. The flow rate increases with radial distance from the capillary surface. The electroosmotic flow reaches 99% of its full value at a radial distance of just 14 nm for a typical buffer solution.[16] The electroosmotic flow profile is essentially flat, which avoids bandbroadening issues seen in pressure-driven flow techniques. The linear electroosmotic flow rate (cm s^{-1}) is given by

$$v_{eof} = \mu_{eof} E = \frac{\mu_{eof} V}{L} \qquad \textbf{1.1}$$

where μ_{eof} is the electroosmotic mobility (cm^2 V^{-1} s^{-1}), E is the electric field strength (V cm^{-1}), V is the applied voltage (V) and L is the total length of the capillary (cm). The electroosmotic mobility is governed by the von Smoluchowski equation:[18]

$$\mu_{eof} = -\frac{\varepsilon_0 \varepsilon_r \zeta}{\eta} \qquad \textbf{1.2}$$

where ε_0 is the permittivity of a vacuum (C^2 N^{-1} m^{-2}), ε_r is the dielectric constant of the medium relative to ε_0 (unitless), ζ is the zeta potential of the surface (V), and η is the viscosity of the solvent (Pa s). The most accessible variable in controlling the electroosmotic mobility is the zeta potential. The zeta potential is the potential of the capillary surface, measured at the plane of shear. This potential results from the charge

density on the silica surface, and can be experimentally controlled by the pH of the solution. The weakly acidic silanol groups ($pK_a \sim 5.3$)[19] can be deprotonated by rinsing the capillary with concentrated base solution, yielding a high zeta potential and thus, a strong electroosmotic flow. A typical value for μ_{eof} is $\sim 5 \times 10^{-4}$ cm^2 V^{-1} s^{-1} at pH 8.[20] A plot of eof versus pH resembles a titration curve, with a sigmoidal increase in eof centered about pH 5.3. Due to the heterogeneity of surface silanol species (bridging, geminal, vicinal), this sigmoidal behaviour is significantly broadened. The electrophoretic mobility of an ionizable analyte ion is also pH-dependent, as described below.

1.2.3 Electrophoretic Mobility

As with electroosmotic mobility, the electrophoretic mobility of an analyte is calculated as

$$v_{ep} = \mu_{ep} E = \frac{\mu_{ep} V}{L} \qquad \textbf{1.3}$$

where the subscript *ep* denotes electrophoretic, and all other terms have the same meaning and units as in Section 1.2.2.

A charged particle in solution undergoing electrophoresis experiences two forces: electrostatic attraction or repulsion in the electric field and frictional drag. Under steady-state conditions these forces have equal magnitudes but in opposite directions, leading to

$$qE = 6\pi\eta r v_{ep} \qquad \textbf{1.4}$$

where q is the net charge of the ion (C), and r is the radius of the ion (cm). Inserting equation 1.4 into equation 1.3 yields an expression for the electrophoretic mobility of an ion:

$$\mu_{ep} = \frac{q}{6\pi\eta r} \qquad \textbf{1.5}$$

Similar to electroosmotic flow, a plot of μ_{ep} versus pH for a weak acid also displays a sigmoidal dependence. The difference in electrophoretic mobility of analytes is used to achieve a separation. The net mobility (also termed apparent mobility, μ_a) of an analyte is

$$\mu_{net} = \mu_{eof} + \mu_{ep} = \frac{L_d L}{V t_m} \qquad \textbf{1.6}$$

where L_d is the length of the capillary to the detection point (cm), L is the total length of the capillary and t_m is the migration time of an analyte (s). Net mobility must, of course, be in the direction of the detector. Few analytes, except for multiply charged or small ions, have sufficient electrophoretic mobility to overcome the strong eof of a bare silica capillary.

1.2.4 Separation Efficiency

Efficiency, as defined in separation science, is a measure of a technique's ability to produce sharp peaks. One parameter which is used to calculate the efficiency of a peak is its width (measured in length, volume or time). Assuming a Gaussian peak shape, the baseline width, w_b, of a peak is given by

$$w_b = 4\sigma \qquad \textbf{1.7}$$

where σ is the standard deviation of the Gaussian profile. Under ideal conditions the only source of bandbroadening in CE is longitudinal diffusion, which affects peak width as

$$\sigma_{diff}^2 = 2Dt_m = \frac{2DL_d L}{V\mu_{net}} \quad \textbf{1.8}$$

where D is the diffusion coefficient of the analyte. Note that equation 1.6 has been inserted to obtain the right side of equation 1.8. Efficiency, N (number of theoretical plates), is calculated by equation 1.9,

$$N = \left(\frac{L_d}{\sigma}\right)^2 = 16\left(\frac{t_m}{w_b}\right)^2 \quad \textbf{1.9}$$

Inserting equation 1.8 into 1.9 gives

$$N = \frac{\mu_{net} V L_d}{2DL} = \frac{{L_d}^2}{2Dt_m} \quad \textbf{1.10}$$

Equation 1.10 makes it clear that a rapid separation allows little time for diffusion bandbroadening to occur. More importantly, the right side of this equation shows the maximum theoretical efficiency that can be obtained, assuming no other sources of bandbroadening are present. Using the citrate anion (D = 6.6 × 10^{-5} cm^2 s^{-1}) as an example and assuming L_d of 27 cm and t_m of 5 min, we see that this a CE separation is capable of achieving up to 184,000 theoretical plates. Indeed a separation resulting in less than 100,000 plates is cause for concern in CE.[21] Resolution is another important parameter in a separation, which indicates how well two peaks are separated. An efficient separation improves the resolution (R_s) as

$$R_s = 0.25\sqrt{N}\frac{\Delta\mu}{\bar{\mu}_{net}} \quad \textbf{1.11}$$

where $\Delta\mu$ is the difference in mobility of two analytes and $\overline{\mu}_{net}$ is the average net mobility of the two analytes. Not surprisingly, the resolution is proportional to the difference in mobility between two analytes.

1.2.5 Bandbroadening in CE

Various phenomena can cause broadening of the injected analyte zone in CE, although in an ideal system only longitudinal diffusion is present. Bandbroadening in CE, as in all separation methods, is quantified by the standard deviation of the electrophoretic peaks, seen in equation 1.7. The overall peak width is simply the sum of variances caused by different broadening mechanisms:

$$\sigma_{tot}^2 = \sigma_{diff}^2 + \sigma_{inj}^2 + \sigma_{\det}^2 + \sigma_J^2 + \sigma_{ads}^2 + \sigma_{HF}^2 + \ldots \qquad \textbf{1.12}$$

where σ^2 is the variance and the subscripts *tot*, *diff*, *inj*, *det*, *J*, *ads* and *HF* refer to total, longitudinal diffusion, injector, detector, Joule heating, adsorption and hydrodynamic flow contributions. Joule heating and detector bandbroadening are discussed in Sections 1.2.5.1 and 1.2.5.2, whereas the remaining sources of bandbroadening are discussed below.

Equation 1.8 defines bandbroadening resulting from longitudinal diffusion. Injector bandbroadening can be considered an avoidable error in CE. When an excessively long plug of analyte is injected (and in the absence of stacking effects), the width of the analyte band at the detector is affected according to

$$\sigma_{inj}^2 = l_{inj}^2 / 12 \qquad \textbf{1.13}$$

where l_{inj} (m) is the length of the injected plug. Injection volume (or length) can be calculated from the Hagen-Poiseuille Law:

$$V = \frac{\pi d^4 \Delta P t}{128 \eta L} \qquad \textbf{1.14}$$

where ΔP is the pressure difference across the capillary (Pa), d is the capillary (inner) diameter (m), t is the time of injection (s), and η and L have their previous meaning.

Sample adsorption in CE occurs due to the electrostatic attraction between a positively-charged molecule (or a positively-charged region of a macromolecule) and the negatively-charged capillary silica surface. As this adsorption retards the migration of an analyte, it results in bandbroadening in the form of peak tailing. In some cases, the adsorption is so severe that complete, irreversible adsorption of a species occurs. The Lucy group has worked extensively on developing coatings which prevent the adsorption of basic drugs and proteins.[22-27]

Hydrodynamic flow, also an avoidable error, can arise in CE if the liquid level of the inlet and outlet vials differs. This laminar flow profile results in zone broadening. Lucy *et al.* have expressed these and other parameters causing bandbroadening as tolerable error limits.[21]

1.2.5.1 Joule Heating

Joule heating, as mentioned in Section 1.1, limits the maximum applicable voltage in an electrophoretic separation. The heating arises from the resistance to passage of electrical current across the capillary. The resulting heat is dissipated at the capillary walls, leading to a radial temperature gradient. Because aqueous solvent viscosity

decreases by approximately 2.7% per degree Celsius,[28] the viscosity gradient allows molecules in the center of the capillary to migrate more rapidly (see Equation 1.5). The magnitude of the generated temperature gradient is proportional to the square of capillary i.d., indicating that narrower capillaries are significantly less susceptible to Joule heating.

An Ohm's plot can be used to determine whether Joule heating is significant under a given set of experimental conditions. Plotting the observed steady-state current as a function of applied voltage should result in a linear relationship. However, in the presence of Joule heating, positive deviation from this linear relationship is observed. To combat Joule heating, most commercial instruments have a cooling system, where either air or a CFC refrigerant continuously cools the capillary (Section 1.2.1). The instrument used in this work was devoid of such thermostatting (Section 2.2.2).

1.2.5.2 Detector Bandbroadening

Detector bandbroadening is investigated in Sections 3.3.1 and throughout Chapter Four. When the detector samples an excessively large length along the capillary, detector bandbroadening becomes significant. An analyte moving through this large detection window will be detected for a long period of time, thereby expanding the peak width (in units of time, distance, or volume). This broadening is illustrated in Figure 1.2. The equation for detector bandbroadening is identical to that for injector bandbroadening except that the subscripts should read *det*. The use of an infinitely narrow detector region would appear ideal. However, as detectors have a finite response time, a narrow detection region allows less integration time of a fluorescent signal, resulting in lower

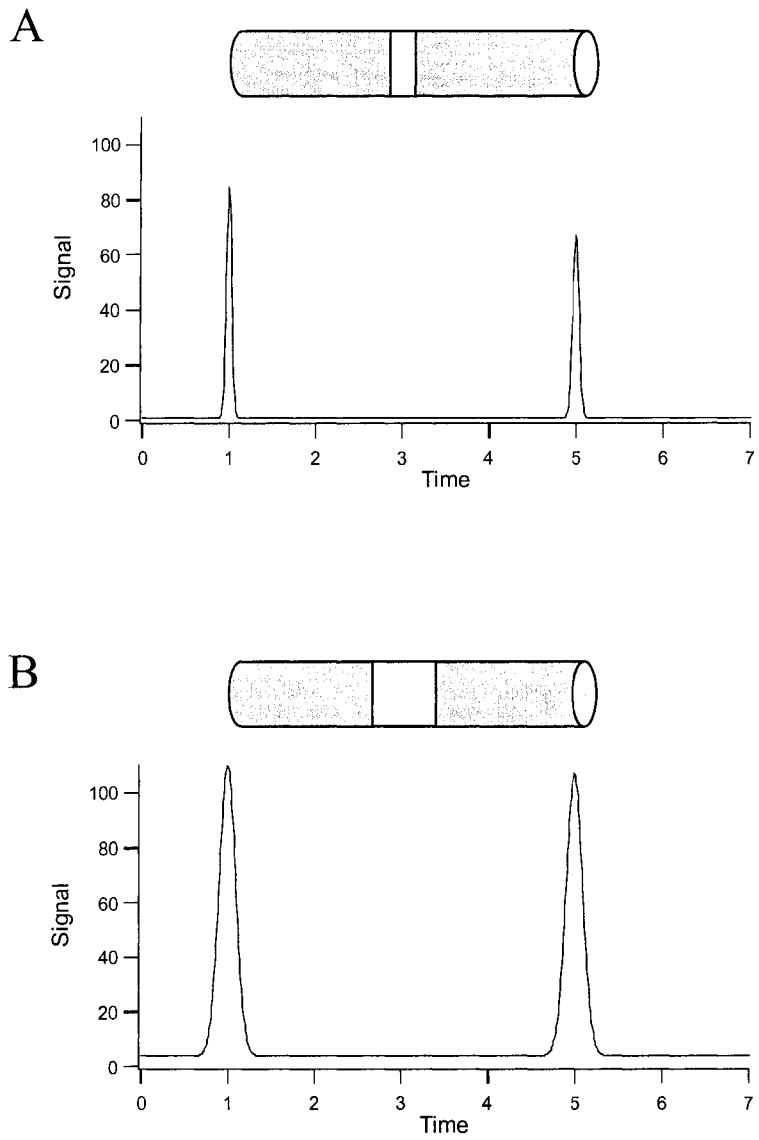

Figure 1.2 Illustration of detector bandbroadening. Peak widths and areas are modelled for two different detector lengths, and the resulting separation is shown below the cartoon of the capillary. The detector width in panel B is four times that in panel A. Note that peak widths and heights are to scale.

sensitivity (see Equation 1.17 below). Consequently, the largest detection zone which does not produce any appreciable bandbroadening is ideal.

1.2.6 Separation Modes

1.2.6.1 CE Separation Modes

Capillary electrophoresis instrumentation can be used in a variety of operational modes, often with little or no changes required to the hardware or operational procedures. Among the most common modes are capillary zone electrophoresis (CZE),[9] micellar electrokinetic chromatography (MEKC),[29] capillary isoelectric focusing (cIEF),[30] capillary isotachophoresis (cITP)[31, 32] and capillary gel electrophoresis (CGE).[33] Isoelectric focusing and isotachophoresis were not used in this thesis, and will not be discussed here.

1.2.6.1.1 Capillary Zone Electrophoresis (CZE)

The simplest of the separation modes listed above, CZE requires only a buffer-filled capillary. After injection of a sample, an electric field is applied and the net mobility of the analytes carries them towards the detector. The electroosmotic mobility is dictated by the choice of buffer, while the electrophoretic mobility of the analytes is determined by their size to charge ratio (Equation 1.5). Since the eof mobility is usually larger than the electrophoretic mobility, cations, neutrals and anions are all swept toward the detector. The bulk flow can be directed towards the detector by using a positive bias at the inlet vial (anode) and a negative bias at the outlet vial (cathode). This bias can be

reversed, if necessary. Figure 1.3A shows the net mobility of the species in a hypothetical separation, and Figure 1.3B represents the resulting electropherogram. Note that no separation is achieved between the neutral species. Greatest speed is achieved for cations which migrate with the eof (co-eof; equation 1.6) and greatest resolution is achieve for ions which migrate against the eof (counter-eof; equation 1.11).

1.2.6.1.2 Micellar Electrokinetic Chromatography (MEKC)

MEKC is a hybrid technique encompassing elements from liquid chromatography and electrophoresis. The primary benefit of MEKC compared to CE is that it allows the separation of neutral molecules. In a MEKC separation, a surfactant is added to the BGE at a concentration above its critical micelle concentration (cmc). A typical example is sodium dodecyl sulfate (SDS) which forms a negatively-charged micelle. Upon applying a voltage to the capillary, the SDS micelles migrate slowly against the eof. The micelles soon enter the plug of analyte solution, where the analytes partition between the (usually) aqueous mobile phase and the hydrophobic core of the micelles. A neutral analyte that partitions strongly into the micelles will display a counter-eof mobility and a different net mobility compared to an analyte which partitions weakly into the micelles. Similar to the expression used in liquid chromatography, one can define a retention factor $\tilde{k}'$,

$$\tilde{k}' = \frac{t_r - t_0}{t_0\left(1 - \frac{t_r}{t_{mc}}\right)} \qquad \textbf{1.15}$$

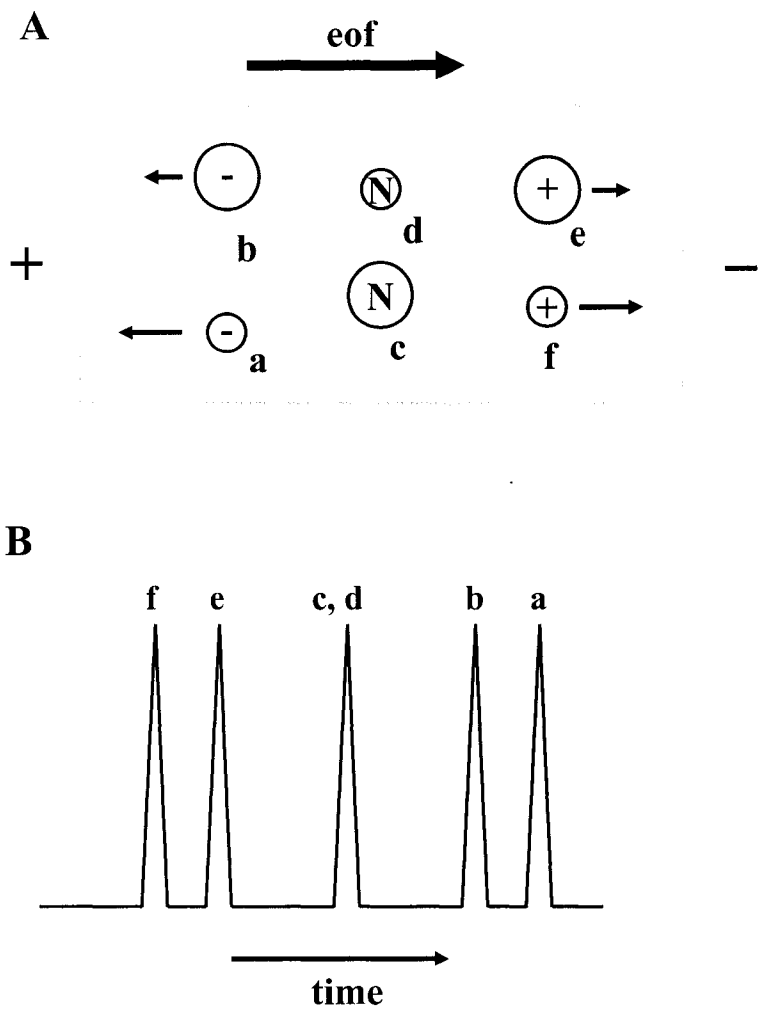

Figure 1.3 Theoretical CE separation, showing small and large anions, neutrals, and cations. Top panel, A, displays the species' net mobilities (light arrows) and eof flow (heavy arrow) inside a capillary. Bottom panel, B, illustrates the resulting electropherogram.

where t_r is the migration time of an analyte, t_0 is the migration time of the electroosmotic flow (measured using an unretained analyte) and t_{mc} is the migration time of the micelles. Resolution in MEKC is given by

$$R_s = \left(\frac{\sqrt{N}}{4}\right)\left(\frac{\alpha-1}{\alpha}\right)\left(\frac{\tilde{k}_2'}{\tilde{k}_2'+1}\right)\left(\frac{1-\frac{t_0}{t_{mc}}}{1-\left(\frac{t_0}{t_{mc}}\right)\tilde{k}_1'}\right) \qquad \textbf{1.16}$$

where R_s is the resolution and α is the separation factor $\tilde{k}_2' / \tilde{k}_1'$. The separation range in MEKC can be adjusted by altering the concentration of micelles, the nature of the surfactant, or by adding an organic solvent to the BGE. MEKC can also be used merely to sweep a low-mobility analyte towards the detector more rapidly (Section 3.2.5).

1.2.6.1.3 Capillary Gel Electrophoresis (CGE)

Capillary gel electrophoresis (CGE) is used for size-based separations of relatively large molecules, usually biomolecules. Many synthetic polymers are uncharged, and can not be separated by CGE. DNA however, serves as an appropriate example to explain CGE separations. All lengths of DNA have the same mass-to-charge ratio which, under denaturing conditions, is proportional to their size-to-charge ratio. Consequently CZE would be unable to separate DNA and instead, a size-based separation is necessary. By filling the capillary with a chemically crosslinked gel or a physically entangled gel (Section 5.1.5), larger molecules are retarded which gives rise to a separation.[34] CGE separations are usually performed in the absence of eof. In contrast to DNA, proteins display a range of masses and pH-dependent charges. However, in the

presence of a sub-micellar concentration of SDS, all proteins will adsorb SDS to give a constant mass-to-charge ratio. Since the SDS denatures proteins, their mass-to-charge is proportional to their size-to-charge ratio. In this way, so-called SDS-PAGE can separate proteins based on their size.[33] CGE is described in significantly more detail in Sections 5.1.3 and 5.1.5.

1.2.6.2 Other Separation Techniques Used

Gel filtration chromatography (GFC) is generally not performed as a capillary-scale technique. GFC is a size-based separation method where fractionation occurs through the permeation of smaller molecules into the pores of a stationary phase.[35] The stationary phase consists of inert particles with a very tightly controlled pore size. Small molecules can enter all the pores they encounter during their transit through the column. Exceedingly large molecules can not enter any of the pores, and are the first to elute with the mobile phase. Intermediate size molecules sample some fraction of the pores, and elute in order of decreasing size, followed by the small molecules. Gel filtration chromatography is commonly used to purify or de-salt proteins. It should be noted however, that GFC is in fact not chromatography since, ideally, there are no interactions between the analyte and the stationary phase. GFC is employed in Section 4.2.4.

1.3 Detection in CE

A number of detection methods are possible for CE. By far the most commonly used method is UV/vis absorbance detection.[36] Absorbance detection owes its popularity

to the fact that it is a universal detection method which is relatively inexpensive and extremely simple. The primary disadvantage of absorbance detection in CE is its sensitivity. An absorbance signal is proportional to the path length of the light interacting with the sample. In CE, this path length is the capillary i.d., or 10 – 100 μm. This short path length results in concentration limits of detection in the range of 10^{-5} to 10^{-6} M.[37] The next most common technique is fluorescence detection, discussed in Section 1.3.1. Other optical detection techniques include indirect absorbance and fluorescence detection, (electro)chemiluminescence, refractive index, and thermal lens detection. Non-optical techniques include electrochemical (potentiometric, amperometric and conductivity)[38] and mass spectrometric detection.[39] Since fluorescence was the sole detection method used in this thesis, only this technique will be discussed in detail.

1.3.1 Fluorescence Detection

The phenomenon of fluorescence was first described by Sir John F.W. Herschel, as he noticed a blue glow from a solution of quinine exposed to sunlight.[40] A Jabłoński diagram (Figure 1.4) can be used to describe the fluorescence process. The energy levels in a Jabłoński diagram are singlet (S_0, S_1...) and triplet (T_1) electronic energy levels, and the vibrational levels therein (v = 0, 1, 2...). The cycle begins with a ground-state molecule (S_0, v = 0) absorbing a photon of precisely the correct energy to excite the molecule to a higher electronic energy level ($S_{>0}$; fs time scale). This molecule can be excited into a number of vibrational levels within a number of excited electronic states. For simplicity, only the ground and first excited electronic states (S_0 and S_1) will be considered here. Vibrational relaxation to the lowest vibrational state within the first

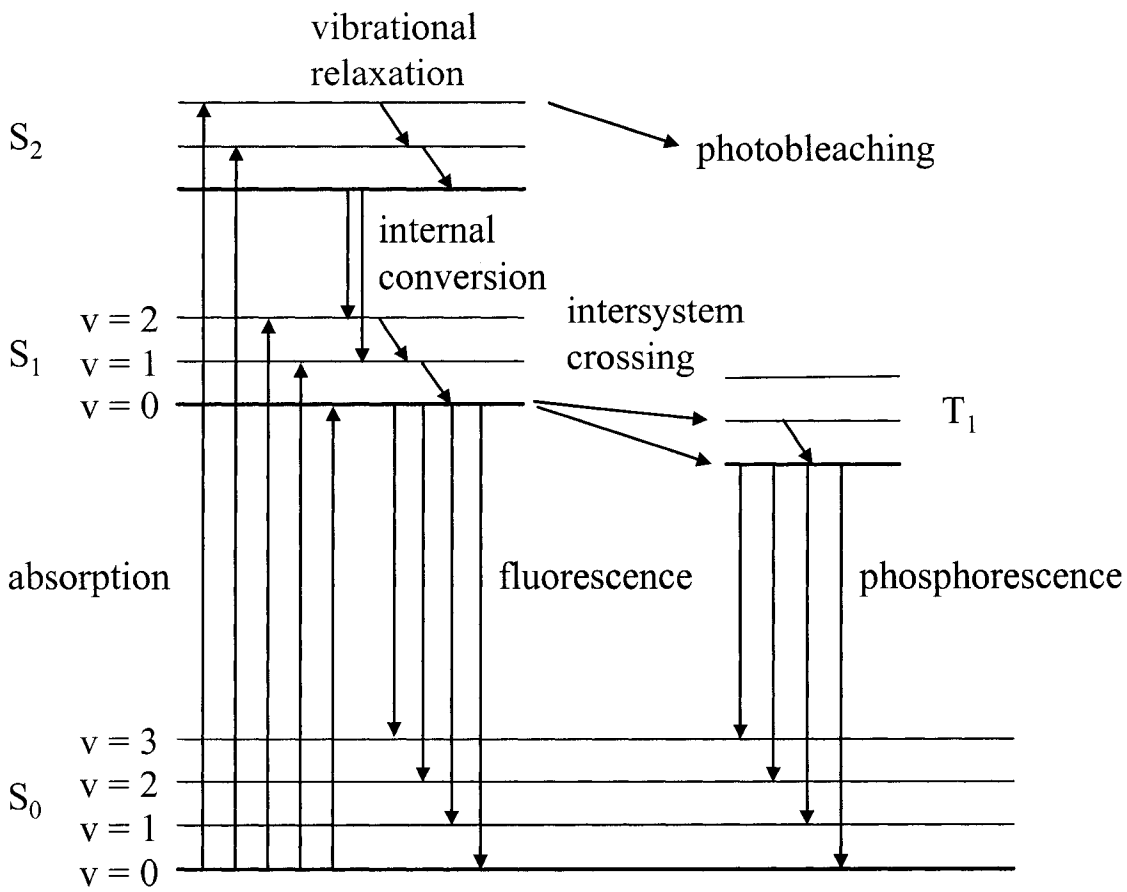

Figure 1.4 Jabłoński diagram of the fluorescence process. S_0, S_1, S_2 and T_1 are singlet and triplet electronic states, with superimposed vibrational levels. The photophysical processes relevant to fluorescence are absorption, vibrational relaxation, internal conversion and fluorescence.

electronic excited state (S_1, v = 0) occurs on the order of picoseconds. Fluorescence is the spontaneous emission of a photon by the excited molecule, as it returns to the ground electronic state. Since energy is lost during vibrational relaxation, the emitted fluorescent light has a longer wavelength than the excitation light. For a typical fluorophore (fluorescein), the fluorescence lifetime is 3.8 ns. This energy or wavelength shift is known as the Stokes' shift.[41] This cycle can be repeated until the fluorophore undergoes a photoinduced chemical reaction, converting it to a nonfluorescent species. This destructive process is known as photobleaching. Note that a number of other photophysical processes from Figure 1.4 are not discussed, as they rarely occur for a highly fluorescent molecule.

Fluorescence detection is accomplished by exciting the molecule of interest at or near its optimum excitation wavelength and observing its emission at a longer wavelength. With appropriate spectral filtering, fluorescence can yield high selectivity but more importantly, extremely low limits of detection, below 10^{-13} M.[37] Since excitation and emission occur at different wavelengths, emission is viewed against a dark or zero background. Sensitive photodetectors can greatly enhance a weak emission signal. However, a fundamental limitation to fluorescence detection is the difficulty in collecting all the emitted light. Fluorescence emission occurs in all directions, whereas one can only conveniently collect light at a chosen direction, typically giving 1 -10% collection efficiency.[42, 43] Like absorbance detection, fluorescence signal intensity, I, is directly proportional to the fluorophore concentration, c,

$$I = 2.3K'\varepsilon bcP_0 \qquad \textbf{1.17}$$

where K' is a constant related to the instrument and the fluorophore, ε is the molar extinction coefficient of the fluorophore, b is the path length of the excitation light, and P_0 is the incident light power.[44] Unlike in absorbance detection, increasing P_0 can be used to increase the fluorescence signal, but only until saturation of the fluorophore or photobleaching become significant. Nevertheless, the use of high- power light sources is usually beneficial in fluorescence detection.

1.3.1.1 Laser-Induced Fluorescence (LIF)

Johnson and Landers have written an excellent review article on the use of laser-induced fluorescence in CE.[45] However, a number of groups have made significant contributions to the field, and deserve recognition here. The Zare group at Stanford was the first to show LIF detection for CE, using a HeCd laser.[46] The Dovichi group while at the University of Alberta was responsible for several seminal papers on the use of sheath flow (see Chapter 4) detection for CE using an argon-ion,[43] or HeNe laser.[47] Yeung and co-workers at Iowa State are also leaders in the field, using the argon-ion laser both in the visible[48] and UV.[49] Concentration detection limits, in the absence of time-gating signal collection, are typically in the range of 10^{-10} to 10^{-13} M.

Spectrally, lasers are nearly the perfect light source for fluorescence measurements. Their high power, collimated, monochromatic light allows for efficient fluorescence excitation, beam expansion or reduction, and lasers require minimal spectral filtering. The only shortcoming of a laser's spectral properties is its fixed wavelength. In many cases, fluorophores are designed to match a laser wavelength (e.g., naphthalene dicarboxaldehyde (NDA) was created to match the 442 nm line of the HeCd laser, and 3-

(2-furoyl)quinoline-2-carboxaldehyde (FQ) was synthesized to match the 488 nm line of the argon ion laser). This is essentially a retrofitting, which is seldom the most efficient approach. A tuneable light source that delivers all its power at a desired wavelength would be ideal.

The spectral properties aside, lasers suffer from a number of other disadvantages in instrumental analysis. Lasers are relatively expensive light sources, often costing tens of thousands of dollars, with a lifetime of only several thousand hours. Gas-phase or mixed gas-solid lasers are bulky and require large amounts of power to operate. Furthermore, gas-phase lasers have a relatively unstable power output (1% noise).[50] This power instability leads to baseline noise in a fluorescence measurement which is detrimental to limits of detection.

Diode lasers (alternatively called laser diodes) are very much comparable to gas-phase lasers. Diode lasers consist of a light-emitting diode with polished surfaces to increase internal reflection. This internal reflection provides the lasing action, but since the diode is side-emitting, the laser emits an elliptical beam of approximately $8 \times 25°$. Diode lasers are almost always sold with collimating optics, although the beam from a diode laser can never be considered a point source, as is the case for gas-phase lasers. The emitted power of diode lasers is remarkably similar to gas-phase lasers. Typical powers range from 5 – 200 mW in the blue or violet region, up to 10 mW in the green and up to 2000 mW in the red and infrared. Diode lasers consume significantly less power than gas-phase lasers and are also much smaller (1.5 to 8 times smaller in each dimension). Finally, the cost of diode lasers is lower than that of gas-phase lasers, but only marginally. An argon-ion laser costs at least $7300, a violet or blue diode lasers

costs $5000, and green diode lasers cost ~ $1000.[51] This seems expensive considering a laser pointer, containing a red diode laser, is available for as little as $5. The additional cost of research-grade diode lasers appears to stem from improved collimating optics, a more stable power supply and active cooling. Active cooling, usually in the form of a fan or large heat sink, is important because the lasing threshold current of diode lasers is sensitive to temperature, as is the slope of the power-current curve (better known as slope efficiency). Consequently, tight control over the device's temperature is needed in order to achieve reproducible power output for a given current. A home-built heat sink was constructed for a violet diode laser (Figure 1.5), which was used in Chapter Two.

1.3.1.2 Light-Emitting Diodes as a Light Source

Light-emitting diodes (LEDs) were first reported in 1962 by the IBM Company.[52] These early GaAs devices produced a peak wavelength of 842 nm and initially operated only in pulsed mode at liquid nitrogen temperatures. Today, LEDs can operate continuously at room temperature, although the rapid switch-on time of LEDs (<4 ns FWHM) makes them useful in pulsed measurements as well.[53, 54] The global market for high brightness LEDs is currently 4.13 billion US$, based on their use in mobile phones and computers, automotive lighting, televisions and signage. Further applications in architectural lighting, water treatment and surgical sterilizations are envisioned.[55] Vast improvements in LED output power and colour options have been made, especially with the introduction of GaInN as a semiconductor material by Nichia. This latest innovation has allowed for blue LEDs and similarly, for blue or violet diode lasers.

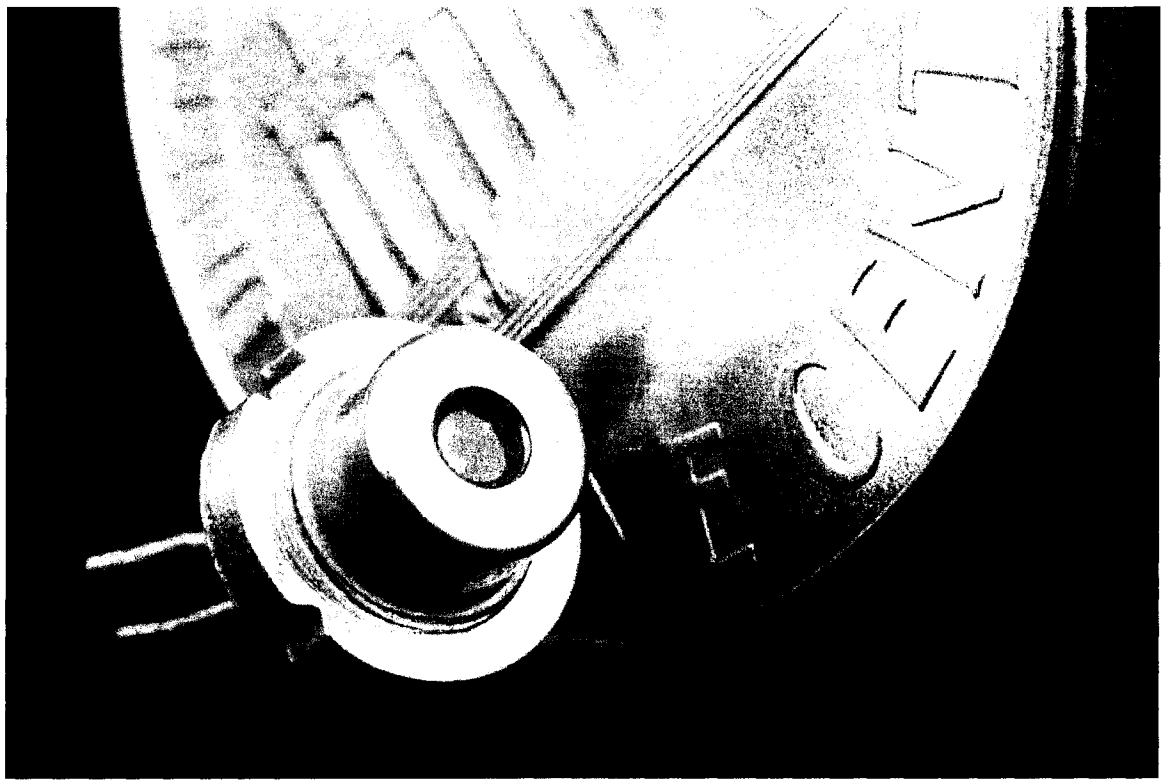

Figure 1.5 Picture of a diode laser. This diode is packaged with electrical leads, but without collimating optics or a cooling system.

A simplified LED band diagram, pictured in Figure 1.6, consists of a semiconductor device with a *pn* junction. The right side of the device is the negatively-doped, or *n*-type material. The "+" superscript denotes that the *n*-side is more heavily doped than the left, *p*-side. Closed circles represent electrons and open circles represent holes. Electron energy increases along the *y*-axis. E_c, E_v and E_g refer to the energy of the conduction band, the valence band, and the band gap. All arguments about electrons and holes are, for our purposes, equal (but in opposite directions) and thus the discussion will focus simply on the electrons. Electrons in the *n*-side diffuse towards the *p*-side, but are prevented by the "built-in voltage", V_0. Upon applying an external voltage to the device, the electrons have sufficient energy to diffuse or be injected into the *p*-type material. Recombination of electrons and holes leads to spontaneous emission of photons with energy approximately equal to the band gap energy.[56] Due to the thermal energy distribution of the electrons, the light emission profile exhibits a full width at half maximum (FWHM) of approximately 1.8 kT.[57] A typical value for an LED's spectral bandwidth, $\lambda_{½}$, is 30 nm.

LED chips are housed in an epoxy dome. This dome protects the chip and the electrodes, but also improves light extraction. In a simple, rectangular LED chip, total internal reflection occurs for photons travelling nearly parallel to the chip surface. Extraction efficiency is defined as the ratio of the number of photons emitted into free space per photon emitted by the LED chip. For an uncoated LED chip, this extraction efficiency is poor at ~10%. However, the epoxy has a much higher refractive index than air (1.4 to 1.8, *vs.* ~1), allowing a wider escape angle and thus increasing the extraction efficiency to ~27%.[58] The epoxy dome can also be used to control the divergence of the

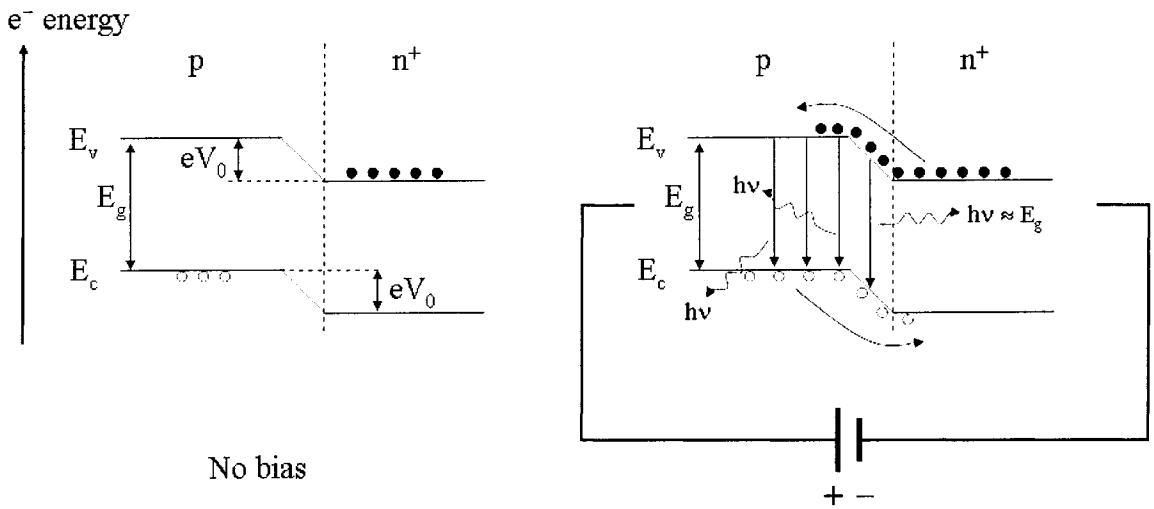

Figure 1.6 Energy level diagram of a *pn* junction in an LED at rest (left) and under forward bias (right). Filled circles represent electrons and open circles represent holes. At rest there is no net movement of charge carriers. Under forward bias, electrons are able to cross the junction and combine with a hole to produce a photon. This light emission is spontaneous, and results in incoherent light emission.

LED light. A planar LED surface emits with a Lambertian profile with a maximum emission intensity perpendicular to the surface. The emission intensity decreases at greater angles, dropping to 50% of the maximum intensity at 60°. A hemispherical epoxy dome creates uniform emission intensity at all angles. The most common shape of epoxy dome is a parabolic profile. Depending on its shape, the parabolic dome can narrow the emitted light to give 50% maximum intensity at 10 - 30° (Figure 1.7).

The lighting market is driving LED manufacturers to increase the light output of their LED packages. In order to increase the light output from a single LED, Luxeon and other companies have made their LEDs with a significantly larger emitting chip (Section 4.3.2). As a result of the larger emitter size and ability to accept greater current, these LEDs can produce up to 750 mW of power – a vast improvement over the 5 mW produced by a standard LED chip. Aside from the improved output power, LEDs with a larger emitter differ from standard LEDs in a number of ways. First, large LED chips can accept up to 1500 mA, compared to 30 mA for standard LEDs. Dissipation of such a high current generates a significant amount of heat (up to 5 W), and high-power LEDs must be operated with a heat sink to prevent irreversible damage to the chip. Standard LEDs dissipate on the order of 0.1 W and do not require a heat sink. With the exception of this heat sink, high-power LEDs are essentially the same size as standard LEDs, as most of the volume comes from packaging. LEDs occupy a very small volume, perhaps 1 × 3 × 3 cm plus a typical AC converter power supply. Another consequence of the larger emitter chip is that high-power LEDs cost <US$ 20, compared to < US$ 1 for low-power LEDs.

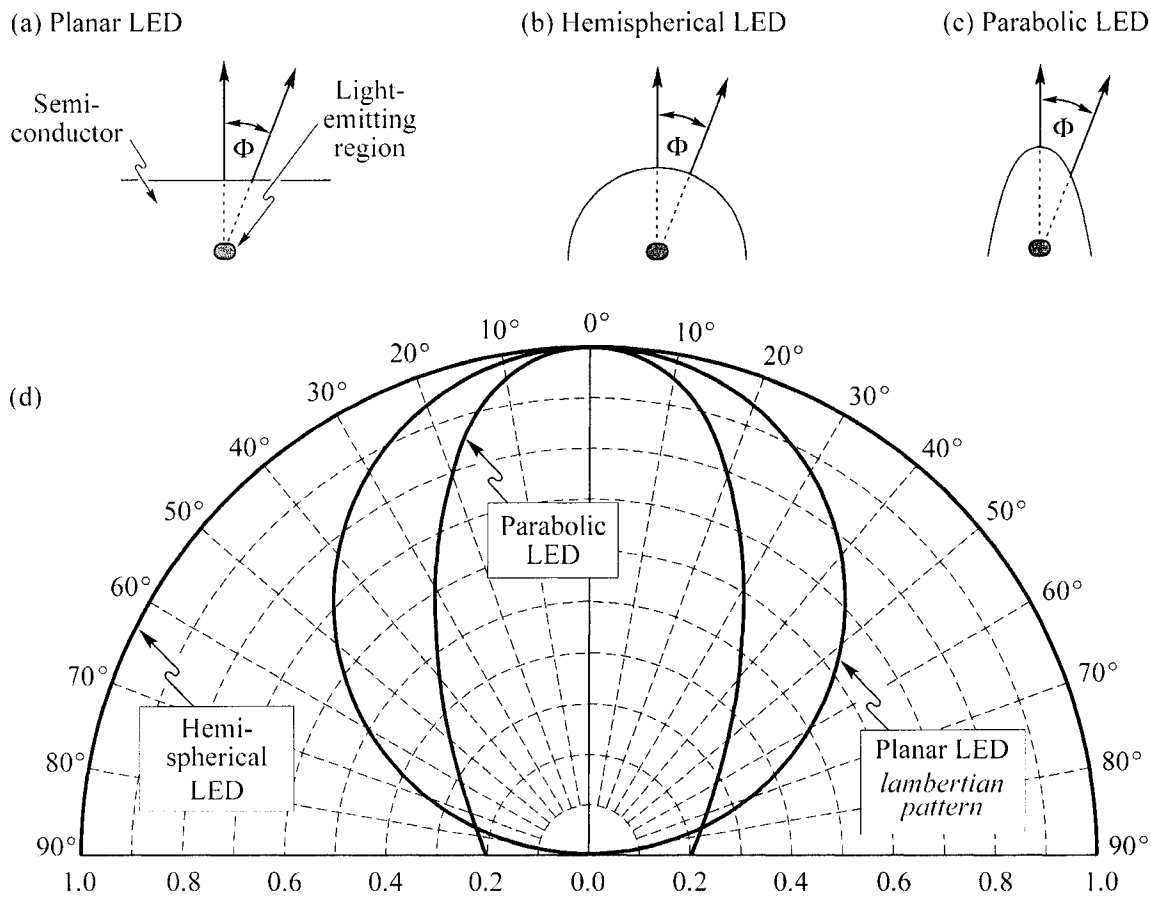

Figure 1.7 Illustration of three possible LED shapes (a-c), and (d) their effect on light emission pattern. In (d), the radial coordinate (bottom) represents the normalized emission intensity and the angular coordinate is the angle of observation, Φ. Image courtesy of E. Fred Schubert, Department of Electrical, Computer & Systems Engineering and Department of Physics, Rensselaer Polytechnic Institute, Troy, NY.

Even prior to the introduction of high-power LEDs, researchers had begun to use LEDs as an alternative to the traditional light sources for fluorescence: lasers and broadband light sources. The physical and electrical characteristics of LEDs are especially favourable. LEDs are much smaller than lasers or arc lamps, and have extremely long lifetimes (50,000 – 100,000 h) even under challenging conditions such as high humidity and mechanical vibration. LEDs can even be autoclaved. The power output of LEDs is also extremely stable at ~ 0.1% RSD. Diode lasers are equally stable, but are much more sensitive to temperature fluctuations. A HeCd laser, in contrast, shows about 1.4% RSD power output.[14] Thus, these properties of LEDs make them very amenable to miniaturized field instruments.[59, 60] Spectrally, the advantages of LEDs are not as obvious. The power emitted by standard LEDs is typically lower than that of lasers or arc lamps. However, their commercial availability in nearly every visible colour, and their broad line emission (FWHM of 10–30 nm) allows LEDs to excite a wide range of analytes.

High-power LEDs maintain almost all the advantages of standard LEDs as a potential light source in spectroscopic measurements. However, two disadvantages arise when using high-power LEDs. First, these LEDs have a greater divergence than low-power LEDs. This divergence makes it challenging to obtain a narrowly focussed beam, required for small-scale analyses. Another factor affecting the ability to focus the light from high-power LEDs is the size of the emitter. A larger emitter inherently produces a larger focussed spot. Nonetheless, LEDs with this much power should be capable of producing impressive sensitivity for CE measurements, and thus the use of LEDs is the focus of the majority of this thesis.

1.3.1.3 Figures of Merit for Fluorescence Detection

The three most relevant figures of merit for the detectors constructed in this thesis are dynamic range, sensitivity and detection limit. Dynamic range is the concentration range over which samples can be accurately quantified. The lower limit in the dynamic range is the limit of quantitiation, below which the analytical signal is lost in the instrument noise. At the upper limit of the dynamic range, the calibration curve departs from linearity. A large dynamic range is desirable, and a 100-fold concentration range necessary for a detector to be useful. Sensitivity is defined as the ability to distinguish a small difference in concentration, and is measured as the slope of a calibration curve. The detection limit (DL) of a compound is the lowest concentration at which it can be detected with some certainty. Perhaps the most frequently used calculation for DL is

$$DL = \bar{S}_{bl} + ks_{bl} \qquad \textbf{1.18}$$

where $\bar{S}_{bl}$ is the mean signal for a blank, s_{bl} is the standard deviation of several blanks, and k is a constant. Various values for k have been used, but $k = 3$ is most common.

1.4 Thesis Overview

Capillary electrophoresis is a small-scale separation technique, analyzing nanolitres of sample. A home-built CE system can be assembled for perhaps $10,000, with the majority of is the cost due to the high-voltage power supply. It is therefore inappropriate to use a bulky gas-phase laser consuming thousands of watts of power and costing at least $8000 as part of the detector. Diode lasers present a step in the right direction, being significantly cheaper and much smaller than gas-phase lasers. In Chapter

Two, a violet diode laser is used as the light source for CE-LIF detection. Myoglobin is a well-studied protein and a urinary marker of muscle destruction. By optimizing two novel non-covalent labelling schemes, myoglobin is fluorescently labelled with a porphyrin that mimics its natural heme cofactor.

Light-emitting diodes in turn, are extremely small and their cost is trivial. With recent improvements in LED technology, numerous groups have begun to use these small and inexpensive devices as light sources for fluorescence detection in CE.[61-69] Few of these reported LED-fluorescence instruments have made appropriate use of the LED light, and consequently, most report limits of detection in the μM range. Chapter Three investigates the use of LEDs for fluorescence detection on a capillary-sized scale. The use of a bandpass filter to restrict the bandwidth of light reaching the detector is critical. Specific guidelines used to select appropriate bandpass filters is given.

LEDs delivering 500 mW of light power became available in 2003. Making use of such unmatched power is the focus of Chapter Four. These new LEDs are significantly more divergent than previous LEDs and also have a larger emitting area. Both these aspects make it difficult to tightly focus the light, which leads to inefficient use of light or to detector bandbroadening. A detailed study of spatial filtering and detector bandbroadening is presented, in order to optimize the use of light delivered by these new devices. Finally, in Chapter Five, the high-power LED is used to detect DNA fragments from DNA sequencing reactions and from a DNA digest. Chapter Six will summarize the thesis and propose further areas for study.

1.5 References

(1) Tiselius, A. *Trans. Faraday Soc.* **1937**, *33*, 524-530.

(2) Wieland, T.; Fischer, E. *Naturwissenschaften* **1948**, *35*, 29-30.

(3) Consden, R.; Gordon, A. H.; Martin, A. J. P. *Biochem. J.* **1946**, *40*, 33-41.

(4) Grabar, P.; Williams, C. A. *Biochim. Biophys. Acta* **1953**, *10*, 193-194.

(5) Smithies, O. *Biochem. J.* **1955**, *61*, 629-641.

(6) Hjerten, S. *Biochim. Biophys. Acta* **1961**, *53*, 514-517.

(7) Raymond, S.; Weintraub, L. *Science* **1959**, *130*, 711-711.

(8) Mikkers, F. E. P.; Everaerts, F. M.; Verheggen, T. *J. Chromatogr.* **1979**, *169*, 11-20.

(9) Jorgenson, J. W.; Lukacs, K. D. *Anal. Chem.* **1981**, *53*, 1298-1302.

(10) Baryla, N. E.; Lucy, C. A. *Electrophoresis* **2001**, *22*, 52-58.

(11) Kenndler, E.; Schwer, C.; Kaniansky, D. *J. Chromatogr.* **1990**, *508*, 203-207.

(12) Hogan, B. L.; Lunte, S. M.; Stobaugh, J. F.; Lunte, C. E. *Anal. Chem.* **1994**, *66*, 596-602.

(13) Diress, A. G.; Lucy, C. A. *J. Chromatogr. A* **2004**, *1027*, 185-191.

(14) Melanson, J. E.; Boulet, C. A.; Lucy, C. A. *Anal. Chem.* **2001**, *73*, 1809-1813.

(15) Laitinen, H. A. *Anal. Chem.* **1973**, *45*, 2305-2305.

(16) Grossman, P. D. In *Capillary Electrophorsis: Theory and Practice*; Grossman, P. D., Colburn, J. C., Eds.; Academic Press, Inc.: New York, 1992, pp 1-44.

(17) Lee, C. S. In *Handbook of Capillary Electrophoresis,* 2nd ed.; Landers, J. P., Ed.; CRC Press: New York, 1997, pp 717-739.

(18) von Smoluchowski, M. *Bull. Int. Acad. Sci. Cracovie* **1903**, *8*, 182– 200.

(19) Schwer, C.; Kenndler, E. *Anal. Chem.* **1991**, *63*, 1801-1807.

(20) Lukacs, K. D.; Jorgenson, J. W. *Journal of High Resolution Chromatography & Chromatography Communications* **1985**, *8*, 407-411.

(21) Lucy, C. A.; Yeung, K. K. C.; Peng, X. J.; Chen, D. D. Y. *LC-GC* **1998**, *16*, 26-32.

(22) Cunliffe, J. M.; Baryla, N. E.; Lucy, C. A. *Anal. Chem.* **2002**, *74*, 776-783.

(23) MacDonald, A. M.; Lucy, C. A. *J. Chromatogr. A* **2006**, *1130*, 265-271.

(24) Melanson, J. E.; Baryla, N. E.; Lucy, C. A. *Anal. Chem.* **2000**, *72*, 4110-4114.

(25) Wang, C. Z.; Lucy, C. A. *Anal. Chem.* **2005**, *77*, 2015-2021.

(26) Yassine, M. M.; Lucy, C. A. *Anal. Chem.* **2005**, *77*, 620-625.

(27) Yeung, K. K. C.; Lucy, C. A. *Anal. Chem.* **1997**, *69*, 3435-3441.

(28) Hjerten, S. *Electrophoresis* **1990**, *11*, 665-690.

(29) Terabe, S.; Otsuka, K.; Ando, T. *Anal. Chem.* **1985**, *57*, 834-841.

(30) Thormann, W.; Mosher, R. A.; Bier, M. *J. Chromatogr.* **1986**, *351*, 17-29.

(31) Kopwillem, A. *J. Chromatogr.* **1973**, *82*, 407-409.

(32) Vacik, J.; Zuska, J. *Chem. Listy* **1972**, *66*, 416.

(33) Cohen, A. S.; Karger, B. L. *J. Chromatogr.* **1987**, *397*, 409-417.

(34) Cohen, A. S.; Najarian, D. R.; Paulus, A.; Guttman, A.; Smith, J. A., *et al. Proc. Natl. Acad. Sci. U. S. A.* **1988**, *85*, 9660-9663.

(35) Porath, J.; Flodin, P. *Nature* **1959**, *183*, 1657-1659.

(36) Pentoney, S. L.; Sweedler, J. V. In *Handbook of Capillary Electrophoresis,* 2nd ed.; Landers, J. P., Ed.; CRC Press: New York, 1997, pp 379 - 424.

(37) Swinney, K.; Bornhop, D. J. *Electrophoresis* **2000**, *21*, 1239-1250.

(38) Haber, C. In *Handbook of Capillary Electrophoresis,* 2nd ed.; Landers, J. P., Ed.; CRC Press: New York, 1997, pp 425 - 448.

(39) Olivares, J. A.; Nguyen, N. T.; Yonker, C. R.; Smith, R. D. *Anal. Chem.* **1987**, *59*, 1230-1232.

(40) Herschel, J. F. W. *Phil. Trans. R. Soc. London* **1845**, *135*, 143 - 145.

(41) Stokes, G. G. *Phil. Trans. R. Soc. London* **1852**, *142*, 463 - 465.

(42) Takamizawa, A.; Steinmetz, T.; Delhuille, R.; Hansch, T. W.; Reichel, J. *Optics Express* **2006**, *14*, 10976-10983.

(43) Wu, S. L.; Dovichi, N. J. *J. Chromatogr.* **1989**, *480*, 141-155.

(44) Skoog, D. A.; Holler, F. J.; Nieman, T. A. *Principles of Instrumental Analysis*, 5th ed.; Saunders College Publishing: New York, 1998.

(45) Johnson, M. E.; Landers, J. P. *Electrophoresis* **2004**, *25*, 3513-3527.

(46) Gassmann, E.; Kuo, J. E.; Zare, R. N. *Science* **1985**, *230*, 813-814.

(47) Chen, D. Y.; Dovichi, N. J. *Anal. Chem.* **1996**, *68*, 690-696.

(48) Yeung, E. S.; Wang, P. G.; Li, W. N.; Giese, R. W. *J. Chromatogr.* **1992**, *608*, 73-77.

(49) Lee, T. T.; Yeung, E. S. *J. Chromatogr.* **1992**, *595*, 319-325.

(50) Gooijer, G.; Mank, A. J. G. *Anal. Chim. Acta* **1999**, *400*, 281-295.

(51) Edmund Optics Catalog, N068A 2006

(52) Nathan, M. I.; Dumke, W. P.; Burns, G.; Dill, F. H.; Lasher, G. *Appl. Phys. Lett.* **1962**, *1*, 62-64.

(53) O'Hagan, W. J.; McKenna, M.; Sherrington, D. C.; Rolinski, O. J.; Birch, D. J. S. *Meas. Sci. Technol.* **2002**, *13*, 84-91.

(54) Rusak, D. A.; James, W. H.; Ferzola, M. J.; Stefanski, M. J. *J. Chem. Educ.* **2006**, *83*, 1857-1859.

(55) Fischer, A. L. *Photonics Spectra* **2006**, *40*, 90-92.

(56) Kasap, S. pn Junction Devices and Light Emitting Diodes; An E-Booklet 2001

(57) Chhajed, S.; Xi, Y.; Li, Y. L.; Gessmann, T.; Schubert, E. F. *J. Appl. Phys.* **2005**, *97*.

(58) Krames, M. R.; Ochiai-Holcomb, M.; Hofler, G. E.; Carter-Coman, C.; Chen, E. I., *et al. Appl. Phys. Lett.* **1999**, *75*, 2365-2367.

(59) Li, J. Z.; Dasgupta, P. K.; Genfa, Z.; Hutterli, M. A. *Field Analytical Chemistry and Technology* **2001**, *5*, 2-12.

(60) Toda, K.; Dasgupta, P. K.; Li, J. Z.; Tarver, G. A.; Zarus, G. M., *et al. Anal. Chem.* **2001**, *73*, 5716-5724.

(61) Bruno, A. E.; Maystre, F.; Krattiger, B.; Nussbaum, P.; Gassmann, E. *Trends Anal. Chem.* **1994**, *13*, 190-198.

(62) Chabinyc, M. L.; Chiu, D. T.; McDonald, J. C.; Stroock, A. D.; Christian, J. F., *et al. Anal. Chem.* **2001**, *73*, 4491-4498.

(63) Dang, F.; Zhang, L.; Hagiwara, H.; Mishina, Y.; Baba, Y. *Electrophoresis* **2003**, *24*, 714-721.

(64) Hart, S. J.; Jiji, R. D. *Anal. Bioanal. Chem.* **2002**, *374*, 385-389.

(65) Hillebrand, S.; Schoffen, J. R.; Mandaji, M.; Termignoni, C.; Grieneisen, H. P. H., *et al. Electrophoresis* **2002**, *23*, 2445-2448.

(66) Kuo, J. S.; Kuyper, C. L.; P.B., A.; Fiorini, G. S.; Chiu, D. T. *Electrophoresis* **2004**, *25*, 3796 - 3804.

(67) Uchiyama, K.; Xu, W.; Qiu, J. M.; Hobo, T. *Fresenius' J. Anal. Chem.* **2001**, *371*, 209-211.

(68) Wang, S. C.; Morris, M. D. *Anal. Chem.* **2000**, *72*, 1448-1452.

(69) Webster, J. R.; Burns, M. A.; Burke, D. T.; Mastrangelo, C. H. *Anal. Chem.* **2001**, *73*, 1622-1626.

CHAPTER TWO. Non-Covalent Labelling of Myoglobin by Reconstitution with a Fluorescent Porphyrin[a]

2.1 Introduction

The use of fluorescence detection in capillary electrophoresis allows for vastly improved detection limits, compared to the very popular absorbance detectors. As discussed in Section 1.3.1.1, lasers are an ideal excitation source due to their high power, collimated beam and monochromatic light. In the field of proteomics, CE-LIF is becoming increasingly prominent.[1, 2] A number of approaches have been used to perform LIF of proteins. The native fluorescence of aromatic amino acids Trp, Tyr and Phe has been exploited,[3, 4] but complex and expensive gas-phase lasers operating in the deep UV (<300 nm) are required. Alternatively, solid state lasers such as the frequency-quadrupled Nd:YAG can be used, but at a wavelength of 266 nm, it is not well matched with the native excitation of Trp (280 nm) and thus shows reduced sensitivity. Even under optimal conditions, Tyr and Phe are poor fluorophores due to their low extinction coefficient and low quantum yield, respectively, while Trp is a relatively rare amino acid. These disadvantages restrict detection limits to the low-nM range, using native fluorescence of proteins.[3]

---

[a] This work was performed in part by Dr. Jeremey Melanson, and has been published as E.P. deJong, J.E. Melanson and C.A. Lucy, "Noncovalent labeling of myoglobin for capillary electrophoresis with laser-induced fluorescence detection by reconstitution with a fluorescent porphyrin", *Electrophoresis* **2004**, *25*, 3153-3162.

A few proteins possess native fluorescence in the visible spectrum. For instance, green fluorescent protein (GFP; *Aequorea victoria*; jellyfish) contains a fluorophore formed by the cyclization of the Ser^{65}-Tyr^{66}-Gly^{67} tripeptide. GFP has been extensively used in molecular and cell biology.[5, 6] In conjunction with CE, an endogenous GFP-tagged substrate has been used to assay intracellular enzymatic activity[7] and a GFP-fusion protein has been used to study protein-protein interactions.[8] GFP has also been used as a model protein in fundamental studies in capillary electrophoresis.[9, 10] Other fluorescent proteins are being developed to extend the utility of genetically encoded reporters.[11]

When the use of a protein's native fluorescence is not convenient, one can use covalent or non-covalent derivatizations with a fluorophore to produce a detectable product. Covalent derivatization of proteins with fluorescent labels such as sulforhodamine 101[12] and rhodamine 6G[13] have achieved detection limits down to the single molecule level. However, fluorescent labelling of proteins is not without its problems. These derivatization reactions often yield innumerable reaction products whose mobility all differ slightly. In some cases this multitude of products results in a single, broad peak,[10] while in other cases a "charge ladder" may be observed. Such charge ladders have been used to determine the charge of a protein, N-terminal pKa's and in estimating protein molecular mass under non-denaturing conditions.[14] The resulting peaks, however, do not result from a single reaction product but rather from a number of regioisomers with a similar charge-to-size ratio, and are best viewed as a series of broadened peaks resulting from a single protein.

Further complicating attempts to fluorescently label proteins is that micromolar concentrations of both protein and dye[15] are generally required for the reaction to proceed, although exceptions have been reported.[2] Since a typical mammalian cell contains in the neighbourhood of 50 pg or 2 fmol of total protein, one would require 500 cells to prepare 1 μL of a 1 μM total protein solution. Of course not all proteins in the cell are of interest. When performing an assay of low-abundance proteins, the number of cells required would be substantially higher.

Non-covalent, fluorescent labelling of proteins was first used for capillary electrophoresis by Swaile and Sepaniak,[4] although the technique has been used in protein folding studies for half a century. It has also been used in capillary isoelectric focussing, most commonly studying albumin. Non-covalent labels used thus far include indocyanine green,[16] squarylium dyes,[17] arylsulfonates,[4, 18] NanoOrange[19, 20] and the Sypro series of dyes.[21, 22] These synthetic dyes are all foreign to the proteins, whereas this chapter describes the use of a class of naturally-occurring labels which are native to the proteins being labelled.

This chapter explores the potential of using a large class of natural proteins that contains an intrinsic fluorophore that could be exploited for LIF detection in CE and other applications. These proteins are the heme proteins, so called because their structure includes an iron-containing porphyrin molecule known as the heme group. Porphyrins possess an intense excitation band at ~400 nm, known as the Soret band.[23] Using excitation with a violet diode laser (400 nm) picomolar detection limits have been achieved for urinary porphyrins using CE-LIF.[24] Thus, the violet diode laser presents an opportunity for highly sensitive detection of heme proteins. The primary challenge for

this approach is that the porphyrin of the heme group contains a central Fe atom, which is an efficient quencher of fluorescence. Myoglobin will be used as the model heme protein for these studies, as it is a biologically important as an oxygen carrier and yet is simple in structure. The non-covalent labels used are fluorescent porphyrins; analogues of the heme group.

2.2 Experimental

2.2.1 Chemicals

Myoglobin (from horse skeletal muscle; 95-100%; crystallized and lyophilized; essentially salt-free; Sigma), apo-myoglobin (from horse skeletal muscle; salt-free, lyophilized powder; Sigma), bovine serum albumin (≥ 99%; Sigma), protoporphyrin IX (PPIX, Aldrich), Protoporphyrin IX, zinc (II) complex (Zn-PPIX; Aldrich), urea (99.5%; BDH), boric acid (ACS grade; BDH), hydrochloric acid (EM Science) and sodium hydroxide (10 N solution; Fisher) were used as received. Ultrapure water was obtained from a Nanopure water system (Barnstead; Dubuque, IO, U.S.A.). Borate buffer was prepared by dissolving an appropriate amount of boric acid in ultrapure water and adjusting the pH by the addition of 1 M NaOH while stirring. Stock solutions of 10 μM PPIX and Zn-PPIX solutions were prepared in 50/50 (v/v%) methanol / 25 mM borate buffer, pH 9.5 and were stored in glass containers covered by foil to prevent photodegradation. Sonication aided dissolution of the porphyrins. Solutions of PPIX showed < 1% loss in fluorescent intensity after 12 months' storage at room temperature. A solution of Zn-PPIX did, however, exhibit ~ 14 % degradation within 12 months upon

storage under the same conditions as PPIX. It is recommended that new solutions be prepared every 3 months.

2.2.2 Apparatus

The home-built instrument used was described previously.[24] Briefly, voltage and pressure at the inlet vial were controlled by a Crystal CE system (model 300, ATI Unicam, Boston, MA, U.S.A.). Detection was performed on-capillary using a home-built LIF detection system as depicted in Figure 2.1. The laser was a 400 nm violet diode laser (Nichia; Tokyo, Japan) with a maximum output power of 5 mW. The diode was housed in an aluminium heat sink and the emitted light was collimated by a laser diode collimator (Oz Optics; Carp, ON, Canada). The collimated light was focussed onto the capillary by passing the light through a 400 μm pinhole (Melles Griot; Carlsbad, CA, U.S.A.) and subsequently through a 6.3 × (0.20 N.A.) microscope objective (Melles Griot). Fluorescent light was collected at a right angle through a 40 × (0.65 N.A.) microscope objective, spatially filtered by a 1 mm pinhole (Melles Griot), optically filtered by either a 600 nm bandpass filter (600DF50; Omega Optical; Battleboro, VT, U.S.A.) or a 450 nm cut-off filter (450 CFLP, Omega Optical) and detected by a photomultiplier tube (Hamamatsu R3896; Hamamatsu; Bridgewater, NJ, U.S.A.). The photomultiplier tube was operated at 600 V. The signal from the photomultiplier tube was gathered via a connection to a data acquisition board (National Instruments; Austin, TX, U.S.A.), displayed by Virtual Bench Logger software (version 2.51; National Instruments) at 5 Hz and stored on a Celeron 400 MHz PC. Data was plotted and analyzed using Igor Pro version 3.12 (WaveMetrics, Inc.; Lake Oswego, OR, U.S.A.).

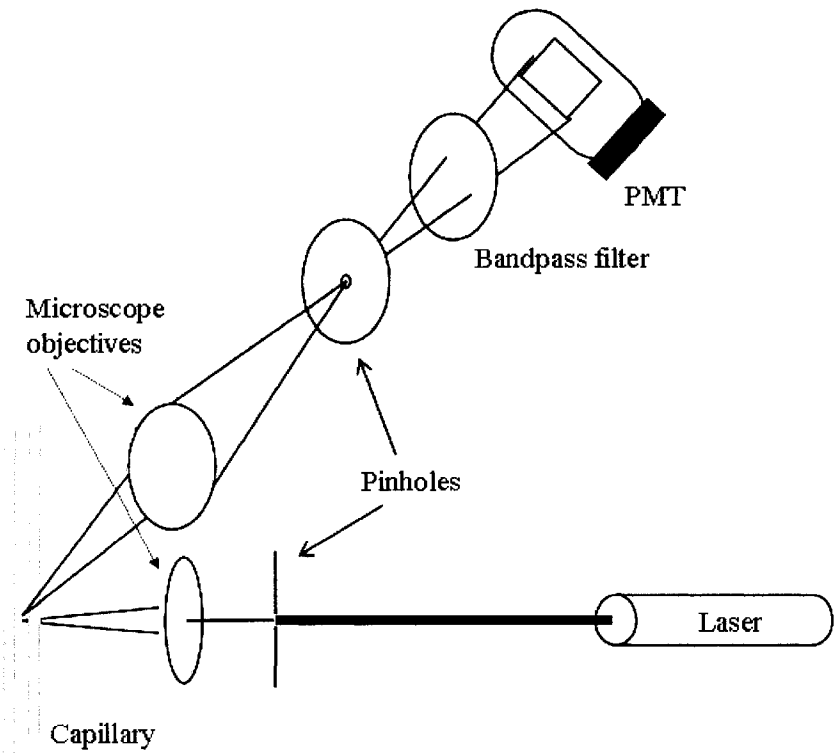

Figure 2.1 Schematic of the LIF detector. The laser beam diameter is reduced by a pinhole, and a microscope objective focusses the light on the capillary inner diameter. Fluorescence is collected at right angles by another microscope objective, spatially filtered by another pinhole, and spectrally filtered by a bandpass filter. A photomultiplier tube (PMT) detects the fluorescence signal.

Experiments were performed with 70 cm × 50 μm I.D. (360 μm O.D.) fused silica capillary (Polymicro Technologies, Phoenix, AZ, USA) with an effective length of 65 cm. The capillary was at room temperature (~23°C).

2.2.3 Procedures

2.2.3.1 Reconstitution From *Apo*-Myoglobin

Holo-myoglobin has been reconstituted from *apo*-myoglobin by adding 5 μL of 14 μM protein and 10 μL of 10 μM PPIX to 985 μL of 25 mM borate buffer pH 9.5 and then vortexing. The reconstitution was allowed to proceed for at least 30 min before injecting the solution. These reactions were injected at 50 mbar for 6 s, separated at 20 kV and used a 600DF50 optical filter for fluorescence detection.

2.2.3.2 Reconstitution From Myoglobin

A variety of CE-LIF studies were performed to optimize the reaction of urea-denatured myoglobin. To study the effect of denaturation time on the reaction yield, the native protein was denatured by combining 10 μL of 50 μM myoglobin and 90 μL of 6.0 M urea in a 1.5 mL microcentrifuge vial (Rose Scientific). The solution was allowed to sit for 1 to 15 min prior to renaturation. The protein was renatured by adding 100 μL of 10 μM PPIX solution and diluting the solution to 1 mL with ultrapure water, thereby reducing the urea concentration. For studies of the initial urea denaturant concentration, varying amounts of water were added to 10 μL of 50 μM myoglobin prior to the addition of urea. The denaturation was allowed to proceed for 1 min, followed by the addition of

PPIX solution and renaturation by diluting with water to 0.54 M urea. The effect of reducing the final urea concentration was also investigated. These reactions used 80, 70 and 60 μL of 6.0 M urea, were given 1 min to denature prior to the addition of PPIX and then diluted to 1 mL as above. Finally, the volume of PPIX added to the solution was studied. Here, 90 μL of 6.0 M urea was added to the protein. After 1 min, 100, 200, 300, 500 or 700 μL of PPIX solution was added and then the solution was diluted to 1 mL with water.

Alternately, the denaturation can be based on pH changes. In this case, 10 μL of 0.02 M HCl was added to 10 μL of 50 μM myoglobin. To study the effect of denaturation time on the reaction yield, the solution was allowed to stand between 1 s and 3 min, followed by addition of 100 μL of 10 μM PPIX solution and 10 μL of 0.02 M NaOH. The total volume was then made up to 1 mL using ultrapure water. The volume of PPIX solution added to the reaction was also investigated. These reactions used between 100 and 700 μL of PPIX, followed by NaOH and water, as above. Once the reaction conditions were optimized, Zn-PPIX could be used in place of PPIX.

In the studies where equimolar amounts of bovine serum albumin (BSA) were added as a possible interferent, reactions were performed as described above for both urea and low-pH denaturation studies, except that 10 μL of 50 μM BSA was added to the reaction container prior to all other solutions. For studies using greater excesses of BSA, reactions were performed as described above for low-pH denaturation studies, except that diluted myoglobin (10 μL at 5 μM) was used with an appropriate volume of 50 or 500 μM BSA. The concentration of BSA solution used was chosen so that the volume used

was minimized, but not less than 3 μL. When the total volume of protein solutions exceeded 20 μL, the volumes of HCl and NaOH added equalled that of the BSA solution.

The limit of detection at the 99% confidence limit for myoglobin was investigated following a published method [25]. The reactions were performed by combining 267 μL of 0.25 μM myoglobin (water used for blanks) and 267 μL of 0.02 M HCl, waiting for 2 min, adding 200 μL of 10 μM Zn-PPIX and 267 μL of 0.02 M NaOH. Ten blank and reaction solutions were analyzed.

2.2.3.3 Non-Denaturing Heme Exchange

For simple myoglobin labelling, 10 μL of 50 μM myoglobin was delivered to a microfuge tube, followed by 790 μL of ultrapure water and then 200 μL of 10 μM PPIX or Zn-PPIX solution. The reaction solutions were mixed by inverting the tube several times. Electrophoresis of the samples was started approximately 3 min after the solution was mixed. In BSA interference studies, 10 μL of 5 μM myoglobin was combined with an appropriate volume (between 3 and 30 μL) of 50 or 500 μM BSA solution. Ultrapure water was added to a volume of 800 μL, followed by 200 μL of Zn-PPIX solution. These reactions were mixed as above.

2.2.3.4 Capillary Electrophoresis with LIF Detection

New capillaries were rinsed with 0.1 M NaOH at 2000 mbar, followed by water for at least 10 min each. Between runs, capillaries were rinsed with run buffer for 5 min at 2000 mbar (~ six capillary volumes). Samples were injected at 50 or 100 mbar for 6 s.

The separation buffer used was 25 mM boric acid, pH 9.5. Applied voltages were 20 or 25 kV. The violet diode laser intensity at the capillary was 250 to 300 μW. The laser power was determined with a LaserCheck hand-held laser power meter (Melles Griot).

2.3 Results and Discussion

Heme proteins are critical components of several biological processes, including drug detoxification and aerobic respiration. A heme protein which serves as a useful model, myoglobin, is studied in this chapter. Myoglobin is an oxygen-binding protein of muscle cells. It is a relatively small (MW = 16,700; horse skeletal) protein and consists of single polypeptide chain of 153 amino acid residues of known sequence. Myoglobin folds such that most of the hydrophobic amino acid side chains are oriented toward the interior of the molecule. This creates a very dense hydrophobic core or pocket that is typical of globular proteins. Inside this hydrophobic pocket sits the porphyrin ring known as the heme group. Figure 2.2 shows the structure of myoglobin.[26]

The heme group of myoglobin consists of a protoporphyrin IX (PPIX) molecule in which an Fe (III) atom is bound by the four pyrrole-nitrogens of the porphyrin. The heme group is held in the inner pocket of myoglobin by two main forces. Firstly, the iron atom of the heme group forms a coordinate bond to His^{93}. Secondly, the heme group (or PPIX) is held in place by the hydrophobic interaction between the porphyrin and the hydrophobic residues of the inner pocket of myoglobin.

Protoporphyrin IX, shown in Figure 2.3, in its free-base form is highly fluorescent with excitation and emission maxima at 400 nm (Soret band) and 619 nm, respectively (10 mM phosphate; pH 7.4).[27] The heme form exhibits normal absorption behavior, but

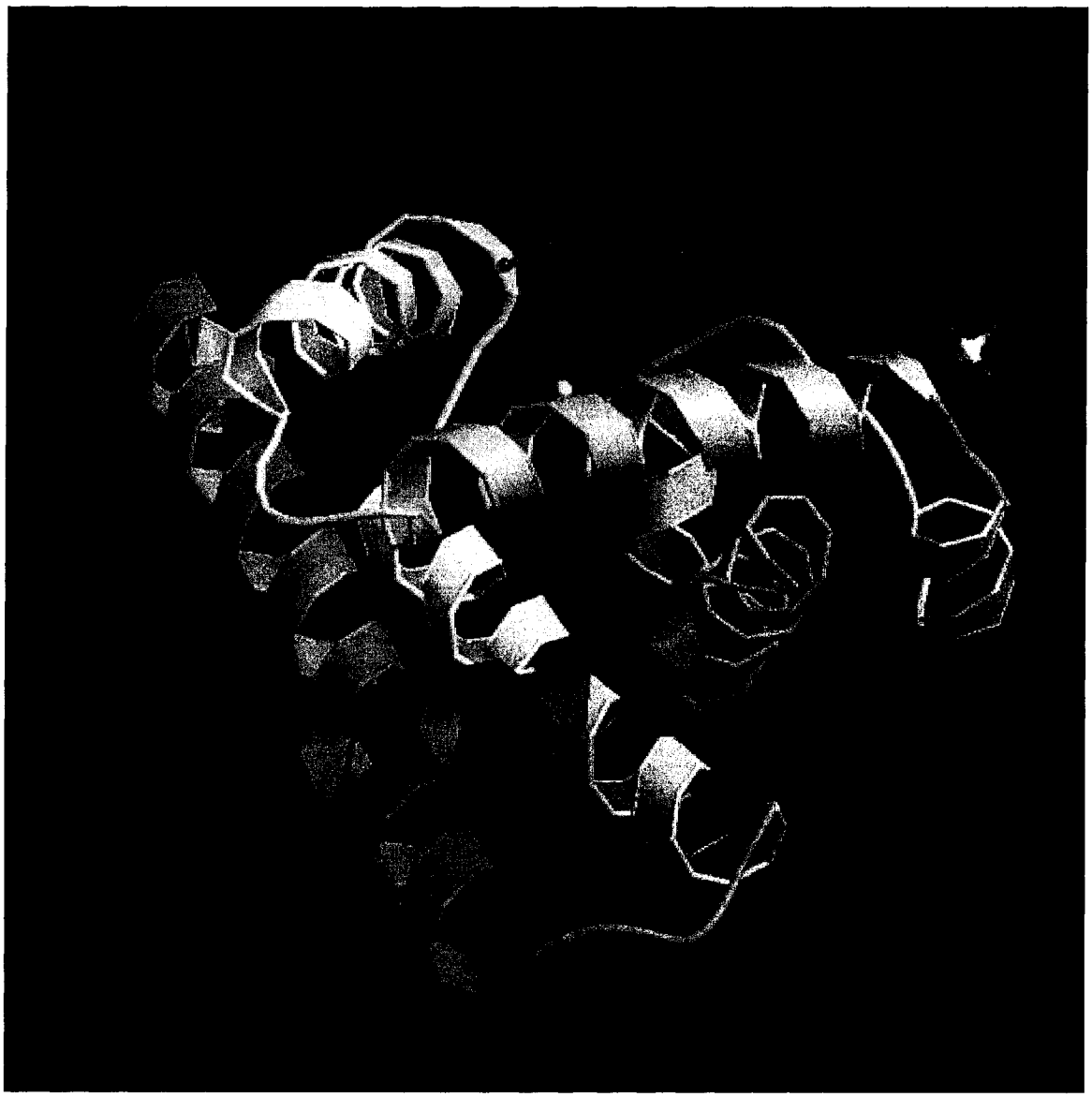

Figure 2.2 Three-dimensional structure of horse heart myoglobin. The polypeptide backbone shown in a ribbon representation and the heme group in ball-and-stick format.[26]

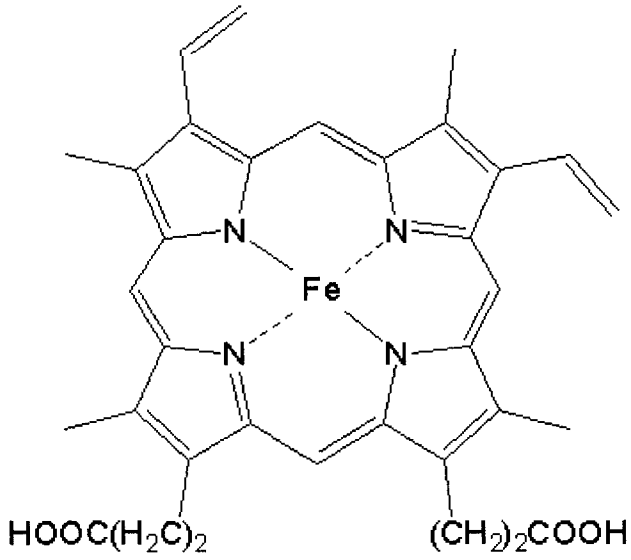

Figure 2.3 Structure of the heme group. The heme group consists of an iron atom bound to protoporphyrin IX (PPIX).

is essentially non-fluorescent. Fe(III) is a paramagnetic metal and as such, is an effective quencher of fluorescence. Although this quenching is usually considered 100 % efficient, very weak fluorescence ($\Phi_f \sim 4 \times 10^{-6}$) has been reported for some Fe-porphyrin complexes.[28] For comparison, other metalloporphyrins normally exhibit Φ_f between 0.001 and 0.2.[23] Figure 2.4 shows an electropherogram of 5 μM of native (Fe-containing) horse skeletal myoglobin in sodium borate buffer at pH 9.5. The multiple peaks observed between 5 and 6 minutes are most likely due to isoforms of myoglobin.

Horse myoglobin is known to have a major isoform (pI 7.4) and a minor isoform (pI 6.9) which have been separated by gel electrophoresis.[29] These peaks were also observed using UV absorbance detection (λ = 214 nm) under the same experimental conditions. The intensity of the peaks in Figure 2.4 are over 1500 times lower than achieved for an equimolar concentration of free-base PPIX (no Fe) using similar buffer conditions to those employed in previous porphyrin studies.[24] This reduction in signal can be qualitatively explained by the reduced quantum yield of porphyrins that contain iron ($\sim 4 \times 10^{-6}$).[28] With a limit of detection of 0.2 μM, native myoglobin fluorescence with excitation at 400 nm offers little advantage over absorbance detection in either the UV or 400-nm region.

2.3.1 Demetalation or Transmetalation of the Heme

Enhancing the fluorescence of myoglobin is essential to making LIF a viable alternative to direct absorbance detection. A seemingly simple solution would be to remove the Fe atom from the porphyrin. However, porphyrins bind metals extremely

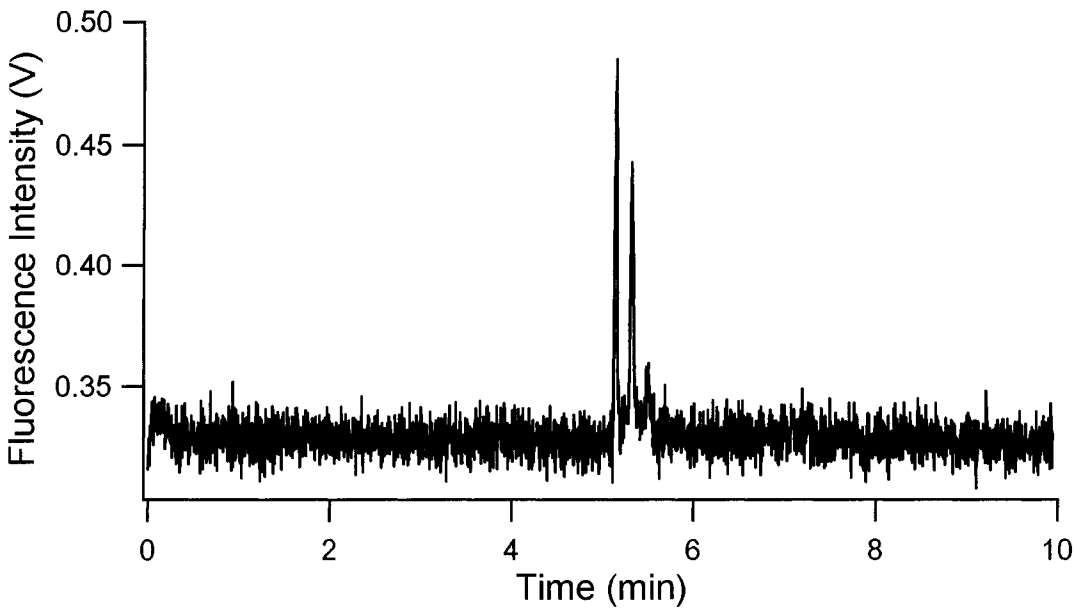

Figure 2.4 Electropherogram of 5 μM native horse skeletal myoglobin. Sample was injected at 50 mbar for 6 s; applied voltage was 20 kV; optical filter used was a 600 nm bandpass; background electrolyte was 25 mM sodium borate at pH 9.5.

strongly, with stability constants in the 10^{29} range.[30] Thus, extremely harsh conditions must be used to *demetalate* porphyrins. For instance, the standard method for demetalation of Fe-porphyrins calls for treatment with 100 % H_2SO_4 for 24 h.[30] These harsh conditions are obviously not compatible with proteins such as myoglobin in which the heme group is held noncovalently. Undoubtedly irreversible protein denaturation or even digestion would result.

A second possibility for enhancing the fluorescence of myoglobin would be to exchange the iron for a different metal ion. This procedure is known as transmetalation. Whereas metals such as Fe quench fluorescence, porphyrins containing closed shell metals exhibit relatively strong fluorescence. The quantum yields of closed shell metal-porphyrins such as Mg(II) and Zn(II) yield fluorescence quantum yields of 0.25 and 0.04, respectively.[23] However, a direct transmetalation of porphyrins has not been reported. Further, transmetalation procedures are tedious and dangerous. For instance, transmetallation of cytochrome c requires the use of anhydrous HF which is obtained through the condensation of $HF_{(g)}$ into containers cooled to liquid nitrogen temperatures.[31, 32] Thus, demetalation and transmetalation are not very appealing procedures for routine analysis.

2.3.2 Reconstitution of *Apo*-Myoglobin

A third option to render heme proteins fluorescent is to replace the entire heme group with a fluorescent porphyrin. The simplest scenario, explored herein, involves the use of a heme protein where the heme group is noncovalently bound. Myoglobin is chosen as a test compound in these studies, as its heme group can be removed upon

denaturation and re-introduced when the resulting *apo*-myoglobin is allowed to re-fold. The uptake of a porphyrin into *apo*-myoglobin is called reconstitution. This approach is explored below.

Initial studies focused on reconstituting *apo*-myoglobin and PPIX solutions to generate a fluorescent myoglobin as described in Section 2.2.3.1. The resulting concentrations of protein and PPIX are roughly ten-fold lower than the concentrations used by Adams, who first studied the kinetics of this reaction,[33] but the molar ratio is similar. As this reaction is second-order, this reduction in concentration is expected to decrease the reaction rate 100-fold. Even with this decrease in reaction rate, the reaction is essentially complete in 10 min. A background electrolyte of 25 mM borate pH 9.5 was chosen to maintain a net negative charge on both myoglobin and PPIX, and thus minimize adsorption onto the capillary wall. Figure 2.5 shows the reconstitution of myoglobin with PPIX. The upper trace in Figure 2.5 is the electropherogram for the injection of 100 nM PPIX solution. The lower trace corresponds to a reconstituted myoglobin solution. An excess of PPIX was used during reconstitution to verify that the apo-myoglobin is quantitatively converted to PPIX-myoglobin. As can be seen, the PPIX peak area is reduced by 72% upon reaction with *apo*-myoglobin, roughly consistent with the 30% excess of PPIX in the reaction.

Thus, the reconstitution occurs in a 1:1 ratio and is quantitative under the current conditions. The fluorescently labelled protein appeared as a pair of peaks at approximately 5.3 and 5.5 min. Myoglobin is known to separate into three components (Kagen[34] and in Figure 2.4), however it is conceivable that *apo*-myoglobin has lost of one of these components during purification and isolation. These experiments demonstrated

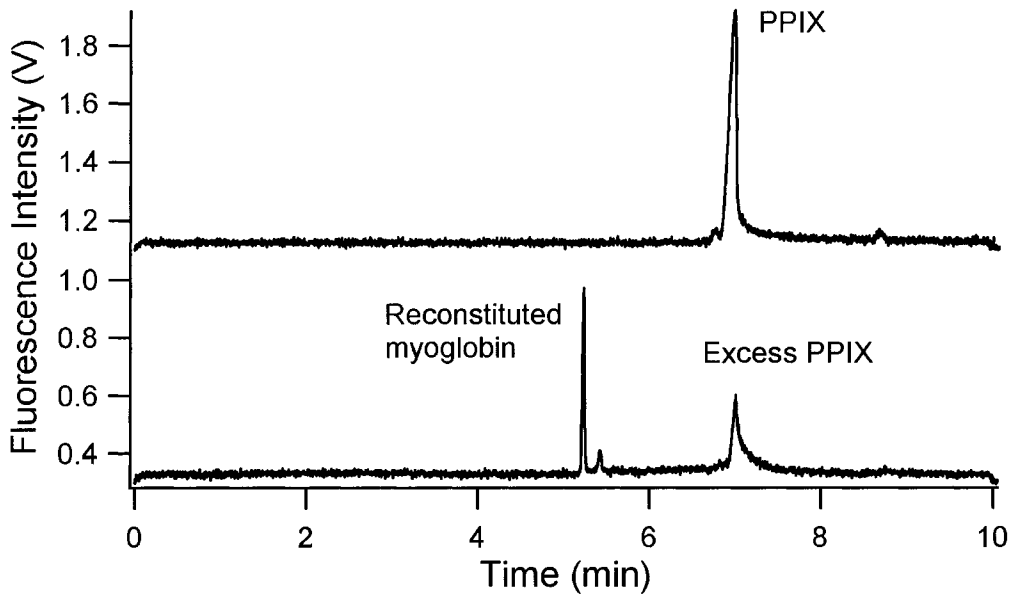

Figure 2.5 Electropherograms of PPIX (top trace) and the reaction of apo-myoglobin with PPIX (bottom trace). Reaction conditions are described in Section 2.2.3.1. Sample was injected at 50 mbar for 6 s; applied voltage was 20 kV; optical filter used was a 600 nm bandpass.

that the reconstitution is possible and that the chosen electrophoretic conditions allow the *holo*-protein to remain intact and give a fluorescent signal.

2.3.3 *Holo*-Myoglobin Reconstitution with Denaturing Conditions

The first step in labelling native (*holo*-) myoglobin is to denature the protein so that its hydrophobic pocket is disrupted and the heme group is released. However, this denaturation must be mild, so that the protein can later reconstitute with the porphyrin (i.e., irreversible denaturation must be avoided). Various procedures to denature a protein have been reported, including: (i) temperature;[35] (ii) pH;[36] (iii) organic solvents;[37] and (iv) chemical denaturants such as surfactants,[38] urea[39] and guanidine hydrochloride.[36] The denaturation step must also be reversible to be compatible with the subsequent reconstitution procedure. Organic solvents and surfactants are difficult to remove from solution, and thus are not compatible with reconstitution. Thermal denaturation must be done slowly and carefully to avoid irreversible denaturation.[35] Guanidine hydrochloride induced denaturation can be reversed by simply reducing the concentration of denaturant by dilution. However, the high concentration of the guanidine hydrochloride necessary for denaturation (typically $\geq$ 6 M) results in a high ionic strength sample plug that is not compatible with CE separation.[40] Urea must be used in similarly high concentrations (8 M) to act as a denaturant. However, urea is non-ionic and so does not generate electrodispersion in CE. Thus urea-based reconstitution was studied, and is discussed in Section 2.3.3.1. The use of low-pH for denaturation is also easily reversed (by increasing the pH), and will be discussed in Section 2.3.3.2.

2.3.3.1 Urea-Based Reconstitution

Urea-induced denaturation curves for myoglobin have been well studied, although there remains some ambiguity as to at what stage of the titration the protein can be considered denatured. A fairly conservative estimate considers myoglobin to be at least 90% unfolded at a urea concentration of 4.0 M, and less than 10% unfolded at concentrations below 1.3 M.[39] It has been established that myoglobin folding is complete within 10 seconds.[41] The effect of protein denaturation time was studied at times of 1, 5, 10 and 15 min, with each reaction being performed in triplicate and analyzed twice. While there were statistically significant differences in the resulting protein peak area at the 95% confidence level, the data showed only a slight positive correlation between denaturation time and protein signal (Appendix 1). The gradual increase in peak area with denaturation time is likely a reflection of the slow unfolding of myoglobin, similar to what is observed in equine alcohol dehydrogenase.[42] Thus, a gradual increase of labelling efficiency with denaturation time can be expected. A denaturation time of 1 min was chosen for speed and simplicity. Next, the effect of initial urea concentration was optimized. Urea was added at 5.4, 5.0, 4.5, 4.0, 3.5 and 3.0 M, with a maximum protein peak area observed at 4.5 M (Appendix 2). The relatively small observed increase in signal however, did not warrant the additional dilution step that this added to the reconstitution procedure and thus future studies used an initial urea concentration of 5.4 M. Another series of experiments used a lower total amount of urea to prevent irreversible unfolding of myoglobin and to promote complete folding upon dilution of the urea. Irreversible unfolding has been reported to occur when *Coprinus cinereus* peroxidase, another heme protein, is exposed to 4 M urea for over 300 s.[43] In these

studies, the initial urea concentrations were 5.33, 5.25 and 5.14 M, and final concentrations of 0.48, 0.42 and 0.36 M, respectively. No significant changes in protein peak area were observed (Appendix 3), and thus a volume of 90 μL urea solution (5.4 M urea initially) was maintained.

Finally, the volume of PPIX added to solution was optimized. It is expected that a greater concentration of PPIX in solution will increase the labelling efficiency of myoglobin, as there will be a greater ratio of PPIX : heme in solution. Molar excesses of 2, 3, 4, 6, 10, 14 and 18 of PPIX were added to the denatured protein (Appendix 4 and 5). This data was generated over two days, where the alignment of the optics and the sensitivity of the detector differed significantly. Nonetheless, the greatest protein peak area was observed with a 6-fold excess of PPIX. The progressive decrease in protein peak area beyond this level of PPIX can be explained by the solution conditions. The PPIX solvent is a 50:50 (v/v %) mixture of methanol and 25 mM borate buffer, pH 9.5. The use of methanol is necessitated by the poor solubility of PPIX in aqueous solutions. As the volume of added PPIX reaches 500 μL (10-fold PPIX excess), the final solution will contain 25% (v/v) methanol and thus myoglobin will be partially denatured.[44] In its denatured state, myoglobin can not be labelled by this procedure and thus gives a reduced fluorescent signal. Thus, it was determined that the simplest and most efficient reaction procedure used 5.4 and 0.54 M urea for protein denaturing and re-folding, respectively. The protein is denatured for 1 min, followed by the addition of 300 μL (6-fold excess) of PPIX solution and dilution to 1 mL. Figure 2.6 illustrates the urea-based reconstitution of myoglobin with all conditions optimized. Note that the peak shape of PPIX here and in all subsequent electropherograms differs from that in Figure

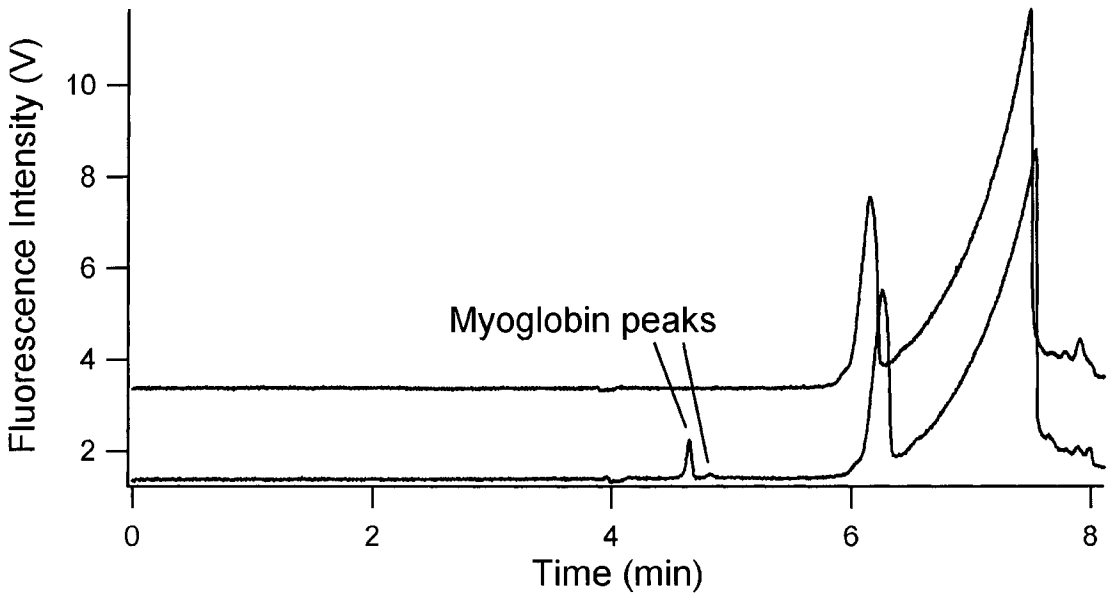

Figure 2.6 Myoglobin reconstituted following urea denaturation. Top trace is a blank where no myoglobin was added, while the bottom trace is the electropherogram of a reaction solution. Final [myoglobin] = 0.5 μM. Reaction conditions are described in Section 2.2.3.2.

2.5. This is caused by the large difference in concentration of PPIX (≥ 2 μM vs. 0.1 μM) in the later figures. Above pH 8 and 5 μM concentration, PPIX is known to dimerize, which is the likely cause of the peak shape.[45]

2.3.3.2 Low-pH Reconstitution

Myoglobin is fully denatured at pH 2.0[46, 47] and thus this labelling procedure should also be possible using low-pH denaturation for the release of heme. As in the case of urea denaturation, the time allowed for protein unfolding was examined. The times selected in this study are considerably shorter than those used in the urea study because it has been found that prolonged exposure of heme to acid solution decreases the rate of protein-heme recombination.[48] Reaction times of 1 s to 3.0 min were examined, but no significant trend in protein peak area was found (Appendix 6). A reaction time of 2.0 min was used for the remainder of the pH reconstitution studies. The volume of PPIX added to the reaction was also studied in the range of 100 to 700 μL of PPIX solution and the optimum volume was found to be 200 μL, or a mole ratio of 4 PPIX per myoglobin (Appendix 7). Figure 2.7 shows the results for an optimized pH-based reconstitution. The peak area for the labelled myoglobin in this figure is approximately 3.7 times that in Figure 2.6, demonstrating that the use of low-pH is a more efficient labelling procedure for myoglobin. The low-pH denaturation is more efficient at cleaving the heme from myoglobin. Below pH 4, the heme Fe is no longer co-ordinated to the histidine ligand.[49] While both denaturation schemes can disrupt the hydrophobic heme pocket, it is not expected that urea can also disrupt the iron-histidine interaction. As well, the use of pH

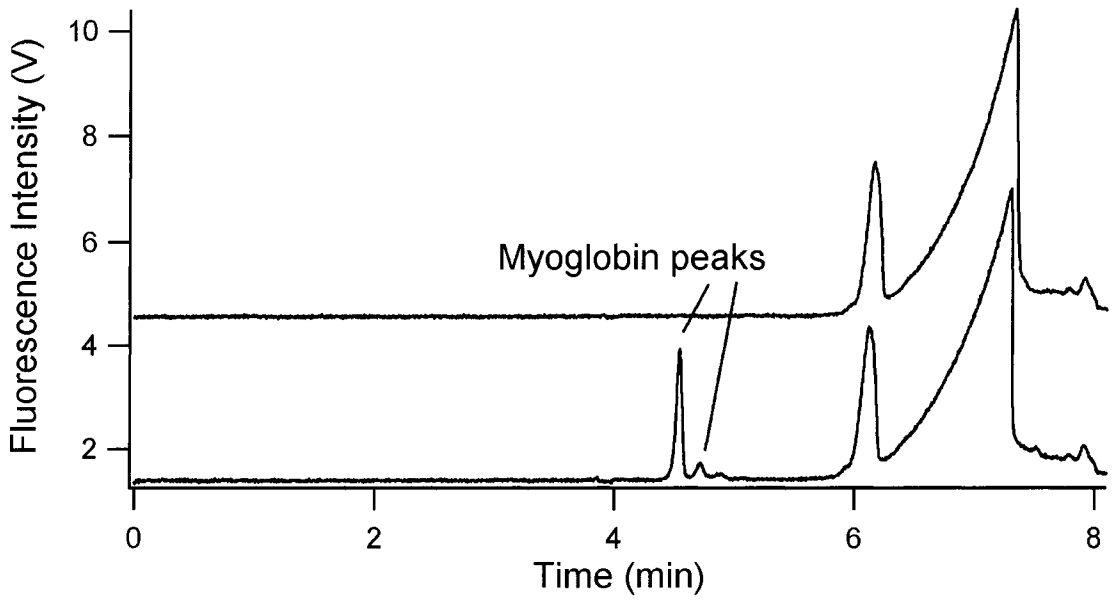

Figure 2.7 Myoglobin reconstituted following pH denaturation. Top trace is a blank where no myoglobin was added, while the bottom trace is the electropherogram of a reaction solution. Final [myoglobin] = 0.5 μM. Reaction conditions are described in Section 2.2.3.2.

changes does not require the final sample dilution that was used here. However, this dilution was employed to match the final myoglobin concentration with that of the urea-denatured reactions.

After optimizing this reaction procedure, Zn-PPIX was used in place of PPIX and gave 27 % higher protein signal. This can be attributed to Zn-PPIX forming a Zn-His[93] linkage similar to that holding the heme group in *holo*-myoglobin. This linkage makes Zn-PPIX more competitive than PPIX in replacing the heme groups.

The low-pH reaction yields, upon aging for 5 h, up to four protein peaks which are nearly baseline-resolved and well-separated from excess Zn-PPIX. Reactions analyzed some 3 min after mixing contain only two protein peaks. There appears to be a gradual interconversion between isoforms of the fluorescent product. The combined area of the four Zn-PPIX labelled protein peaks gives a maximum area upon immediate analysis, but this signal decreases by 8 and 11% after 2 and 4 h, respectively.

The limit of detection of this method was investigated as described in section 2.2.3.2 and was determined to be 50 nM. The dynamic range is from 0.1 – 5 μM.

2.3.4 Heme Exchange Using Non-Denaturing Conditions

The porphyrin held by myoglobin can also be exchanged without denaturing the protein. Various heme exchanges are possible between (*apo* or *holo*)-hemoglobin and (*apo* or *holo*)-myoglobin, but all can be performed under non-denaturing conditions at neutral pH.[50] This method of labelling presents the simplest conceivable means of generating a fluorescent myoglobin. Here, myoglobin is first diluted to avoid denaturation upon addition of the porphyrin solution, as the latter contains 50% methanol.

The kinetics of this reaction were studied using both PPIX and Zn-PPIX. Reactions with either porphyrin gave a similar profile: immediately, there was a signal from labelled protein which increased to a steady state in approximately 25 min and was stable until at least 3 h after the reaction was initiated. However, two important differences were apparent between the PPIX and the Zn-PPIX reactions. First, the Zn-PPIX reaction gave a signal that was 6 times that of PPIX. Second, due to the more sensitive labelling of myoglobin by Zn-PPIX, the greater protein peak signal could be distinguished as three peaks with the same migration and peak height pattern as seen in Figures 2.6 and 2.7. As the reaction solution ages, the peak area of the first peak (3.71 min) decreases, while that of the second (3.82 min) and third (3.95 min) peaks increases. This suggests that there is a slow interconversion between labelled myoglobin species. However, given that the sum of their signals remains constant for at least 3 h, quantification is still possible. Figure 2.8 shows successive electropherograms of a reaction performed using Zn-PPIX monitored from 3 min to 186 min after the reaction was initiated. The combined area of the three Zn-PPIX labelled protein peaks decreases by only 11% after 3 h, as shown in Figure 2.9. In the case of PPIX labelling, the area decreases by only 4% after nearly 4 h, but the overall sensitivity was lower, as discussed above.

The reported[50] loss or exchange of heme by myoglobin is utilized in this labelling scheme for myoglobin. Not surprisingly, Zn-PPIX labelling gave a greater protein signal (a 6-fold increase) than when PPIX was used. Again, this difference is believed to be caused by a Zn-His[93] linkage which is absent when using PPIX. Compared to low-pH

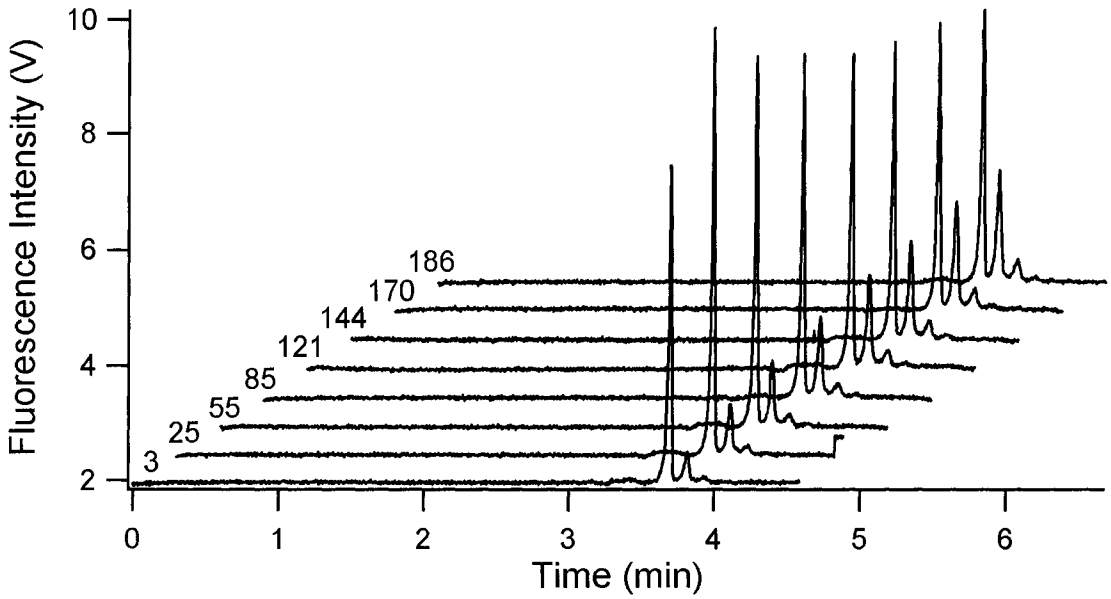

Figure 2.8 Electropherograms of a heme exchange reaction using Zn-PPIX, monitored at various times after the reaction was initiated. Time in minutes is indicated to the left of each trace. Reaction conditions are described in Section 2.2.3.3. Sample was injected at 100 mbar for 6 s; applied voltage was 25 kV; optical filter used was a 450 nm cutoff; background electrolyte was 25 mM borate at pH 9.5. Traces have been offset for clarity.

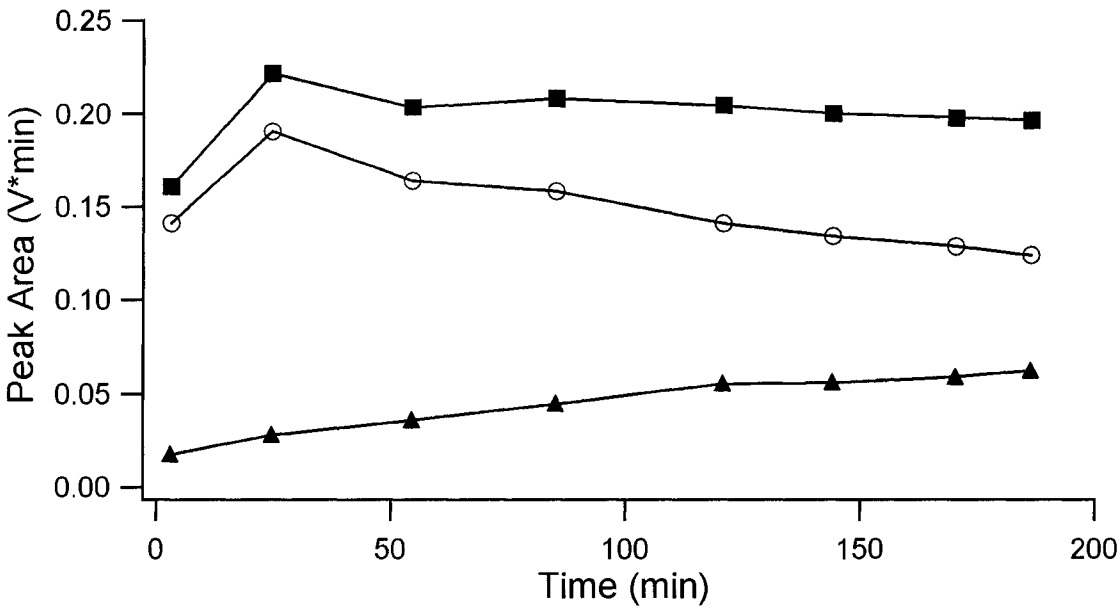

Figure 2.9 Conservation of protein peak area for the non-deanturing labelling of myoglobin with Zn-PPIX. A labelling reaction for myoglobin was sampled repeatedly over ~ 3 h to measure the interconversion between the observed electrophoretic peaks. Filled squares (■) represent the total peak area, open circles (○) represent the first myoglobin peak and filled triangles (▲) represent the second peak. The lines between points serve only as a guide to the eye.

denaturation, this non-denaturing technique gives almost identical peak heights and presumably, comparable sensitivity.

2.3.5 Specificity of the Labelling Reaction

To test whether this procedure is specific to heme proteins, the reactions were performed in the presence of a non-heme protein: bovine serum albumin. Using albumin represents a significant challenge: both human and bovine serum albumin are known to contain two high-affinity heme binding sites,[51] which retain their affinity over the pH range 4 – 10.[52] Thus one would expect BSA to interfere with the labelling reaction by binding the fluorescent porphyrins added to solution. To examine this competitive labelling, BSA was added in an equimolar quantity to myoglobin, as discussed in section 2.2.3.2. The reconstitution reactions were performed by both the urea and low-pH methods. The reactions were performed with and without myoglobin and the results for all four permutations are shown in Figure 2.10. The presence of bovine albumin does not add any additional BSA-PPIX peaks, although the profile of the excess PPIX peaks is distorted relative to electropherograms of solutions where no BSA is present.

Nonetheless, the migration order and times of both myoglobin and PPIX are typical of reactions without BSA. Again it is clear that the use of low-pH denaturation is the more effective labelling method.The robustness of this method has also been tested by examining the effects of excesses of BSA. This is necessary if one wishes to detect, for instance, the disease condition myoglobinuria. Individuals suffering from myoglobinuria have elevated levels of urinary myoglobin (>250 μg/mL *vs.* <5 ng/mL for a healthy person).[53] Individuals who also suffer from kidney disorders can also have albuminuria

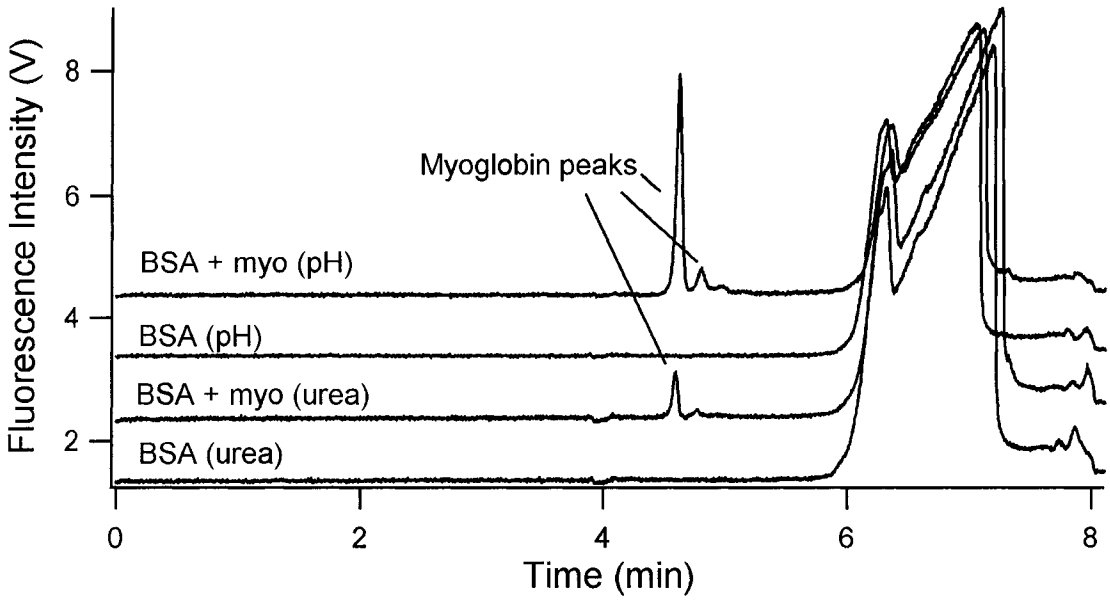

Figure 2.10 Effect of BSA on the reconstitution reaction. The top two traces are for reactions where pH denaturation was used; the bottom two for urea denaturation. Of each pair, the lower trace is for a reaction containing only BSA, while the upper trace is that for a reaction containing both proteins. Reaction conditions are described in Section 2.2.3.2. Sample was injected at 100 mbar for 6 s; applied voltage was 25 kV; optical filter used was a 450 nm cutoff; background electrolyte was 25 mM soduim borate at pH 9.5. Traces have been offset for clarity.

with over 300 μg/mL of urinary albumin.[54] Thus in a worst-case scenario, an analyst would seek to detect a minimal amount of myoglobin in the presence of >4.5 μM albumin. In the following studies, solutions of 50 nM (0.85 μg/mL) final myoglobin concentration and varying concentrations of albumin were analyzed. The initial myoglobin and albumin concentrations ranged from 3.85 μM to 0.238 μM and from 115 μM to 476 μM, depending on the volume of BSA solution added. Albumin molar excesses of 3, 10, 30, 100, 300, 1000 and 2000 have been added to a low-pH reconstitution reaction for myoglobin with the results shown in Figure 2.11. Interestingly, the myoglobin peak area increases gradually by 72% over the range of 3 to 1000-fold molar excess of BSA. Again, no peaks attributed to BSA or any BSA-PPIX adducts are seen. While this dependence of protein peak area on BSA concentration might seem unacceptable, such a large range of BSA is rare in biological samples. For instance, the average human serum BSA level is 42 mg/mL,[55] while *extreme* hypoalbuminemia begins at 18 mg/mL.[56] Quantification should then be conducted by preparation of standard solutions with a normal level of BSA. The dependence of myoglobin signal on BSA concentration should be negligible over the possible range of BSA concentration in serum. Thus, our method is able to analyze well below the clinical definition of myoglobinuria in the presence of at least 476 μM (31.6 mg/mL) BSA, corresponding to severe albuminuria. These studies reveal that the low-pH labelling method is entirely specific to myoglobin in the presence of large excesses of BSA.

When comparing the low-pH denaturation labelling against the heme exchange reaction, the former was found to be more effective. For heme exchange experiments, Zn-PPIX was used as described in Section 2.2.3.3. The latter labelling scheme was

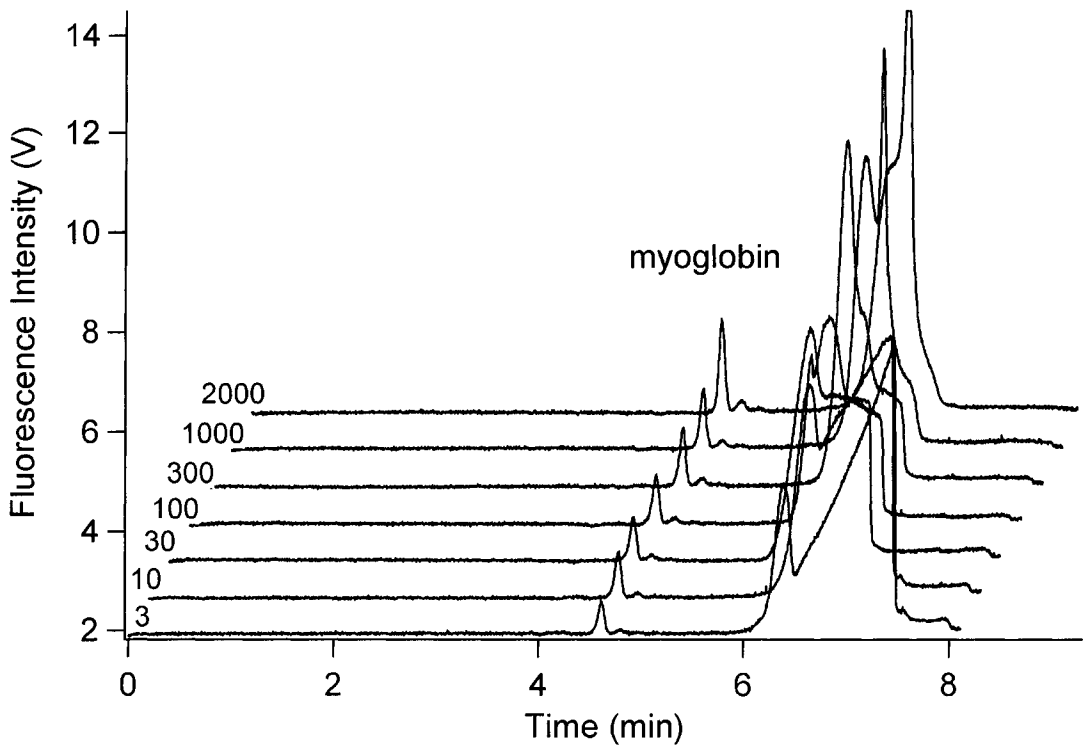

Figure 2.11 Reconstitution reactions with PPIX, performed by low-pH denaturation in the presence of varying amounts of BSA interferent. Molar excess of BSA is indicated to the left of each trace. Reaction conditions are described in Section 2.2.3.2. Sample was injected at 100 mbar for 6 s; applied voltage was 25 kV; optical filter used was a 450 nm cutoff; background electrolyte was 25 mM sodium borate at pH 9.5. Traces have been offset for clarity.

negatively impacted by the presence of BSA, as shown in Figure 2.12. For reference, a similar reaction with no added BSA gave 42% greater signal than the reaction with a 3-fold excess of BSA.

2.4 Conclusions

This chapter shows a novel method for non-covalent, fluorescent labelling of myoglobin for LIF detection in CE. This method is specific for heme proteins and gives a simple reaction product, in contrast to classical labelling reactions which give multiple products. The labelling procedure is rapid, inexpensive and selective. The low-pH method more effectively cleaves the myoglobin-heme bonds than does the use of urea. A direct exchange of porphyrins is also possible, providing a very simple reaction which yields comparable sensitivity to the denaturing methods. The urea denaturation method suffers from a mandatory dilution of the sample during reaction and yields the lowest sensitivity. The low-pH method is the most robust labelling procedure with a detection limit of 50 nM and is robust and selective in the presence of at least a 2000-fold excess of BSA, a protein which could possibly interfere with the reaction. Finally, while the heme exchange reaction can not tolerate BSA, it is comparably sensitive to the low-pH scheme and demonstrates a remarkably simple labelling procedure.

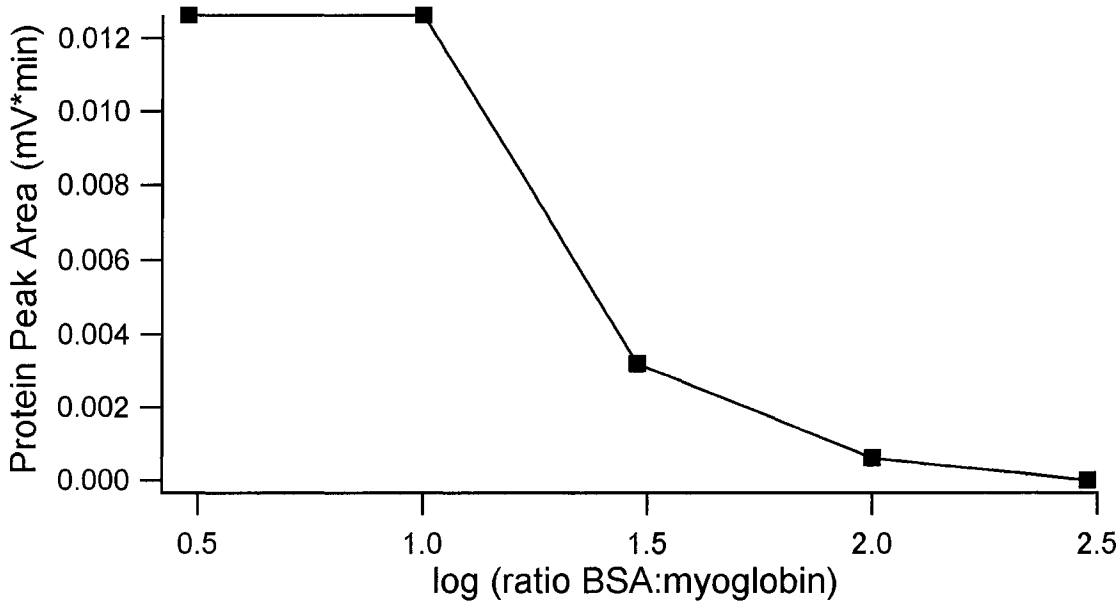

Figure 2.12 Peak area of labelled myoglobin by non-denaturing method using Zn-PPIX vs. log (mole ratio of BSA to myoglobin). Reaction and electrophoretic conditions are described in Sections 2.2.3.3 and 2.2.3.4, respectively. The line between points serves only as a guide to the eye.

2.5 References

(1) Hu, S.; Dambrowitz, A.; Michels, D.; Zhang, L.; Dovichi, N. J. *Radiat. Res.* **2001**, *156*, 444-445.

(2) Hu, S.; Jiang, J.; Cook, L. M.; Richards, D. P.; Horlick, L., *et al. Electrophoresis* **2002**, *23*, 3136-3142.

(3) Chan, K. C.; Muschik, G. M.; Issaq, H. J. *Electrophoresis* **2000**, *21*, 2062-2066.

(4) Swaile, D. F.; Sepaniak, M. J. *J. Liq. Chromatogr.* **1991**, *14*, 869-893.

(5) March, J. C.; Rao, G.; Bentley, W. E. *Appl. Microbiol. Biotechnol.* **2003**, *62*, 303-315.

(6) Miyawaki, A.; Nagai, T.; Mizuno, H. *Current Opinion in Chemical Biology* **2003**, *7*, 557-562.

(7) Zarrine-Afsar, A.; Krylov, S. N. *Anal. Chem.* **2003**, *75*, 3720-3724.

(8) Kiessig, S.; Reissmann, J.; Rascher, C.; Kullertz, G.; Fischer, A., *et al. Electrophoresis* **2001**, *22*, 1428-1435.

(9) Stastna, M.; Radko, S. P.; Chrambach, A. *Electrophoresis* **2001**, *22*, 66-70.

(10) Craig, D. B.; Dovichi, N. J. *Anal. Chem.* **1998**, *70*, 2493-2494.

(11) Zhang, J.; Campbell, R. E.; Ting, A. Y.; Tsien, R. Y. *Nature Reviews Molecular Cell Biology* **2002**, *3*, 906-918.

(12) Chen, D. Y.; Adelhelm, K.; Cheng, X. L.; Dovichi, N. J. *Analyst* **1994**, *119*, 349-352.

(13) Chen, D. Y.; Dovichi, N. J. *Journal of Chromatography B-Biomedical Applications* **1994**, *657*, 265-269.

(14) Colton, I. J.; Anderson, J. R.; Gao, J. M.; Chapman, R. G.; Isaacs, L., *et al. Journal of the American Chemical Society* **1997**, *119*, 12701-12709.

(15) Stoyanov, A. V.; Ahmadzadeh, H.; Krylov, S. N. *J. Chromatogr. B* **2002**, *780*, 283-287.

(16) Moody, E. D.; Viskari, P. J.; Colyer, C. L. *Journal of Chromatography B* **1999**, *729*, 55-64.

(17) Welder, F.; Paul, B.; Nakazumi, H.; Yagi, S.; Colyer, C. L. *J. Chromatogr. B* **2003**, *793*, 93-105.

(18) Colyer, C. L.; Mangru, S. D.; Harrison, D. J. *J. Chromatogr. A* **1997**, *781*, 271-276.

(19) Liu, Y. J.; Foote, R. S.; Jacobson, S. C.; Ramsey, R. S.; Ramsey, J. M. *Anal. Chem.* **2000**, *72*, 4608-4613.

(20) Harvey, M. D.; Bablekis, V.; Banks, P. R.; Skinner, C. D. *J. Chromatogr. B* **2001**, *754*, 345-356.

(21) Sze, N. S. K.; Huang, T. M.; Pawliszyn, J. *Journal of Separation Science* **2002**, *25*, 1119-1122.

(22) Csapo, Z.; Gerstner, A.; Sasvari-Szekely, M.; Guttman, A. *Anal. Chem.* **2000**, *72*, 2519-2525.

(23) Gouterman, M. In *The Porphyrins*; Dolphin, D., Ed.; Academic Press: New York, 1978; Vol. III, pp 1 - 156.

(24) Melanson, J. E.; Lucy, C. A. *Electrophoresis* **2002**, *23*, 1689-1694.

(25) Harris, D. C. In *Quantitative Chemical Analysis,* 5th ed.; Harris, D. C., Ed.; W.H. Freeman and Co.: New York, 1999, pp 533.

(26) *Protein Data Bank*, http://www.rcsb.org/pdb/, Copeland, D.M., West A.H., Richter-Addo, G.B. Proteins: Struct., Funct., Bioinf. (2003) 2053: 2182-2192.

(27) Lamola, A. A.; Yamane, T. *Science* **1974**, *186*, 936 - 938.

(28) Adar, F.; Gouterman, M.; Aronowitz, S. *J. Phys. Chem.* **1976**, *80*, 2184-2191.

(29) Tulp, A.; Verwoerd, D.; Benham, A.; Jalink, K.; Sier, C., *et al. Electrophoresis* **1998**, *19*, 1171-1178.

(30) Philips, J. N. *Reviews of Pure and Applied Chemistry* **1960**, *10*, 35.

(31) Vanderkooi, J. M.; Erecinska, M. *Eur. J. Biochem.* **1975**, *60*, 199-207.

(32) Ye, S. Y.; Shen, C. Y.; Cotton, T. M.; Kostic, N. M. *J. Inorg. Biochem.* **1997**, *65*, 219-226.

(33) Adams, P. A. *Biochem. J.* **1977**, *163*, 153-158.

(34) Kagen, L. J. *Myoglobin; Biochemical, Physiological and Clinical Aspects*; Columbia University Press: New York, 1973.

(35) Griko, Y. V.; Privalov, P. L. *J. Mol. Biol.* **1994**, *235*, 1318-1325.

(36) Tang, Q.; Kalsbeck, W. A.; Olson, J. S.; Bocian, D. F. *Biochemistry* **1998**, *37*, 7047-7056.

(37) Babu, K. R.; Douglas, D. J. *Biochemistry* **2000**, *39*, 14702-14710.

(38) Zheng, Y. B.; Meng, F. G.; Chen, B. Y.; Wang, X. C. *Int. J. Biol. Macromol.* **2002**, *31*, 97-102.

(39) Delli Castelli, D.; Lovera, E.; Ascenzi, P.; Fasano, M. *Protein Sci.* **2002**, *11*, 2273-2276.

(40) Li, S. F. Y. *Capillary Electrophoresis*; Elsevier Science Publishers: New York, 1992.

(41) Jennings, P. A.; Wright, P. E. *Science* **1993**, *262*, 892-896.

(42) Gonnelli, M.; Strambini, G. B. *Biochemistry* **1997**, *36*, 16212-16220.

(43) Tams, J. W.; Welinder, K. G. *Biochem. Biophys. Res. Commun.* **2001**, *286*, 701-706.

(44) Brunori, M.; Giacometti, G. M.; Antonini, E.; Wyman, J. *J. Mol. Biol.* **1972**, *63*, 139-152.

(45) Scolaro, L. M.; Castriciano, M.; Romeo, A.; Patane, S.; Cefali, E., *et al. Journal of Physical Chemistry B* **2002**, *106*, 2453-2459.

(46) Hashimoto, S.; Fukasaka, J.; Takeuchi, H. *J. Raman Spectrosc.* **2001**, *32*, 557-563.

(47) Hughson, F. M.; Wright, P. E.; Baldwin, R. L. *Science* **1990**, *249*, 1544-1548.

(48) Adams, P. A. *Biochem. J.* **1976**, *159*, 371-376.

(49) Morikis, D.; Champion, P. M.; Springer, B. A.; Sligar, S. G. *Biochemistry* **1989**, *28*, 4791-4800.

(50) Rossi-Fanelli, A.; Antonini, E. *J. Biol. Chem.* **1960**, *235*, PC 4-5.

(51) Rosenfeld, M.; Surgenor, D. M. *J. Biol. Chem.* **1950**, *183*, 663-677.

(52) Beaven, G. H.; Chen, S. H.; Dalbis, A.; Gratzer, W. B. *Eur. J. Biochem.* **1974**, *41*, 539-546.

(53) Warren, J. D.; Blumbergs, P. C.; Thompson, P. D. *Muscle & Nerve* **2002**, *25*, 332-347.

(54) Lewis, E. J.; Lewis, J. B. *Clin Exp Nephrol* **2003**, *7*, 1-8.

(55) Ritzmann, S. E.; Daniels, J. C. In *Serum Protein Abnormalities: Diagnostic and Clinical Aspects*; Ritzmann, S. E., Daniels, J. C., Eds.; Little, Brown & Co.: Boston, 1975, pp 3-26.

(56) Beathard, G. A. In *Serum Electrophoresis and Total Serum Proteins*; Ritzmann, S. E., Daniels, J. C., Eds.; Little, Brown & Co,: Boston, 1975, pp 173-212.

CHAPTER THREE. Spectral Filtering of Light Emitting Diodes for Fluorescence Detection[a]

3.1 Introduction

Ongoing improvements in LED technology have made light emitting diodes suitably powerful and stable for optical detection methods. LEDs have been used extensively for fluorescence measurements of atmospheric gases using liquid-core waveguides,[1-10] as the light source in fluorometers,[11-13] for gas sensing[14-20] and in capillary electrophoresis.[21-29] An advantage of LEDs as a light source for fluorescence is that they are commercially available at wavelengths spanning the entire visible spectrum, as well as the mid– and near–UV and near–IR. In contrast, diode lasers are available at only a limited number of wavelengths in the visible and IR. However, LEDs also have a broader spectral bandwidth than diode lasers – typically 30 nm full width at half maximum (FWHM) vs. 1 pm for diode lasers. This polychromaticity can be detrimental in fluorescence measurements, as scattered light from the LED that coincides with the detection wavelength will produce a high background signal. Fluorescence detection limits can be severely degraded if the longer-wavelength LED light reaches the detector.[14, 15] Some studies[16, 18, 19, 21, 22, 26, 29, 30] have used bandpass or short-pass filters to exclude longer-wavelength LED light from being scattered to the detector. However,

[a] A version of this work has been published as E. P. de Jong and C. A. Lucy, "Spectral filtering of light emitting diodes for fluorescence detection", *Analytica Chimica Acta* **2005**, *546*, 37-45.

while the need for spectral filtering with LED fluorescence has obviously been recognized, there has been no systematic study of the effect of spectral filtering.[31, 32]

This chapter provides a detailed study of the importance of filtering both the excitation and the emission light, and provides guidelines for the selection of appropriate filters. The LED excitation light is filtered to remove light at the detection wavelength, and the fluorescence emission is filtered to exclude scattered LED light. In particular, the use of a bandpass filter on the LED excitation beam yielded tremendous gains in signal-to-noise, and consequently in detection limits.

3.2 Experimental

3.2.1 Chemicals

Riboflavin, eosin Y (eosin) and fluorescein sodium salt were from Sigma (St. Louis, MO). Bottles of stock solutions were covered with aluminum foil and stored in the dark to prevent photodegradation. Sodium dodecyl sulfate (SDS, 99+%, ACS reagent, Aldrich, Milwaukee, WI), boric acid (ACS grade; BDH, Poole, England), succinic acid (≥ 99%, Anachemia, Rouses Point, NY) and sodium hydroxide (10 M solution; Fisher, Nepean, ON), were used as received. Ultrapure water was obtained from a Nanopure water system (Barnstead, Dubuque, IO). Buffers were prepared by dissolving an appropriate amount of the conjugate acid in ultrapure water and adjusting the pH with 10 M NaOH while stirring.

3.2.2 LED-Fluorescence

LEDs at three different (nominal) wavelengths were used as the light source: 470 nm (L5T15B), 490 nm (LED490-03U) and 525 nm (B5-433-B525), all from Roithner Lasertechnik (Vienna, Austria). The LED spectra were measured on an Agilent HP 8453 Diode Array UV-Vis spectrometer running UV-Vis Chemstation software (ver. A.06.06, Palo Alto, CA). The LED light was directed at the detector through a neutral density filter (optical density 3.0; Oriel Optics Corp., Stamford, CT) while blocking the UV-Vis source. Absorbance spectra were collected with 1 nm resolution and a 25 s integration time. The absorbance data was converted to %T, normalized to the LED's maximum and smoothed using 2nd order Savitzky-Golay smoothing on 5 points (Appendix 8). The linearity of the LEDs' intensity as a function of operating current was verified (r^2 > 0.977) using a LaserCheck laser power meter (Melles Griot, Carlsbad, CA). An example of this relationship is shown in Appendix 9. A 490 nm LED was flattened and polished,[33] but was found to have lower external efficiency than unaltered LEDs (0.99 mW compared to 1.8 and 1.7 mW). Thus all LEDs were used as received in our studies.

Bandpass filters with center wavelengths of 470, 480 and 490 nm, and 10 nm FWHM (470±5, 480±5 and 490±5) were from Omega Optical (Brattleboro, VT). Bandpass filters centered at 520 and 546 nm with 10 nm FWHM (520±5 and 546±5) were from Edmund Optics (Barrington, NJ, USA). A bandpass filter centered at 520 nm with 20 nm FWHM (520±10) was from Beckman (Fullerton, CA). Long-pass filters with 50 %T at 515 and 530 nm (OG515 and OG530) were purchased from Edmund Optics.

The LED-fluorescence detector is shown schematically in Figure 3.1. The LED was mounted in an in-house built stand. The emitted light was collimated through a

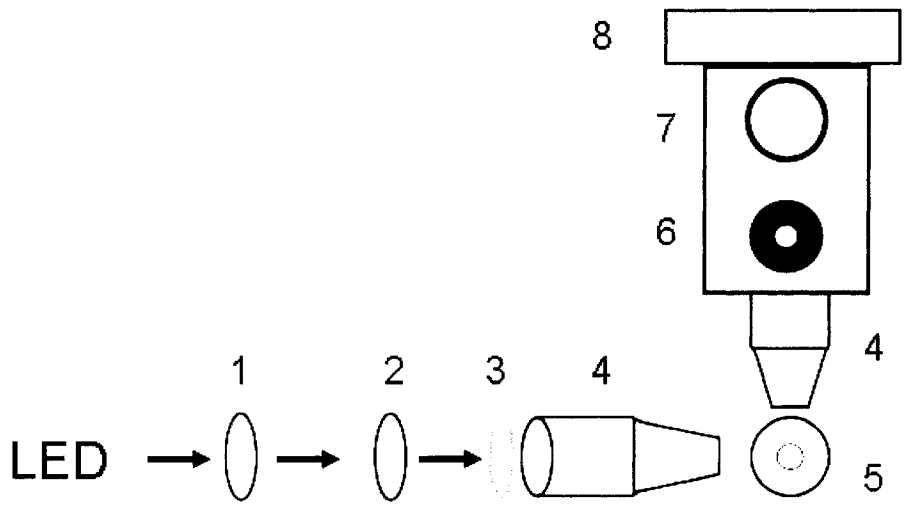

Figure 3.1 Schematic of the LED-fluorescence detector. (1) singlet lens, (2) doublet lens, (3) bandpass filter, (4) 20× microscope objective, (5) capillary, (6) pinhole, (7) bandpass (or longpass) filter, (8) PMT. Figure is not to scale.

singlet glass lens (18 mm focal length, 15 mm diameter; 01LPX017; Melles Griot) and focused towards a 20x microscope objective (Edmund Optics, Barrington, NJ; 017791) by a doublet glass lens (Melles Griot, 21 mm focal length, 14 mm diameter; 01LAO014). In some experiments, a bandpass filter was placed in front of the microscope objective used to focus the light onto the 50 μm ID (360 μm OD) fused-silica capillary (Polymicro Technologies, Phoenix, AZ) used as the sample cell.

The emitted fluorescent light was collected at a right angle to the incident light to minimize scatter. The emitted fluorescence was collected with a 20x microscope objective (as above) and passed through a 1000 μm pinhole (Melles Griot) which provided spatial filtering by rejecting light scattered from the capillary walls.[34] Fluorescence then passed through a bandpass filter prior to impinging upon the photomultiplier tube (R3896; Hamamatsu, Bridgewater, NJ) whose driving voltage was varied by a tunable power supply (manufactured by the Department of Chemistry Electronics Shop; 0 – 1000 V). The signal from the photomultiplier tube was collected by a data acquisition board (National Instruments, Austin, TX), displayed by Virtual Bench Logger software (Version 2.51; National Instruments) at 5 Hz and stored on a Celeron 400 MHz PC. Data was plotted and analyzed using Igor Pro Version 3.12 (WaveMetrics, Lake Oswego, OR). Igor Pro was also used to smooth data in some cases. The entire system is housed in a dark room.

3.2.3 Characterization of Spectral Filters

The sample holder of an Agilent HP 8453 UV-Vis spectrometer was modified to hold the filters perpendicular to the light path. Spectra were collected with 1 nm

resolution from 190 to 900 nm using a 25 s integration time. The center wavelength observed for each filter agreed with their specified nominal values to within 2 nm. All filters had an optical density > 3.5 outside of their transmitting region. The total transmittance of each filter was determined by summing its transmittance at every wavelength across the filter spectrum.

The red and blue edges of the bandpass filters and the roll-off of the long-pass filters were characterized by fitting the edge to a Gaussian distribution using GraphPad Prism 4.00 for Windows (San Diego, CA). The crosstalk (CT) between excitation and emission filter pairs was then calculated using equation 3.1:

$$CT = \Sigma G_{red}(\bar{x}_{red}) \times G_{blue}(\bar{x}_{red}), G_{red}(\bar{x}_{red}+1) \times G_{blue}(\bar{x}_{red}+1), \ldots, G_{red}(\bar{x}_{blue}) \times G_{blue}(\bar{x}_{blue}) \quad \textbf{(3.1)}$$

where $G_{red}(x)$ is the value of the Gaussian function, relative to its maximum value, approximating the red edge of the excitation filter at wavelength x, G_{blue} is the Gaussian function, relative to its maximum, approximating the blue edge of the emission filter and $\bar{x}_{red}$ and $\bar{x}_{blue}$ are the respective means of the Gaussian functions in nm. The LED intensity is expected to impact the background signal, as discussed in Section 3.3.4. However, the LED intensity spans only 2 orders of magnitude, whereas the calculated crosstalk values span over 70. Thus, these values can not be compared mathematically since they are measured in different units and since they span such a different range.

3.2.4 Continuous Flow Analysis

The fluorescence and background signals were determined by continuously flowing solutions of fluorophore or water through the capillary (70 cm of 50 μm ID) using an applied pressure of 2000 mbar. In these experiments, the PMT voltage, the

combination of excitation and emission filters, the LED, and/or the LED's operating current were varied. Dark currents for a given filter set were determined by monitoring the PMT output with the LED off.

3.2.5 Detection Limits

Detection limits were determined using the United States Environmental Protection Agency (EPA) protocol[35] using CE analyses to allow comparison with literature results. In the EPA method, the detection limit is determined based on the signal standard deviation determined for seven replicate injections of dilute sample (at a S/N of 5-10). The optimized bandpass filter combinations were (excitation filter / emission filter): 470±5 / 520±10, 490±5 / 520±10, and 520±10 / 546±5 for riboflavin, fluorescein and eosin, respectively.

In capillary electrophoresis experiments, a Crystal CE system (model 300, ATI Unicam, Boston, MA) was used to control the voltage and pressure. Experiments were performed with 70 cm of 50 μm ID (360 μm OD) fused-silica capillary with an effective length of 65 cm. New capillaries were rinsed at 2000 mbar with 0.1 M NaOH, followed by ultrapure water for at least 10 min each. The capillary was at room temperature (~ 23 °C).

Electropherograms started with a rinse (2000 mbar for 1 min) of background electrolyte (BGE) followed by injection of sample, dipping the inlet end of the capillary in vial of ultrapure water, then BGE, and finally the application of +25 kV. For riboflavin, a 50 μM stock solution was prepared in water; dilutions thereof were injected at 100 mbar for 6 s, and separated in a BGE of 15 mM sodium succinate, pH 6.0.

Fluorescein (56.1 μM stock solution) was dissolved in a BGE of 25 mM sodium borate (pH 9.5) and was injected at 50 mbar for 6 s. Detector bandbroadening was studied using these conditions for fluorescein, but with varying injection pressures (25 – 100 mbar) and times (1.2 – 6 s). Eosin (300 μM stock solution) was also dissolved in 25 mM sodium borate (pH 9.5) but due to its strong counter-eof mobility, it was eluted using micellar electrokinetic chromatography (MEKC). The BGE for eosin was 50 mM SDS in 25 mM sodium borate (pH 9.5). Eosin was also injected at 50 mbar for 6 s.

3.3 Results and Discussion

To use LEDs for fluorescence detection, two factors must be considered. First, the divergent LED light must be efficiently directed towards the sample. LEDs emit a much more divergent beam than lasers. Diode lasers are usually packaged with collimating optics which reduces the beam divergence to ~ 0.1 degrees. Without these optics, a beam with 10 – 20 degree divergence would be observed for a diode laser.[36] LEDs are not usually sold with collimating optics and give a divergent beam with a 16 - 150 degree emission angle, depending on the back-reflecting bowl and the epoxy dome. Fiber optic cables[21, 37] or a combination of lenses and/or microscope objectives[28] have been used to deal with the divergent nature of the LED beam. Lenses are usually used to first produce a collimated and then a focused beam of light. In practice, fully collimated light is never truly achieved due to the back-reflecting bowl and dome-shaped housing of an LED.

The second factor that must be considered is that the LED emission is polychromatic. As discussed in the Section 3.1, the detection limits in LED-fluorescence

can be severely degraded if the longer-wavelength LED light reaches the detector.[14, 15] Thus, both the LED light and sample fluorescence must be spectrally filtered. The LED light is filtered to remove longer wavelengths and the fluorescence emission is filtered to transmit the fluorescence while rejecting scattered LED light. This filtering must satisfy several requirements: the LED emission and the excitation filter must match the fluorophore's excitation spectra; the emission filter must match the fluorophore's emission spectrum; and finally the two spectral filters should exhibit minimal crosstalk while transmitting the maximum fluorescent signal. This last point is the key focus of this chapter. *Crosstalk* refers to the spectral overlap of two spectral filters.[38] Once the best wavelength match between the fluorophore, LEDs and filters has been found, the only parameters that can be adjusted to maximize the signal to background ratio are the bandwidth of the spectral filters and the sharpness of their cutoff edges. The latter can be controlled only in the selection of a filter manufacturer, and we have found that the filters from Omega and Beckman were superior to those from Edmund. Bandpass filters from Edmund have edges which make a transition from 10 – 90 %T over 5 nm, compared to ~ 4 nm for the other suppliers (Table 3.1). As well, the filters from Edmund tend to have lower maximal transmission and weaker optical density in the blocking region. Cut-off filters make the 10 – 90 %T transition over 28 nm.

This chapter demonstrates that the reduction of background signal is easily accomplished as a means to increase the ratio of the signal to background and thus improve the detection limit of the method.

Table 3.1 Properties of the bandpass filters used in this study.

	Supplier	Center λ (nm)	FWHM (nm)	Max. %T	Steepness (nm) [a]	Specified OD [b]
470	Omega	470	10	64	4	≥ 4
480	Omega	480	10	74	3.5	≥ 4
490	Omega	490.5	11	73	3.5	≥ 4
520±5	Edmund	520.5	9	57	5	≥ 3
520±10	Beckman	521	21	65	4	N/A
546	Edmund	547	10	59	5.5	≥ 3
OG515	Edmund	516	N/A	90	28	≥ 3
OG530	Edmund	529	N/A	90	28	≥ 3

[a] Average wavelength spanned by the transition from 10 – 90 %T for the filter's red and blue edges.

[b] Optical density (OD) = -log(%T ÷ 100) in the non-transmitting regions, as specified by the manufacturer.

3.3.1 Focusing the LED Light

A number of different optical configurations have been employed with LEDs as light sources in an open-beam style (i.e., no fiber optic cables). These configurations range in complexity from using no optics[1-7, 9, 27, 33, 39-41] to confocal epi-fluorescence[23] and the use of various lenses.[11, 12, 19, 25, 42-45] We have adopted the latter configuration, as it preserved the most light power, while reducing scatter background signal. LEDs emit light from a greater area than lasers, since the LEDs are packaged with a back-reflecting bowl to direct light forwards. Using high magnification objectives can reduce the beam waist to a narrower spot, and thus reduces scattered light by aligning this spot with the center of the capillary. The use of several microscope objectives (6.3, 10, 20, 40 and 63×) in various combinations for both light focusing and collection of fluorescence was examined. In practice, a 20× objective creates a spot size larger than that attained with a laser (~ 2 mm vs. < 0.5 mm), while a 40× objective yields a spot size of ~ 1 mm. However, the 20× objective has a convenient working distance of 8 mm, while the 40x objective has a working distance of < 1 mm. Thus, due to space constraints near the capillary, the 20× objective was used in the studies detailed in Chapters 3 and 4. This finite focusing of the LED light did degrade the peak efficiency in CE studies, as will be discussed in Section 3.3.7. To reduce this extra-column bandbroadening, epi-fluorescence is investigated in Chapter 4.

3.3.2 Spectral Filtering of LED Light

Compared to a laser, LEDs emit a broad spectral line with a full width at half maximum (FWHM) of 10-70 nm, with 30 nm being most common. Unfortunately, the Stokes' shift for most fluorophores is comparable to the LED bandwidth. For instance, the Stokes' shift for the fluorophores studied herein range from 23 nm for eosin to 55 nm for riboflavin. Thus, it is likely that the LED emission will overlap spectrally with the transmitting portion fluorescence bandpass filter – a situation that is seldom encountered when using a laser as a light source. Bright and co-workers have observed that scattered light from the LED which coincides with the detection wavelength produces a high background signal.[14, 15]

The importance of scattered LED light on fluorescence detection can be illustrated using riboflavin. Riboflavin has a large Stokes' shift (55 nm), and so should be less affected by scattered LED light than most fluorophores. Riboflavin was excited using a 467 nm LED, with and without a 470±5 bandpass filter. In both cases the fluorescence emission was collected with a 520±10 bandpass filter. Use of the 470 nm filter increased the signal-to-background ratio 70-fold. Thus, substantial improvements in detectability were achieved using spectral filtering for riboflavin. The improvements in signal to background ratio would be even greater for fluorophores that possess a smaller Stokes' shift.

Filters with a narrow FWHM would decrease the filter crosstalk and thus the background. However narrow bandwidth filters also reduce the flux of excitation light that reaches the sample and reduce the amount of fluorescence that reaches the detector.

Both of these reductions would result in a reduced signal. These effects are investigated in detail in the following sections, with a particular focus on the background signal.

3.3.3 Effect of Filter Bandwidth on Sensitivity

The effect of filter bandwidth on sensitivity was examined using eosin and fluorescein as analytes (Table 3.2). The sensitivity is the change in (background corrected) fluorescence signal per unit concentration, and was determined by passing a series of standards (1 to 10 μM) of each fluorophore through the capillary with each spectral filter set and LED. The 520±5 and 520±10 filters have different maximum %T, and thus their transmission does not scale linearly with their FWHM. To correct for this the total transmission of the 520 nm filters was determined and is reported in Table 3.2.

Increasing the bandwidth of the 520 nm excitation filter significantly increases the sensitivity of eosin (Table 3.2). This is to be expected, as the wider bandwidth would allow more LED light to reach the sample, thereby increasing sensitivity. However while the total transmission of the 520 filter increased 2.5 fold, the sensitivity increased only 2.15 fold. Eosin's excitation spectrum has a FWHM of 22 nm and the LED emits with a FWHM ~30 nm. Thus as the excitation filter's FWHM is broadened, the sensitivity does not increase proportionally, due to reduced absorbance by the fluorophore and reduced light intensity at the outer wavelengths of the LED's emission. Thus, as the bandwidth of the excitation filter is increased, sensitivity increases by a diminishing factor as the bandwidth of the filter approaches that of the fluorophore and LED.

The effect of varying the bandwidth of the emission filter was studied using fluorescein (Table 3.2). In this case, the sensitivity increases 2.56 fold, consistent with

Table 3.2 Sensitivity study examining the effect of excitation and emission filter bandwidth.

Analyte	Filter combination (excitation / emission)	Total transmittance (%T nm) [a]	Sensitivity (V μM^{-1})
Eosin	520±5 / 546	510.1	0.577
Eosin	520±10 / 546	1276	1.24
Fluorescein	490 / 520±5	510.1	0.573
Fluorescein	490 / 520±10	1276	1.47

[a] Total transmittance of the 520 nm bandpass filters.

the 2.5 fold increase in the total transmittance of the filter. Fluorescein emits with a FWHM of 34 nm, so both the ±5 and ±10 nm bandpass filters capture a relatively constant portion of the fluorescein emission spectrum. This suggests that if one can afford to increase filter crosstalk, it is best done using the emission filter. Using a broader bandwidth emission filter will usually give more linear gains in sensitivity because the nonlinearity arises only from the analyte emission. In contrast, sensitivity increases arising from increasing bandwidth of the excitation filter may be compromised by both the LED emission spectrum and the analyte excitation spectrum.

3.3.4 Reduction of Background Signal

The background signal in fluorescence detection arises from the PMT dark current, scattered LED light transmitted in the crosstalk region or in other regions where the filters should not be transmissive, and from auto-fluorescence of the filters. In our system, only dark current and scattered LED light were significant sources of background. This is due in part to the extensive spatial filtering that results from the use of microscope objectives and the pinhole filter. In other systems which do not possess these measures to reduce scattered light, the spectral filtering described here may have insufficient optical density to block LED light. To determine the crosstalk, the transmittance spectrum of each filter was measured as described in Section 3.2.3 (e.g., Figure 3.2, solid line). In the crosstalk region, all filters are < 5% transmissive and in most cases < 0.1%. Thus it is necessary to fit the filter transmittance to a function that allows extrapolation to the low %T values in the crosstalk region. Due to the rectangular profile of the filter spectra, a single Gaussian does not fit the filter transmittance (dot-

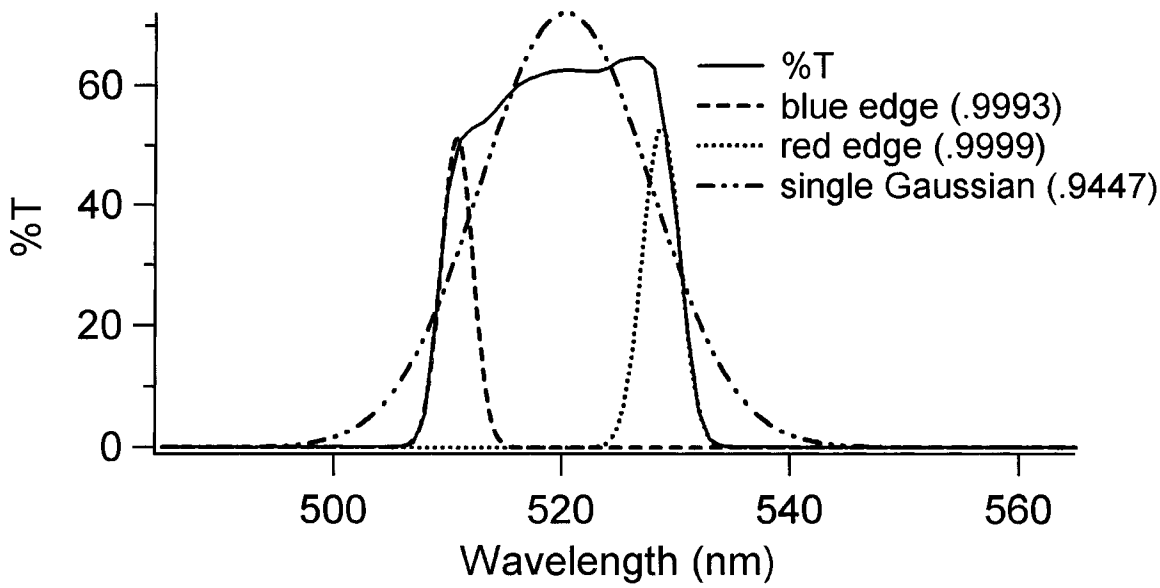

Figure 3.2 Example of curve-fitting using a single Gaussian compared to a Gaussian for each edge of the 520±10 filter. The blue edge is fit up to 511 nm and the red edge from 529 nm upwards. Correlation coefficients (r^2) for each fit in brackets. The data is fit using nonlinear regression.

dash line in Figure 3.2), particularly at the edges, which are of importance to the crosstalk. Since the crosstalk is a function only of the edges of the filters, it is actually only necessary to fit the red- and blue- edges of the excitation and emission filters, respectively (dotted lines). This is illustrated in Figure 3.3. For all of the filters the correlation coefficient (r^2) between the edge of the filter spectrum and the representative section of the Gaussian distribution was greater than 0.9975.

Using the Gaussian fits to the filter edges, the filter crosstalk can be determined from the overlap between the red- and blue- edges of two adjacent filters, as shown in the inset of Figure 3.3. The calculation procedure is described in Section 3.2.3, Equation 3.1. Figure 3.4 shows the effect of filter crosstalk on the background observed for LEDs operating at 30 mA. The curve in Figure 3.4 is the fit of the data to an exponential equation ($r^2 = 0.94$). At low crosstalk values ($<10^{-20}$) the background is dictated by the PMT dark current. At high crosstalk values ($>10^{-20}$), scattered LED light dominates the background.

Two important conclusions can be drawn from the graph. First, the use of long-pass filters alone (e.g., OG515 or OG530) is inappropriate with LED-fluorescence detectors. Their shallow cut-off edges (10-90% over 28 nm) make them ineffective at both eliminating LED scatter while still transmitting fluorescence signal. For instance, the filter combination of 490±5 / OG515 would initially appear suitable for fluorescein ($\lambda_{em,max}$ = 521 nm), since the emission filter reaches 50% of its maximal transmittance at 515 nm. However, the resulting background signal of 1.83 V shows that far too much LED scatter is transmitted. The next available long-pass filter is the OG530. While the 490±5 / OG530 combination yields a much lower background signal (0.31 V), the filter is

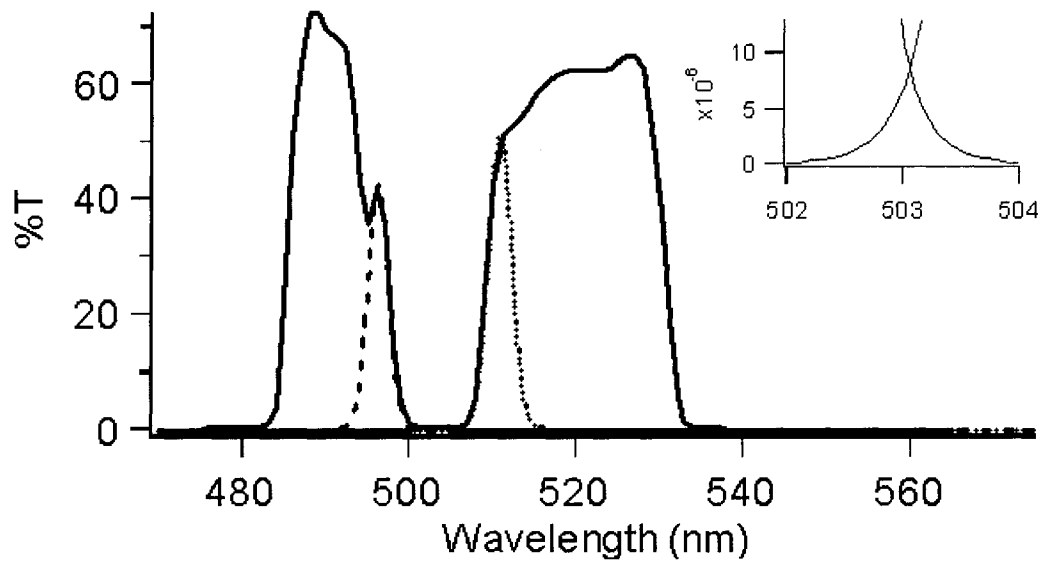

Figure 3.3 Example of Gaussian curves (dashed and dotted lines) generated to model the blue and red edges of the bandpass filters. Shown here are the transmission spectra of the 490±5 and the 520±10 filters (solid lines). Inset: expanded view of the crosstalk between Gaussian curves.

only 20% transmissive at 521 nm and so would yield poor sensitivity. While not observed here, such colored glass filters frequently exhibit auto-fluorescence,[34] which would further degrade the background.

Second, as the center wavelength difference between the two filters is decreased, the background may either be unaffected or increase dramatically. For instance, in moving from the 470 / 520±5 excitation / emission filters (label 2 in Figure 3.4) to the 490 / 520±5 filter set (label 3 in Figure 3.4), the background remains constant at 0.02 V. These filter sets are in the plateau region of Figure 3.4 (crosstalk $<10^{-20}$). In this region the background signal (0.02 V) arises solely from the dark current of the PMT. The two filters prevent scattered LED light from reaching the detector. Alternately, with the 470 / 490 excitation / emission filter set (label 5 in Figure 3.4), the background is 0.13 V. When the filter set is changed to 470 / 480, the PMT saturates (> 10 V) and is off scale on Figure 3.4. The reason for this behavior can be understood by examining the crosstalk. The crosstalk ($\sim 10^{-10}$) with the 470/490 filter pair allows some scattered LED light to reach the detector, raising the background above that due to dark current alone. Decreasing the center wavelength difference results in increased crosstalk ($10^{1.7}$) and thus much more scattered light reaches the detector. The intensity of the LED emission in the crosstalk region also affects the background signal. The spectral power, or intensity, emitted by all three LEDs used here is linearly ($r^2 > 0.977$) related to the operating current. Plots of background signal vs. crosstalk of the filters for a range of LED operating currents are shown in Figure 3.5. For filter sets with crosstalk greater than 10^{-9} (e.g., 470/490), linear relationships ($r^2 > 0.90$) between background signal and LED intensity were observed. Under such filtering conditions, increasing LED intensity would

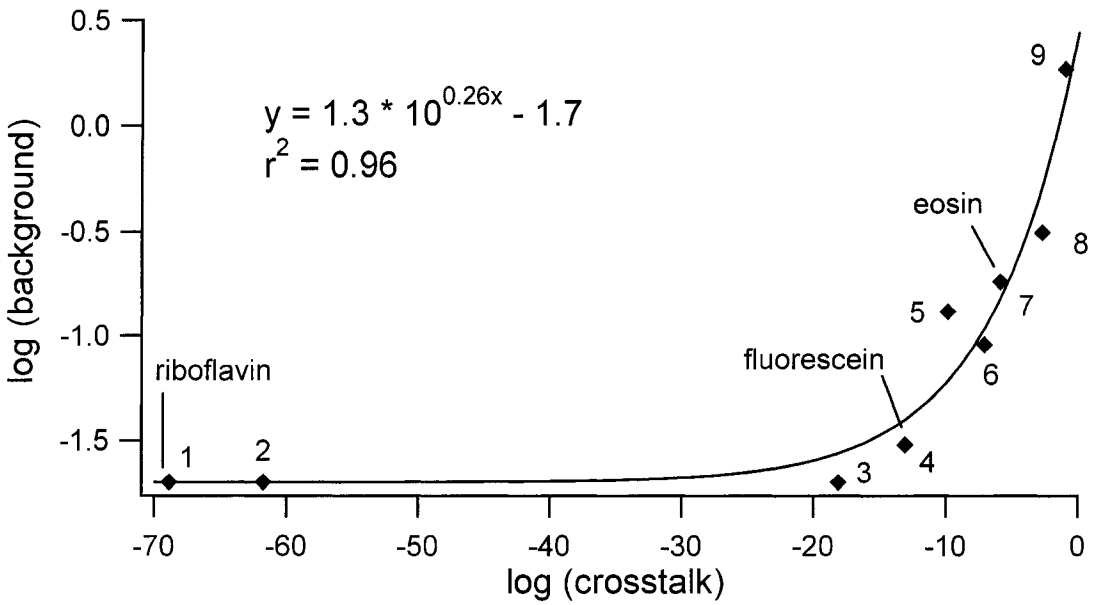

Figure 3.4 Relationship between the background signal and the crosstalk of the bandpass filters. In this plot, all LEDs were run at 30 mA. The filter combinations (data points) are: (1) 470/(520±10), (2) 470/520, (3) 490/520, (4) 490/(520±10), (5) 470/490, (6) 520/546, (7) (520±10)/546, (8) 490/OG530, (9) 490/OG515. All filters have a FWHM of ±5 nm, except for 520±10, OG530 and OG515. See text for filter descriptions. The solid curve is a fit of the data using nonlinear regression.

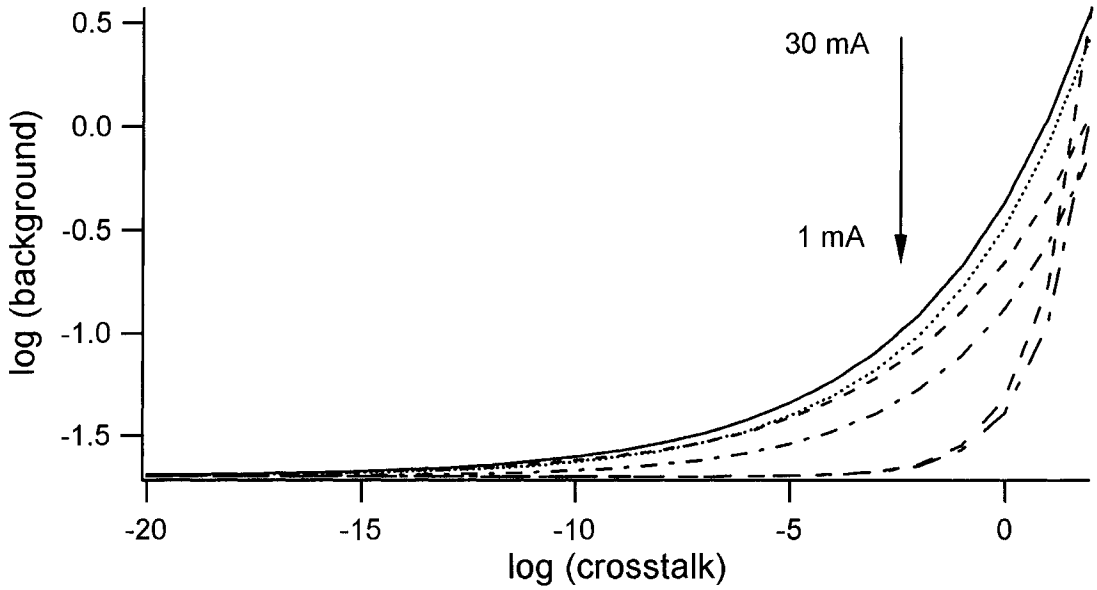

Figure 3.5 Effect of crosstalk on background signal. LEDs operated at 30, 22.5, 15, 7.5, 2 and 1 mA were used to determine the background signal for a given filter pair of known crosstalk.

not be expected to significantly improve detection limits. Filter combinations with crosstalk below 10^{-9} (e.g., 490/520) displayed background signals that did not change with LED intensity. Under such filtering conditions, detection limits can be improved by increasing LED intensity and increasing the bandwidth of the filters.

Finally, it should also be noted that in an epi-fluorescence configuration (Chapter 4, where the excitation and emission light are delivered and collected by the same microscope objective),[46] scattered emission light from the LED would be separated from emitted analyte fluorescence by the use of a dichroic mirror. The steepness of a transmittance curve for a dichroic mirror is comparable to that of a bandpass filter. A dichroic mirror can be approximated as two bandpass filters which intersect at 50 %T, whereas useful filter combinations used in this work overlap at < 0.5 %T. The filter combination of 470±5 and 480±5, which overlap at the highest %T value studied (35%), gives a signal that saturates the PMT under normal operating conditions. Thus, it would seem that a dichroic mirror alone would be unsatisfactory for use with an LED as the excitation source. However, a dichroic mirror with a favorable transition wavelength could serve as either the excitation or emission filter.

3.3.5 Manual Estimation of Crosstalk

The fitting of the red and blue edges of the excitation and emission filters to Gaussian curves (Figure 3.3) allows the filter crosstalk to be estimated, and subsequently optimized. However, this procedure requires that the filter spectrum be in digital form (available from some suppliers, such as the Curv-o-matic service offered by Omega Optical[47]), and the availability of fitting software such as GraphPad Prism. To

circumvent these requirements, three simpler methods for estimating the crosstalk were explored.

In the first method, the manufacturer's nominal specifications were used to generate a single Gaussian that would approximate the filter spectrum. This Gaussian could be used to estimate the crosstalk between two filters. For instance, the 520±10 filter could be approximated by a Gaussian with an amplitude of 70 (assuming 70% maximum transmittance), a mean of 520, and a standard deviation of 8.49 (based on the Gaussian width at half maximum of 2.35σ). However, the crosstalk estimated in this manner can differ from the correct value by 60 orders of magnitude! Not surprisingly plots of the resultant log (crosstalk) vs. log (background), equivalent to Figure 3.4, showed significant scatter ($r^2 < 0.58$) and provided no guidance for proper filter selection. The second method of estimating the crosstalk was to fit the entire filter spectrum to a single Gaussian. An example of such a fit is shown in Figure 3.2. The correlation coefficient appears reasonable (e.g., $r^2 = 0.93$ for the fit in Figure 3.2), but the fit to the filter edge (which is critical to the determination of the crosstalk) is very poor. Furthermore, the cutoff edge of a long-pass filter could not be estimated by either of these methods. Thus, it is imperative that the spectrum of the filter be obtained, be it in digital format or in graphical form.

With a printed version of a filter's spectrum, the filter can be described by manually estimating a Gaussian curve to describe each of its edges. This is illustrated in Figure 3.6 for the 480±5 filter. From each of the outer features near the top of the spectrum, a vertical line is drawn to the baseline. This forms the centre wavelength (i.e., the mean) of the Gaussian distribution used to describe the edge. The height of each of

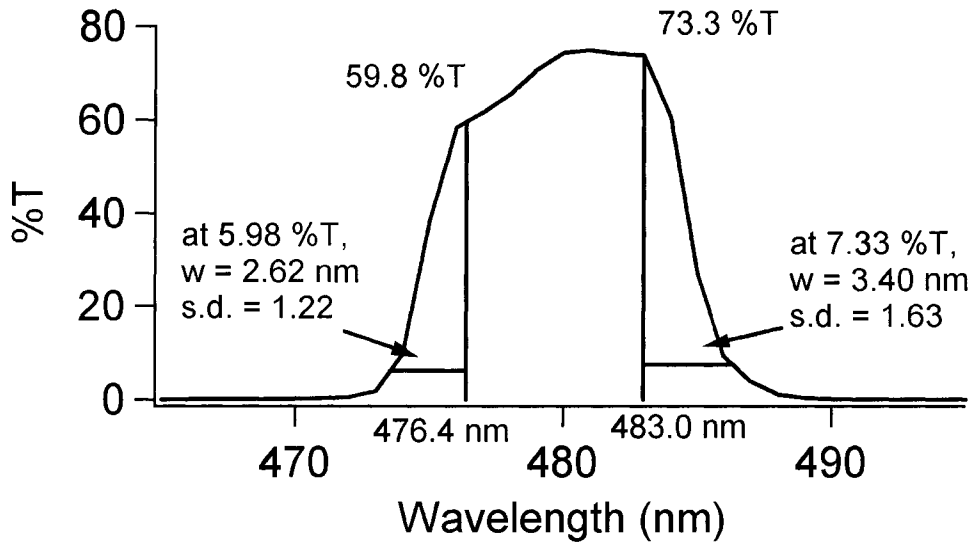

Figure 3.6 Example of estimating the filter edge parameters. Simple measurements from a filter's spectrum can be used to extract the parameters of the Gaussian function describing its edges. For the 480±5 filter, the Gaussian for its blue edge has a centre wavelength of 476.4 nm and standard deviation of 1.22.

these lines is the amplitude of the Gaussian function. Finally, at 10% of the height, a horizontal line is drawn from the centre line to edge of the spectrum. The length of this half-width, in nm, is equal to 2.146 standard deviations. Thus all three parameters of the Gaussian function are obtained and can now be used to calculate the crosstalk. In the given example, the blue edge Gaussian fit the experimental data with $r^2 = 0.983$, compared to $r^2 = 0.998$ for the fit using Prism. Using this estimation method for the complete set of spectral filters produces a new set of crosstalk values. The correlation between crosstalk calculated by the estimation and the digital method is excellent: a log-log plot comparing these values gives a slope of 0.988 and $r^2 = 0.993$ (Appendix 10).

The simplified method then, consists of estimating the crosstalk for a given filter set and interpolating this value using Figure 3.4 or 3.5. If the crosstalk is significantly less than the point where the curve begins to roll off, the combination of filters is too stringent and signal is being lost as a result. Conversely, if the crosstalk is greater than the roll-off point, excess background signal will be generated.

3.3.6 Detection Limits

The criteria for selecting spectral filters for LED-fluorescence are demonstrated for three fluorophores with differing ease of detection. The key spectral parameters of these fluorophores are summarized in Table 3.3. Riboflavin has a generous Stokes' shift of 55 nm at wavelengths very well suited for commercially available LEDs and bandpass filters. Fluorescein's excitation and emission spectra are also located at convenient wavelengths, but its Stokes' shift is only 29 nm. Finally, eosin has a Stokes' shift of 23 nm and the emission of the most appropriate LED (520 nm) is centered on the red edge of

Table 3.3 Spectral properties of the fluorophores studied.

	Riboflavin	Fluorescein	Eosin Y
Extinction coefficient, ε ($L \cdot mol^{-1} \cdot cm^{-1}$)	11,000	93,000	98,000
Fluorescence quantum yield, φ_F	0.30	0.93	0.2
$\lambda_{max,\ excitation}$ (nm)	469	492	518
$\lambda_{max,\ emission}$ (nm)	524	521	541
LED used	467 ± 11 nm	492 ± 14 nm	520 ± 20 nm
Excitation filter	470 ± 5	490 ± 5	520 ± 10
Emission filter	520 ± 10	520 ± 10	546 ± 5
LOD, literature	1.3 μM [a]	5 μM [b], 1 nM [c]	–
LOD, this work	50 nM	3 nM	20 nM

[a] Ref. 44

[b] Ref. 22

[c] Ref. 26

eosin's excitation spectrum (λ_{max} = 518 nm), overlapping the emission spectrum. These conditions make eosin the most challenging fluorophore studied here. Indeed it is not always possible to find an LED with the ideal wavelength. This wavelength mismatch is especially prevalent when working in the "green gap" near 550 nm.[48] To the best of our knowledge, there are no commercially available LEDs available between 535 and 565 nm. When the LED peak wavelength is located between the fluorophore's excitation and emission maxima, filter selection becomes even more important. Depending on the availability of LED peak wavelengths, it might be advantageous to choose an LED and filter at a wavelength shorter than the fluorophore's maximum excitation. This would reduce scatter background, but also compromise the fluorescent signal. The primary goal should be to find an LED whose peak wavelength best matches the fluorophore's spectrum, and then find filters accordingly. Estimation of the resulting crosstalk can be used to select the required bandwidth of the filters. Here it becomes necessary to purchase high quality bandpass filters, since low quality filters exhibit a more shallow transition (for ±5 nm filters, the transition from 10 – 90 %T occurs over 5 nm vs. 4 nm for high-quality filters) and lower opacity (specified optical density of ≥ 3 vs. ≥ 5) outside of their transmitting region. As stated previously, emission filters with a broader FWHM are beneficial so long as excess crosstalk ($>10^{-9}$) is not generated.

The most effective filter combinations for each fluorophore are indicated in Table 3.3, along with the detection limits achieved. As well, Figure 3.7 shows an electropherogram of fluorescein near its detection limit of 3 nM. The dynamic range was from 10 nM – 5 μM. These detection limits compare well with other studies where

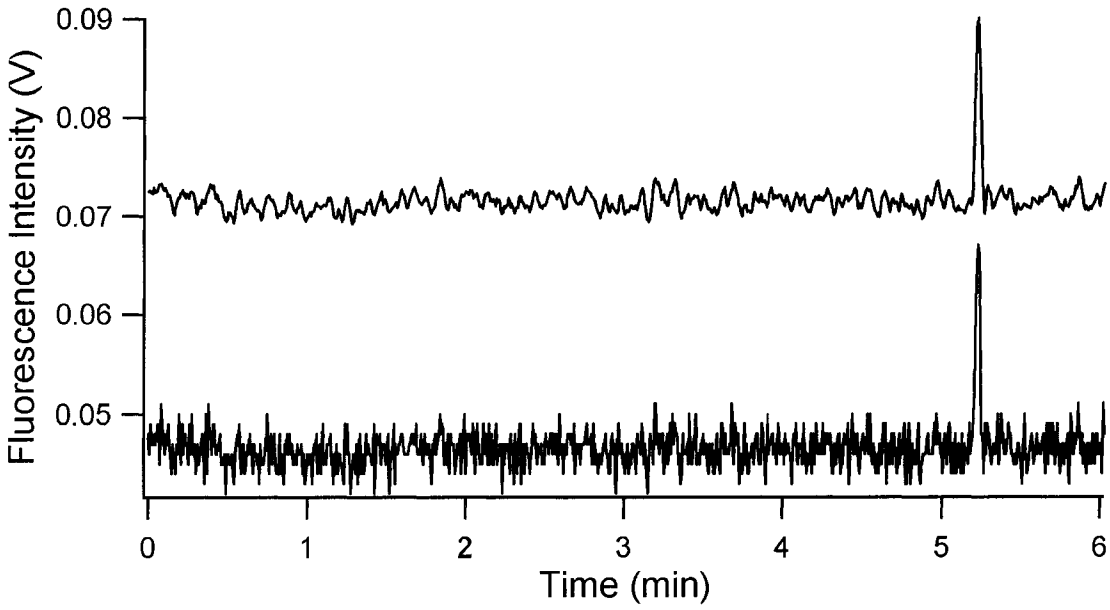

Figure 3.7 Electropherogram of 10 nM fluorescein. Top trace, offset vertically, displays smoothed data from the bottom trace, using 4th-order Savitzky-Golay smoothing on 15 points. **CE conditions:** 25 mM sodium borate background electrolyte at pH 9.5; sample injected at 50 mbar for 6 s; electrophoresis performed at +25 kV; PMT operated at 600 V.

bandpass filters were used to modify the LED excitation light. We estimate concentration detection limits of 5 μM, 500 nM, 39 nM and 1 nM (on a per-fluorophore basis) based on the values reported in references 22, 21, 29, and 26, respectively. The latest report[26] took advantage of the high-power (150 mW) LEDs which have recently come available. References 21 and 29 are omitted from Table 3.3, since these reports used different fluorophores, LEDs and spectral filters than those studied here, making comparison impossible. For both riboflavin and fluorescein, the background signal results only from the PMT dark current. Compared to fluorescein, riboflavin's higher detection limit correlates exactly with its lower extinction coefficient (ε) and fluorescence quantum yield (ϕ_F). However, the very low crosstalk between the filters used for riboflavin (1.42×10^{-69}) indicates that the LOD could have been improved if wider bandwidth filters had been available.

For eosin, the optimized filters yielded a background signal that is greater than the dark current and thus no comparison of its detection limit can be made based on arguments that consider only the extinction coefficient and fluorescence quantum yield. However, after accounting for the difference in $\varepsilon \times \phi_F$ between fluorescein and eosin, the detection limit for eosin is only 1.5 times that of fluorescein. This difference arises from the greater background signal for the filter combination used for eosin and the slight mismatch of the LED spectrum and the excitation spectrum of eosin. This demonstrates that the use of bandpass filters allows the use of an LED whose peak wavelength is very close to the analyte's emission spectrum. The resulting decrease in sensitivity or increase in detection limit is minimal for eosin.

3.3.7 Detector Bandbroadening

To determine the impact of the large spot size of the focused LED, a CE study of the resulting detector bandbroadening was performed. The effect of injection time on the efficiency and peak height for a series of hydrodynamic injections at 25 mbar was determined using 5.61 μM fluorescein. The efficiency increased as the injection time was decreased from 6.0 s to 2.5 s. For injection times below 2.5 s, the efficiency became constant at 700×10^3 plates, indicating that injection bandbroadening no longer contributes to the overall bandbroadening. Using a diffusion coefficient of 5.1×10^{-6} $cm^2 \cdot s^{-1}$ for fluorescein,[49] the theoretical efficiency[50] is predicted to be 1100×10^3 plates. The detector does indeed contribute to the bandbroadening but efficiency is not being seriously degraded. Nonetheless, detector bandbroadening is a factor that needs to be characterized and reported for LED-fluorescence systems. Assuming a finite detector response volume ($\sigma^2_{(det)} = l^2_{(det)}/12$), the effective detector length is estimated to be 1.8 mm.[51] Ideally, the effective detector length should be less than 0.65 mm, so as to cause minimal (<10%) degradation in efficiency.[50] Thus, a shorter detection region is desirable, but as stated, space constraints near the capillary prohibit the use of higher magnification microscope objectives. Other approaches to reducing the detector band broadening with LED fluorescence are being explored. Sheath flow detection and epi-fluorescence geometries are discussed in Sections 4.3.3.3 and 4.3.3.2.

3.4 Conclusions

The use of LEDs as light sources for optical detection methods is very attractive due to their small size, simplicity and low cost. However, their divergent beam and

polychromatic light must be accounted for. Since the LED's spectral emission can overlap with the fluorescence, it becomes necessary to spectrally filter not only the fluorescence, but also the LED light. We have demonstrated that a 70-fold improvement in signal to background can be achieved by spectral filtering of the LED with bandpass filters. While the center wavelength of the filters is determined by the spectra of the fluorophore, the bandwidth of the filters can be used to optimize the signal to background ratio. We have demonstrated a simple method for determining the appropriate filter bandwidth. With optical filtering of 5 mW LEDs, we have achieved detection limits as low as 3 nM in capillary electrophoresis.

3.5 References

(1) Dasgupta, P. K.; Zhang, G. F.; Li, J. Z.; Boring, C. B.; Jambunathan, S.; Al-Horr, R. *Analytical Chemistry* **1999**, *71*, 1400-1407.

(2) Li, J. Z.; Dasgupta, P. K. *Analytical Chemistry* **2000**, *72*, 5338-5347.

(3) Li, J. Z.; Dasgupta, P. K. *Analytical Sciences* **2003**, *19*, 517-523.

(4) Li, J. Z.; Dasgupta, P. K.; Genfa, Z.; Hutterli, M. A. *Field Analytical Chemistry and Technology* **2001**, *5*, 2-12.

(5) Li, J. Z.; Dasgupta, P. K.; Li, G. G.; Motomizu, S. *Analytical Chemistry* **2003**, *75*, 6753-6758.

(6) Li, J. Z.; Dasgupta, P. K.; Tarver, G. A. *Analytical Chemistry* **2003**, *75*, 1203-1210.

(7) Toda, K.; Dasgupta, P. K.; Li, J. Z.; Tarver, G. A.; Zarus, G. M.; Ohira, S. *Analytical Chemistry* **2001**, *73*, 5716-5724.

(8) Toda, K.; Dasgupta, P. K.; Li, J. Z.; Tarver, G. A.; Zarus, G. M.; Ohira, S. *Analytical Sciences* **2001**, *17 Supplement*, i407 - i410.

(9) Toda, K.; Ohira, S.; Tanaka, T.; Nishimura, T.; Dasgupta, P. K. *Environmental Science & Technology* **2004**, *38*, 1529-1536.

(10) Wang, S. L.; Huang, X. J.; Fang, Z. L.; Dasgupta, P. K. *Analytical Chemistry* **2001**, *73*, 4545-4549.

(11) Alexander, T. A.; Gao, G. H.; Tran, C. D. *Applied Spectroscopy* **1997**, *51*, 1603-1606.

(12) Hart, S. J.; JiJi, R. D. *Analyst* **2002**, *127*, 1693-1699.

(13) Smith, B. W.; Jones, B. T.; Winefordner, J. D. *Applied Spectroscopy* **1988**, *42*, 1469-1472.

(14) Cho, E. J.; Bright, F. V. *Analytical Chemistry* **2001**, *73*, 3289-3293.

(15) Cho, E. J.; Bright, F. V. *Analytica Chimica Acta* **2002**, *470*, 101-110.

(16) Hauser, P. C.; Liang, C. L. C.; Muller, B. *Measurement Science & Technology* **1995**, *6*, 1081-1085.

(17) Holthoff, W. G.; Tehan, E. C.; Bukowski, R. M.; Kent, N.; MacCraith, B. D.; Bright, F. V. *Analytical Chemistry* **2005**, *77*, 718-723.

(18) Muller, B.; Hauser, P. C. *Analyst* **1996**, *121*, 339-343.

(19) Potyrailo, R. A.; Hieftje, G. M. *Analytica Chimica Acta* **1998**, *370*, 1-8.

(20) Watkins, A. N.; Wenner, B. R.; Jordan, J. D.; Xu, W. Y.; Demas, J. N.; Bright, F. V. *Applied Spectroscopy* **1998**, *52*, 750-754.

(21) Bruno, A. E.; Maystre, F.; Krattiger, B.; Nussbaum, P.; Gassmann, E. *Trac-Trends in Analytical Chemistry* **1994**, *13*, 190-198.

(22) Chabinyc, M. L.; Chiu, D. T.; McDonald, J. C.; Stroock, A. D.; Christian, J. F.; Karger, A. M.; Whitesides, G. M. *Analytical Chemistry* **2001**, *73*, 4491-4498.

(23) Dang, F.; Zhang, L.; Hagiwara, H.; Mishina, Y.; Baba, Y. *Electrophoresis* **2003**, *24*, 714-721.

(24) Hart, S. J.; Jiji, R. D. *Analytical and Bioanalytical Chemistry* **2002**, *374*, 385-389.

(25) Hillebrand, S.; Schoffen, J. R.; Mandaji, M.; Termignoni, C.; Grieneisen, H. P. H.; Kist, T. B. L. *Electrophoresis* **2002**, *23*, 2445-2448.

(26) Kuo, J. S.; Kuyper, C. L.; P.B., A.; Fiorini, G. S.; Chiu, D. T. *Electrophoresis* **2004**, *25*, 3796 - 3804.

(27) Uchiyama, K.; Xu, W.; Qiu, J. M.; Hobo, T. *Fresenius Journal of Analytical Chemistry* **2001**, *371*, 209-211.

(28) Wang, S. C.; Morris, M. D. *Analytical Chemistry* **2000**, *72*, 1448-1452.

(29) Webster, J. R.; Burns, M. A.; Burke, D. T.; Mastrangelo, C. H. *Analytical Chemistry* **2001**, *73*, 1622-1626.

(30) Wolfbeis, O. S.; Schaffar, B. P. H.; Kaschnitz, E. *Analyst* **1986**, *111*, 1331-1334.

(31) Guibault, G. G. In *Comprehensive Analytical Chemistry*; Svehla, G., Ed.; Elsevier Scientific: Amsterdam, 1977; Vol. VIII, pp 71 - 205.

(32) Seitz, W. R. In *Treatise on Analytical Chemistry*; Elving, P. J., Meehan, E. J., Kolthoff, I. M., Eds.; John Wiley & Sons: New York, 1981; Vol. 7, pp 159 - 248.

(33) Dasgupta, P. K.; Eom, I. Y.; Morris, K. J.; Li, J. Z. *Analytica Chimica Acta* **2003**, *500*, 337-364.

(34) Wu, S. L.; Dovichi, N. J. *Journal of Chromatography* **1989**, *480*, 141-155.

(35) Harris, D. C. In *Quantitative Chemical Analysis,* 5th ed.; Harris, D. C., Ed.; W.H. Freeman and Co.: New York, 1999, pp 89-90.

(36) Imasaka, T. *Talanta* **1999**, *48*, 305-320.

(37) Liu, M. S.; Amirkhanian, V. D. *Electrophoresis* **2003**, *24*, 93-95.

(38) http://www.chroma.com/resources/index.php.

(39) Chediak, J. A.; Luo, Z. S.; Seo, J. G.; Cheung, N.; Lee, L. P.; Sands, T. D. *Sensors and Actuators a-Physical* **2004**, *111*, 1-7.

(40) Edel, J. B.; Beard, N. P.; Hofmann, O.; DeMello, J. C.; Bradley, D. D. C.; deMello, A. J. *Lab on a Chip* **2004**, *4*, 136-140.

(41) Li, Q. Y.; Dasgupta, P. K.; Temkin, H.; Crawford, M. H.; Fischer, A. J.; Allerman, A. A.; Bogart, K. H. A.; Lee, S. R. *Applied Spectroscopy* **2004**, *58*, 1360-1363.

(42) Chen, S. J.; Chen, M. J.; Chang, H. T. *Journal of Chromatography A* **2003**, *1017*, 215-224.

(43) Manor, R.; Datta, A.; Ahmad, I.; Holtz, M.; Gangopadhyay, S.; Dallas, T. *IEEE Sensors Journal* **2003**, *3*, 687-692.

(44) Su, A. K.; Lin, C. H. *Journal of Chromatography B-Analytical Technologies in the Biomedical and Life Sciences* **2003**, *785*, 39-46.

(45) Tsai, C.-H.; Huang, H.-M.; Lin, C.-H. *Electrophoresis* **2003**, *24*, 3083-3088.

(46) Beale, S. C.; Sudmeier, S. J. *Analytical Chemistry* **1995**, *67*, 3367-3371.

(47) http://www.omegafilters.com/.

(48) Ullrich, B.; Schroeder, R. *Ieee Journal of Quantum Electronics* **2001**, *37*, 1363-1367.

(49) Mustafa, M. B.; Tipton, D.; Russo, P. S. *Macromolecules* **1989**, *22*, 1500-1504.

(50) Lucy, C. A.; Yeung, K. K. C.; Peng, X. J.; Chen, D. D. Y. *LC GC-Magazine of Separation Science* **1998**, *16*, 26-32.

(51) Sternberg, J. C. In *Advances in Chromatography*; Giddings, J. C., Keller, R. A., Eds.; Marcel Dekker: New York, 1966; Vol. 2.

CHAPTER FOUR. Low-Picomolar Limits of Detection Using High-Power Light-Emitting Diodes for Fluorescence[a]

4.1 Introduction

Light-emitting diodes (LEDs) have begun to see extensive use as light sources in fluorescence detectors. In relatively simple optical designs, LEDs have been used in liquid core waveguides,[1, 2] open beam format,[3-7] with optical fibers,[8] or a combination of open beams and optical fibers.[9-13] In more sophisticated instrumentation, new prototype LEDs operating in the mid-UV have been used with[14-16] and without[17] time discriminating detectors. While many of the aforementioned detectors have only studied model compounds, other reports show that LEDs can also be used in more interesting applications such as detecting DNA,[18] counting cells,[19, 20] Raman measurements,[21] anisotropy decay,[22, 23] and sensing environmental gases.[1, 24-32] In Chapter Three, the effect of spectrally filtering the LED light was studied.[4] This allowed for low-nM limits of detection, which are the lowest achieved with low-power LEDs.

One approach for increasing LED power is the use of larger LED chips. Standard LEDs are housed in a plastic dome of 3 or 5 mm and emit relatively low power. These 5 mm LEDs utilize a chip of ~250 μm × 250 μm, which can radiate up to 10 mW in the visible region. Newer, high-power packages by Luxeon contain an emitter which is 2

[a] A portion of this work has been published as E.P. de Jong and C.A. Lucy, "Low-picomolar limits of detection using high-power light-emitting diodes for fluorescence", *Analyst*, **2006**, *131*, 664 – 669. The epi-fluorescence work (Section 4.3.3.2) has not yet been published.

mm × 2mm, resulting in power output of 700 mW.[33] Standard and high-power LED packages are shown in Figure 4.1. The shape of the packaging used to house the high-power LEDs is designed to draw heat away from the chip, and does not include a back-reflecting bowl, such as is found in 5 mm LEDs. Consequently, the high-power LEDs have a divergence of 150°, compared to 10–60° when the reflecting bowl is present. Both the larger chip area and the greater beam divergence make it very challenging to focus the LED light onto a small spot, as is often desired in fluorescence detectors. High-power microscope objectives, although able to produce a smaller light spot, have a short working distance, often below 1 mm. When measuring fluorescence using a 90-degree configuration, it becomes necessary to have two objectives each within a millimetre of the capillary. Since there is no room to place two high-power objectives at an appropriate distance from the capillary, lower-power objectives must be used. Conversely, when using an epi-fluorescence configuration, the spatial constraints near the capillary are removed since only a single microscope objective is required. The same microscope objective delivers LED light and collects fluorescence. A high-power (63×), short working distance microscope objective allows the Luxeon LED to be focussed to approximately 150 μm, thus making use of significantly more light than was achieved using a 90-degree configuration.

This chapter presents the use of a 500 mW LED as a light source for fluorescence detection, using fused silica capillaries as the sample cell, or with the sheath flow detector. The effect of spatial filtering to block LED light scattered from the capillary wall is also investigated. A limit of detection in the low-picomolar range is obtained for on capillary detection. The new LED detector was adapted to receive the eluent of a gel

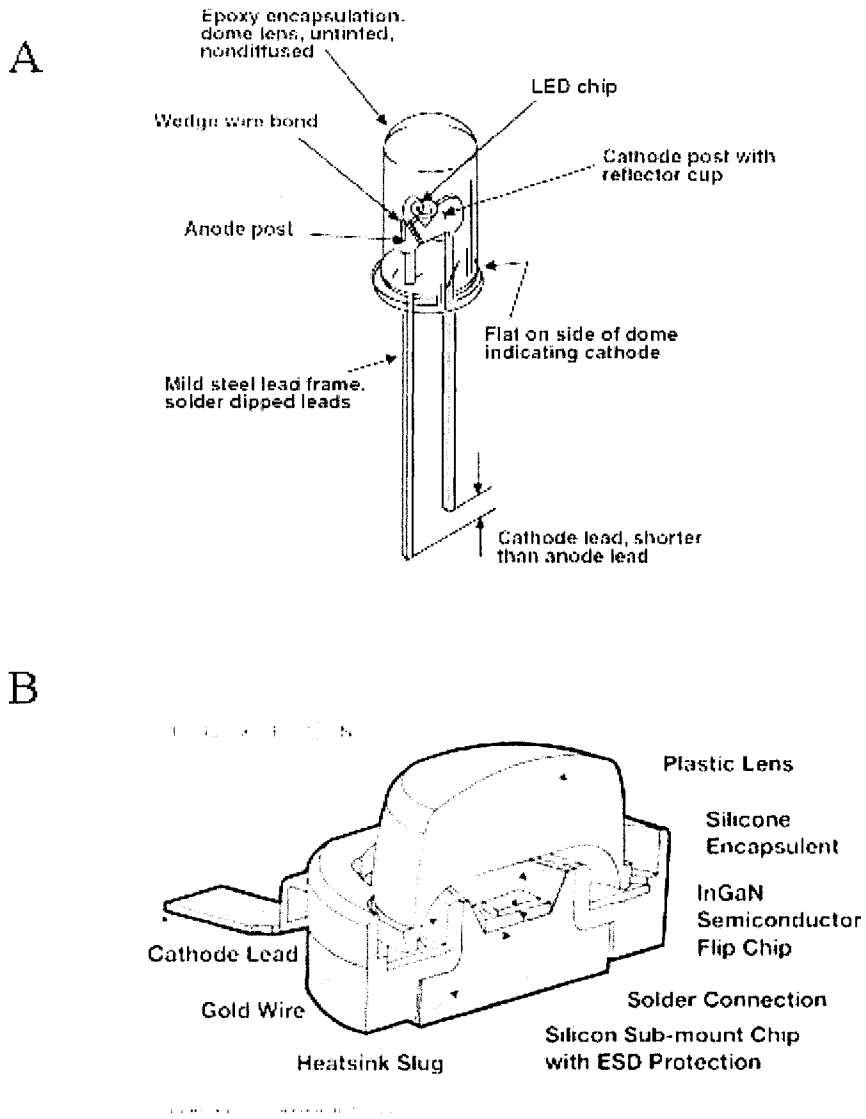

Figure 4.1 Structure of standard (a) and high-power (b) LEDs. Figure 4.1a courtesy of E. Fred Schubert, Department of Electrical, Computer & Systems Engineering and Department of Physics, Rensselaer Polytechnic Institute, Troy, NY. Figure 4.1b courtesy of Philips Lumileds Lighting Company.

filtration column. This extremely inexpensive light source does not sacrifice sensitivity and presents an attractive alternative to traditional light sources in fluorescence detection schemes.

4.2 Experimental

4.2.1 Chemicals

Fluorescein sodium salt, bovine serum albumin (BSA, ≥99%) and fluorescein isothiocyanate (isomer I, ≥90%) were from Sigma (St. Louis, MO, USA). Bottles of fluorescein stock solutions were covered with foil to prevent photodegradation. Boric acid (ACS grade; BDH, Poole, England), sodium dodecyl sulphate (SDS, 99%+ ACS reagent, Aldrich, Milwaukee, WI, USA) and sodium hydroxide (10 M solution; Fisher, Nepean, ON, Canada) were used as received. Ultrapure water was obtained from a Nanopure water system (Barnstead, Dubuque, IO, USA). Borate buffer was prepared by dissolving an appropriate amount of the conjugate acid in ultrapure water and adjusting the pH with 10 M NaOH while stirring.

4.2.2 Instrument

4.2.2.1 On-Capillary Measurements

4.2.2.1.1 Right-Angle Geometry

The instrument was a modification of one described in Section 3.2.2[4] the optical components of which are shown schematically in Figure 4.2. The coordinate system is

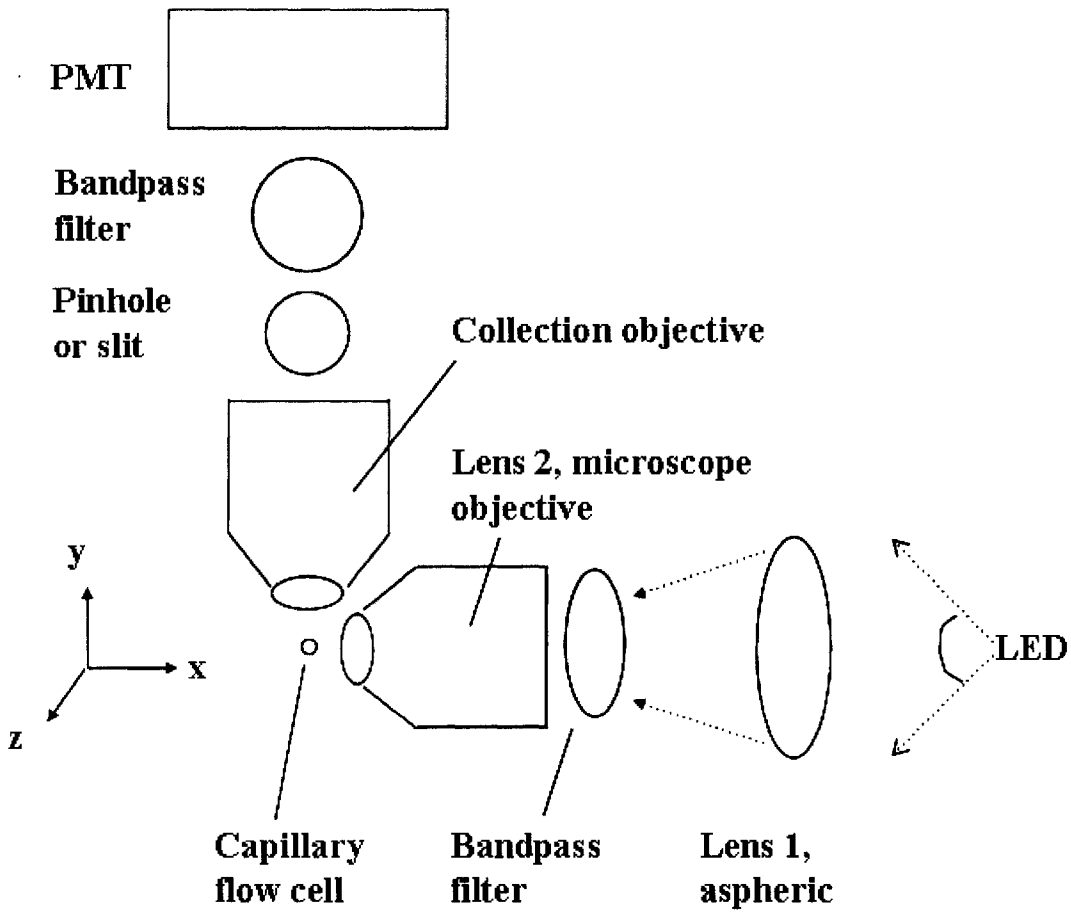

Figure 4.2 Schematic of the right-angle geometry fluorescence detector. The image is viewed down the capillary, that is, the *z*-axis. LED light is collimated by the ashperic lens and spectrally filtered by the first bandpass filter. A microscope objective focusses the light on the capillary, and a second objective collects fluorescence at right angles. Spatial filtering is performed by a pinhole or slit, and a second bandpass filter is used to spectrally filter the fluorescence. A PMT detects the fluorescence. Figure is not to scale.

better illustrated in Figure 4.3. Round or square fused silica capillaries (Polymicro Technologies, Phoenix, AZ, USA) were used as the sample cell. All capillaries were of 365 mm outer diameter (o.d.), with inner diameters ranging from 50 to 200 μm. Optical windows of ~4 mm length were created by burning off the polyimide outer coating. Pressure at the inlet end of capillaries was delivered by a Crystal CE system (model 300, ATI Unicam, Boston, MA, USA). A Luxeon V Star blue LED (LXHL-LB5C; Luxeon, San Jose, CA, USA), driven at 700 mA by a Xitanium power source (LED120A0700C24F; Advance Transformer Co., Rosemont, IL, USA), was used as the excitation source. The LED was mounted on an aluminum heat sink (500400B00000; Future Electronics, Pointe-Claire, QC, Canada), and held in position using an in-housebuilt stand. The LED power was determined with a LaserCheck hand-held laser power meter (Melles Griot, Nepean, ON, Canada). The LED light was collimated by an aspheric lens (01LAG111; Melles Griot), passed through a bandpass filter (XCY-485DF22; Omega Optical, Battleboro, VT, USA), and focused on the capillary by a 20× microscope objective (017791; Edmund Optics, Barrington, NJ, USA). The emitted fluorescence was captured at 90° by a 20× microscope objective (Edmund Optics), spatially filtered by a round or rectangular pinhole (built in-house), passed through a bandpass filter (XCY-535DF45; Omega Optical), and detected by a photomultiplier tube (R3896; Hamamatsu, Bridgewater, NJ, USA) driven at 600 V. The signal from the photomultiplier tube was collected by a data acquisition board at 5 Hz (National Instruments, Austin, TX), displayed by Virtual Bench Logger software (Version 2.51; National Instruments) and stored on a Celeron 400 MHz PC. Data was plotted and

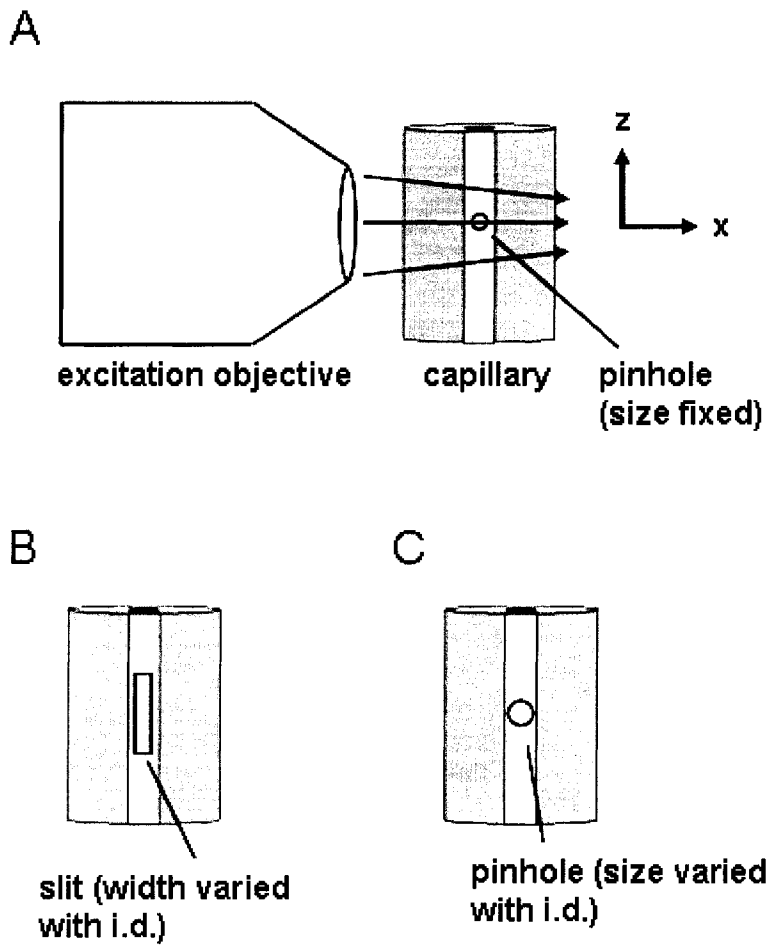

Figure 4.3 Geometry of the right-angle fluorescnece detector, viewed along the detection (y) axis. This orientation represents the view of the capillary from the PMT, with the pinhole or slit superimposed in front of the capillary. The different pinhole options shown here were explored in Section 4.3.3.1.

analyzed using Igor Pro Version 3.12 (WaveMetrics, Lake Oswego, OR, USA). The entire system was housed in a dark room.

4.2.2.1.2 Epi-Fluorescence Geometry

The high-power LED was also used in an epi-fluorescence configuration, where the excitation and emission light follow the same path (Figure 4.4). A few adaptations from the right-angle geometry are required. First, the LED light is collimated by an achromatic lens (01LAO014; Melles Griot), passed through a bandpass filter (XCY-485DF22), then reflected by a dichroic filter (505DCLP; Chroma Technology Corp., Rockingham, VT, USA) towards a 40× or 63× microscope objective (04OAS016; 63× discontinued; Melles Griot). The emitted fluorescence was captured by the same objective, passed through the dichroic filter, spatially filtered by a 2.0 (with 40× objective) or 3.0 mm pinhole (with 63× objective; pinholes built in-house), passed through a bandpass filter (XCY-535DF45), and detected by a photomultiplier tube (as above) driven at 550 – 600 V. An extensive series of baffles was constructed inside the detector box to eliminate stray light reaching the detector.

4.2.2.2 Sheath Flow (Post-Capillary) Measurements

A sheath flow cuvette holder was made in-house by Dieter Starke of the Department of Chemistry Machine Shop. The sheath flow detector for CE was pioneered by Dovichi and co-workers[34, 35] at the University of Alberta, and his later designs served as the model for the components fabricated for this work. The cuvette and its holder are

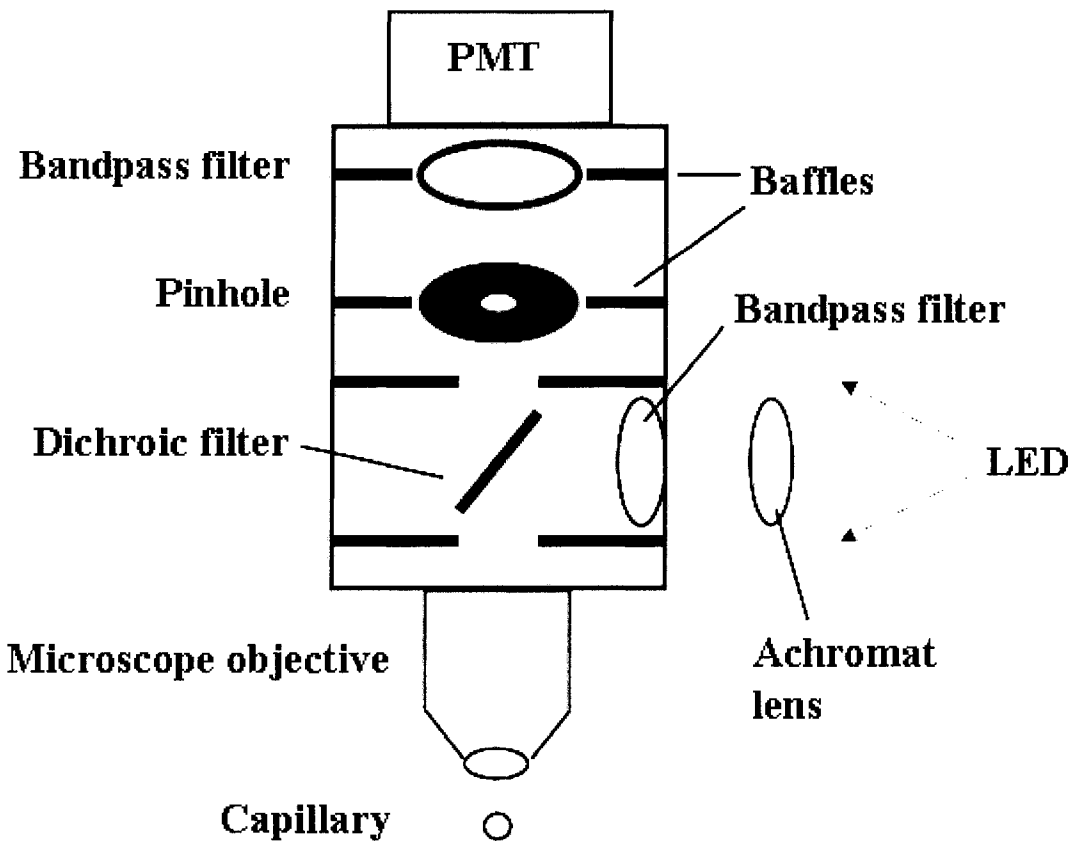

Figure 4.4 Schematic of the epi-fluorescence detection geometry. LED light passes through a lens and a bandpass filter, is reflected by a dichroic filter and focussed by the microscope objective. Fluorescence signal is collected by the microscope objective, transmitted by the dichroic filter, spatially filtered by a pinhole, spectrally filtered by a bandpasss filter and detected by the PMT. Figure is not to scale.

shown schematically in Figure 4.5. The cuvette holder consisted of a stainless steel cylinder with slits on four perpendicular sides, which accommodated the quartz cuvette. Note that overtightening the upper portions of the sheath flow cuvette has been known to crack the cuvette; an expensive mistake to make. The capillary was inserted into the upper "T", which had two arms for flow of sheath fluid. A graphite ferrule prevented solution from flowing out through the top. Plastic tubing was attached to the two arms of the "T", as well as the outlet (bottom). Sheath fluid from a 500 mL wash bottle was flowed by gravity through one arm of the "T". When applying pressure to the inlet stream, the vast majority of sheath fluid flowed out through the other arm of the "T", which serves to remove air bubbles trapped in the tubing between the wash bottle and the cuvette holder. The outlet of this second arm was then blocked by clamping the plastic tubing. Application of further pressure on the wash bottle flushed out remaining bubbles in the cuvette. The cuvette was custom-ordered from Hellma (Concord, ON), and is made from Suprasil Quartz. The rectangular cuvette had a length of 20 mm, and a width of 2 mm. The cuvette had a square center channel running along its long axis with 0.2 mm sides. A fused silica capillary (Polymicro) of 50 / 150 μm i.d./o.d. was partially inserted into the cuvette, allowing for sheath fluid to enter along the exterior of the capillary. The sheath fluid was identical to the background electrolyte. The fluid level in the reservoir was usually 5 – 20 cm above that of the waste container. A short (<2 mm) section of polyimide coating was removed from the capillary, since the coating causes scatter and is, itself, fluorescent. The excitation beam was directed approximately 0.2 mm below the end of the capillary. The optics used for sheath flow detection differed markedly from the final arrangement used in on-capillary measurements. Since the

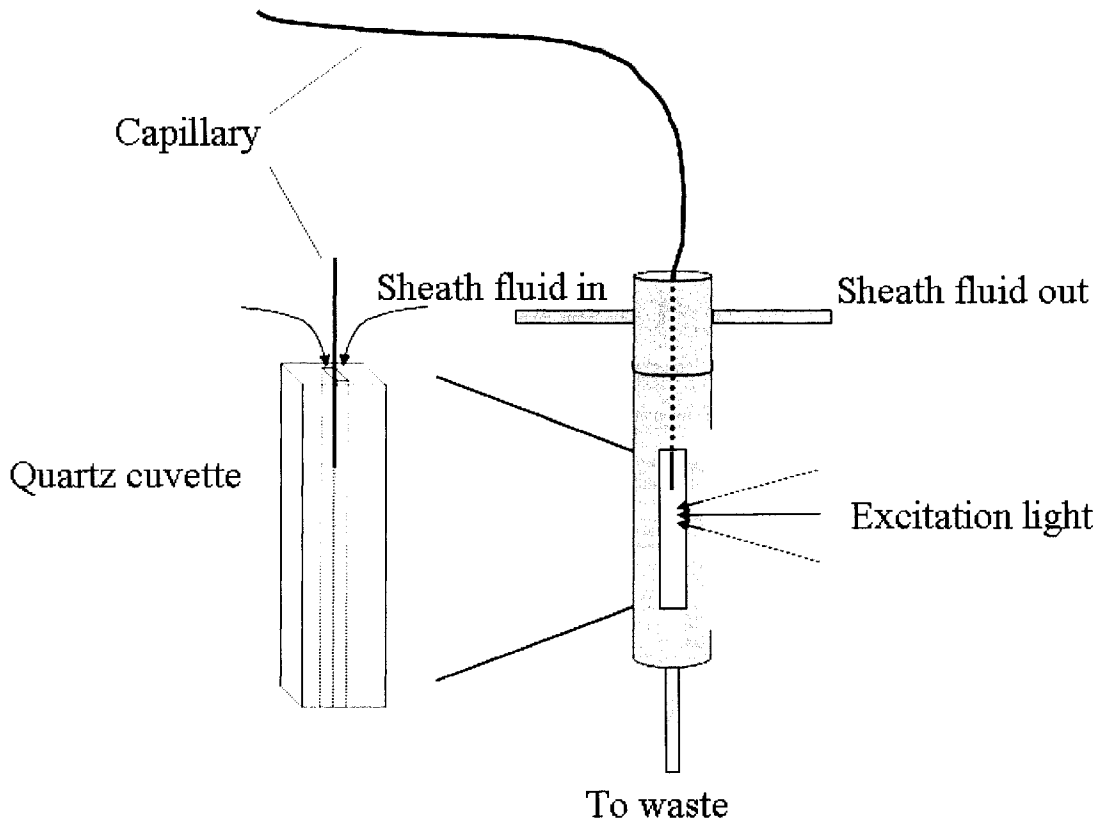

Figure 4.5 Schematic of the sheath flow detector. Right: the cuvette nested in a stainless steel the holder which also directs the sheath fluid through the cuvette. Left: magnification of the quartz cuvette with the capillary and sheath fluid entering from the top.

sheath flow detector was found to be very sensitive to an excessively large excitation beam, Equation 4.1 (Section 4.3.2) was critical in guiding the selection of optics. Light collection efficiency was sacrificed in order to obtain a small beam waist. The LED was placed ~30 cm from a 50 mm diameter plano-convex lens with 150 mm focal length. On the opposite side of the lens, at a distance of ~20 cm, a bandpass filter (centered at 490 nm, 10 nm bandwidth, Omega Optical) was mounted. Five centimetres beyond the bandpass filter, a 1000 μm pinhole (Melles Griot) was mounted against a 20× objective (Edmund Optics). A second 20× objective (Edmund Optics) collected the fluorescence perpendicular to the excitation beam. The fluorescence was passed towards the PMT through a 1000 μm pinhole and a bandpass filter centered at 520 nm with 20 nm bandwidth (Beckman, Fullerton, CA). The Crystal CE system was found to be incompatible with 150 μm o.d. capillaries and required the fabrication of a 15 cm sheath at the inlet end. The sheath consisted of 185 / 365 μm (i.d. / o.d.) capillary, held in place with Holdtite ST3500 UV-curable glue. The two capillaries were sealed together with excess glue under a UV lamp typically used for visualizing TLC plates, using its long-wavelength mode.

4.2.3 Protein Derivatization

Stock solutions of 1 mM fluorescein isothiocyanate (FITC) in acetone and 100 μM bovine serum albumin (BSA) in 0.1 M $NaHCO_3$ buffer were stored at 4°C. BSA labelling was performed at ambient temperature in a solution of 2.5 μM BSA, 400 μM FITC in 0.1 M $NaHCO_3$ with 40% v/v acetone. This solution was gently shaken for one

hour. Samples for analysis were further diluted using 25 mM sodium borate buffer at pH 9.5.

4.2.4 Gel Filtration

Sephadex® G-25 (Fine, Aldrich) particles were allowed to swell in the mobile phase overnight while stirring. This slurry was loaded into a glass column of 15 mL internal volume (8 × 0.8 cm) and allowed to pack by gravity. Injection volumes up to 200 μL did not cause broadening of the analyte bands. After loading the sample with a pipette, 0.22 $mL \cdot min^{-1}$ mobile phase was introduced into the column by a peristaltic pump (Gilson Minipump 2, Middleton, WI, USA). The column effluent was directed into a 10 cm length of fused silica capillary (200 μm i.d., 360 μm o.d., Polymicro) through a conical fitting prepared from a 100 μL pipette tip (Fisher, Nepean, ON). The capillary was held in the pipette tip by carefully melting and deforming the pipette tip around the capillary. An optical window was then created on the capillary 5 cm from the gel filtration column outlet by burning off a section of the polyimide coating. The capillary was placed in the beam path and thus served as the sample cell. A mobile phase of 15 mM sodium borate (pH 9.5) with 5 mM SDS was used. The sub-micellar concentration of SDS partially unfolded the BSA, thus preventing adjacent fluorescein labels from stacking and quenching.[36]

4.2.5 Methods

Continuous flow measurements were performed by pumping water or a fluorescein standard through the capillary for approximately 60 s each. A moving boxcar averaging of 50 points was applied to all data. LODs were calculated using the United States Environmental Protection Agency (EPA) protocol.[37] Briefly, a calibration curve was generated encompassing the entire dynamic range of the detector. The average signal was obtained from seven replicate, blank-corrected measurements of a sample whose concentration gives a signal-to-noise ratio of 5–10. The LOD was calculated using the definition LOD = $t \times s$, where t is the value of student's t at $n - 1$ degrees of freedom and 99% confidence for a one-tailed test, and s is the standard deviation of the seven replicate measurements.

4.3 Results and Discussion

4.3.1 Properties of the High-Power LED

While a number of companies manufacture high-power LEDs, the market is currently dominated by Cree Inc., Lumileds Lighting LLC, Nichia Corp., Osram Opto Semiconductors and Toyoda Gosei Co. Ltd.[38] In this work 500 mW Luxeon high-power LEDs, also known as Lumileds, were used. Luxeon now produces LEDs that emit 700 mW of radiation.[33] Currently, the colour selection of these LEDs is limited to just four colours with peak wavelengths ranging from 455 to 525 nm. In the present study, an LED with a peak wavelength of (nominally) 470 nm with a bandwidth of 25 nm was used. As demonstrated in Section 3.3.2,[4] the use of a bandpass filter between the LED

and the detector cell is critical. While LEDs have a relatively narrow bandwidth of ~30 nm, they emit weakly at longer wavelengths, and this light can be scattered towards the detector. Elimination of this longer wavelength emission reduces the background signal by at least a factor of 70. To this end, a bandpass filter centered at 485 nm with 22 nm half-width was placed between the LED and the sample cell.

4.3.2 Exploiting the LED's High Power

As mentioned in Section 4.1, LEDs are often coupled directly to a fiber optic cable in fluorescence detectors, perhaps as a result of the telecommunications industry's success in utilizing LEDs this way. Two possible benefits of this approach are the potential for high coupling efficiency of light into the fiber, and the separation of a highly divergent light source from the detector area. A disadvantage is that a fiber optical setup, once selected, may contain a number of permanently fixed components (epoxied lenses associated with either the LED or the fiber) which forbids future refinements or improvements. For this reason, an open-beam configuration was expored in this chapter.

When performing fluorescence for biological applications, a flow cell is often used where the light must be focused to give a beam waist of ~2 mm. One exception to this nearly universal size is the 160 × 250 μm flow cell used in the BD FACSAria™ flow cytometer. Focusing the light from high-power LEDs to such a small spot is very challenging for two reasons. First, the high-power LEDs are much more divergent than standard LEDs. The beam from a Luxeon LED has a divergence of 150°, whereas low-power, 5 mm LEDs can be purchased with divergences ranging from 10–60°. The larger divergence of the high-power LEDs is due to the shape of their epoxy dome lens.

Second, the emitting surface of high-power LEDs is much larger than that of standard LEDs. Luxeon LEDs use an emitting area of 2 mm × 2mm, compared to the ~250 μm × 250 μm of standard LEDs. This larger emitting area requires a greater reduction of this spot size at the focal point. Consequently, it becomes challenging to direct a maximum amount of LED light into a small sample area. The compromise between light collection and obtaining a small spot size is a classical problem in optics. This is illustrated by rearranging the combined lens equations[39] to obtain:

$$m = f_1 \div f_2 \tag{4.1}$$

where m is the magnification of the image, f_1 is the focal length of the lens nearest the light source (condenser lens) and f_2 is the focal length of the lens used to focus this light onto the target. Lens 2 is usually a microscope objective with a short (1–20 mm) focal length and a clear aperture[b] of ~5 mm. Thus lens 1 must have a clear aperture in the range of 5 mm so as to create a collimated beam which will be accepted by the microscope objective (lens 2). In addition, equation 4.1 demands that lens 1 has a relatively long focal length ($f_1 \simeq 10 f_2$) to obtain a magnification less than unity. Such a lens however, will exhibit extremely poor light collection due to its low numerical aperture (NA) and is not readily available. Instead, we have used an aspheric lens with NA = 0.75, giving it very high collection efficiency. This is the greatest NA lens available short of using an immersion microscope objective. Due to the spatial constraints near the capillary flow cell and the desire to employ simple, commercially-available optics, the beam waist was reduced to approximately 2 mm. Thus a significant portion of the LED light is not directed at the sample cell. Nonetheless, the increased

[b] Also known as free aperture or objective aperture. The opening in the mount of an optical system or its components that restricts the extent of the bundle of rays incident on the given surface. It is usually circular and specified by its diameter. http://www.photonics.com/dictHome.aspx

power of the new LEDs is still sufficient to yield a 30-fold improvement in LOD compared to low-power LEDs. Using 50 μm i.d. capillary tubing and CE analysis, the LOD using a low-power LED was 3 nM (Section 3.3.6), compared to 90 pM using the high-power LED (Figure 4.6). The dynamic range with the high-power LED was from 0.3 – 30 nM.

4.3.3 Detector Cell

4.3.3.1 Capillary Dimensions for On-Column, Right-Angle Measurements

To make full use of the large spot size generated by the high power LEDs, large diameter capillary tubing is used to maximize the volume of sample illuminated. Figure 4.3 illustrates how increasing the diameter of capillary tubing (*x*- and *y*- dimensions of the detector cell) allows for greater light capture. Note that the entire *y*-axis is always captured by the detector. By maintaining a constant pinhole size in the light capture optics, only one-dimensional gains in fluorescence are captured, along the *y*-axis (Figure 4.3A). Thus, increasing the capillary i.d. resulted in linear gains in sensitivity. This relationship was verified using continuous flow experiments. The pinhole was held constant at 1000 μm, which is appropriate for a 50 μm capillary when imaged by a 20× microscope objective. Round capillary internal diameters of 50, 75, 100, 150 and 200 μm were studied, and a plot of sensitivity vs. inner diameter was linear with $r^2 = 0.987$ (Appendix 11). Square capillaries were also studied but these were difficult to align, thus giving more scatter background signal. Consequently, all data presented here employs round capillary tubing. To solidify our understanding of spatial filtering effects, the

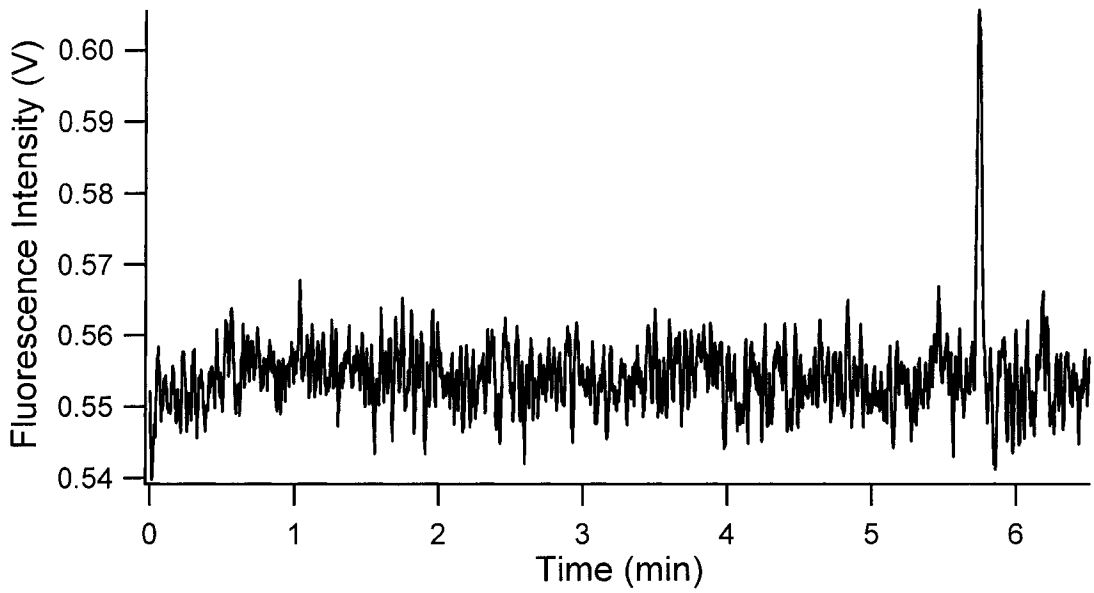

Figure 4.6 Electropherogram of 300 pM fluorescein. The right angle, on-capillary detection geometry is employed here. Sample was injected at 25 mbar for 3 s; applied voltage was 25 kV; background electrolyte was 25 mM sodium borate at pH 9.5. The data has been smoothed using 2nd order Savitzky-Golay smoothing on 21 points.

pinhole was modified to increase light capture along two axes. Instead of using a circular pinhole, a series of vertical slits were fabricated. The length of all slits was constant at 4 mm, which allowed for capture of 200 μm along the capillary (*z*-) axis, while the slit width was altered proportionally to the capillary i.d. Referring to Figure 4.3B, increasing the capillary i.d. increases its *x*- and *y*-dimensions, and both of these increases are captured by the slit. Using the rectangular slits, the relationship between sensitivity and capillary inner diameter followed the expected quadratic relationship, shown in Figure 4.7. Finally, circular pinholes with diameters proportional to the capillary i.d. were employed. Referring to Figure 4.3C, increasing the capillary i.d. increases its *x*- and *y*-dimensions. Increasing the pinhole diameter increases light capture along the *x*- and *z*-axes, while the entire *y*-axis is always captured, regardless of the shape of the pinhole. As expected, a cubic relationship between sensitivity and capillary inner diameter resulted, with $r^2 = 0.998$, seen in Figure 4.8. This shows that dramatically better sensitivity can be achieved by even a slight increase in the capillary i.d., provided that the pinhole shape and size are adjusted accordingly.

4.3.3.2 Epi-Fluorescence Measurements

Adapting the detector box from the right angle geometry to epi-fluorescence required machining of a hole in the side of the box. The highly divergent LED light enters the box through this hole, creating the potential for severe stray light effects. Indeed it was observed that the PMT voltage could not be increased above 400 V without saturating the detector. The addition of a series of baffles greatly reduced this stray light, with a water-filled capillary giving a signal of ~2 V with the PMT biased at 600 V.

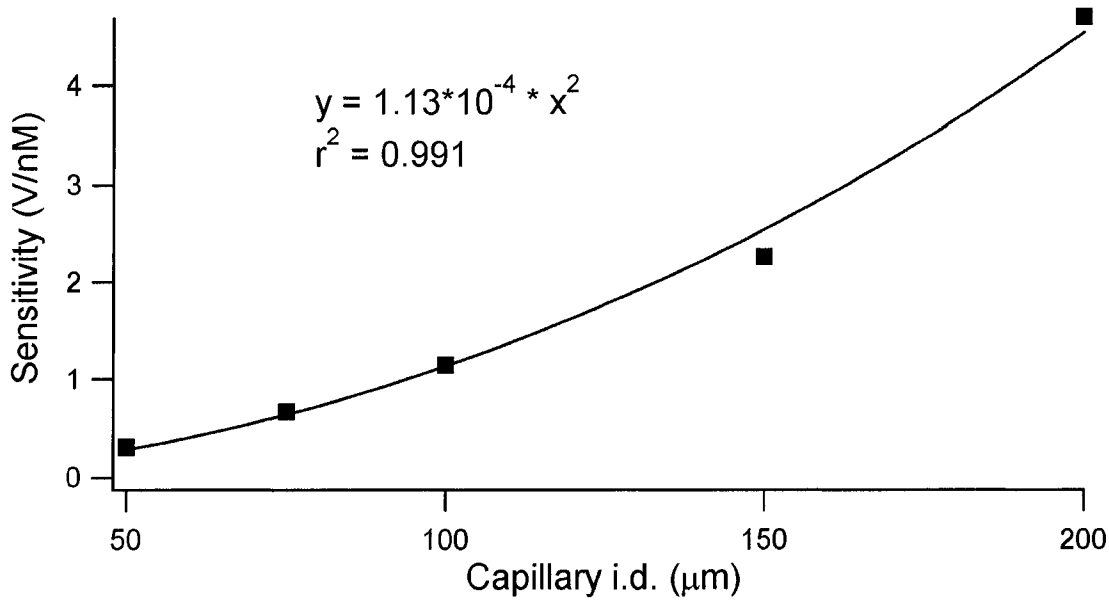

Figure 4.7 Relationship between capillary inner diameter and detector sensitivity. The capillary is imaged through a series of slits with a constant length, but whose width varies with capillary inner diameter. Data was fit using nonlinear regression.

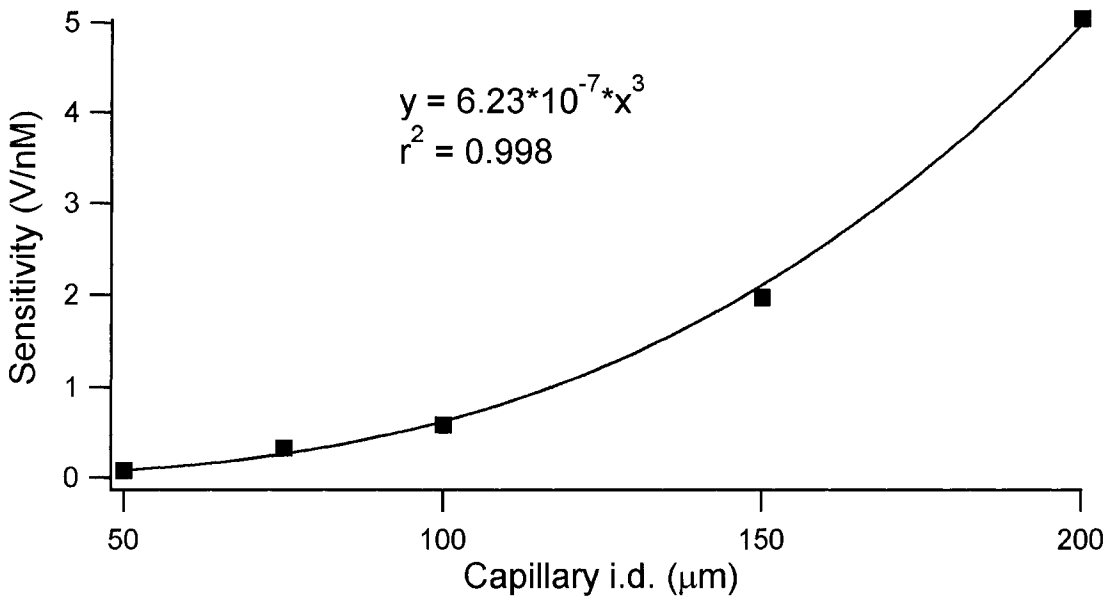

Figure 4.8 Relationship between capillary inner diameter and detector sensitivity. The capillary is imaged through a series of round pinholes whose diameter varies with capillary inner diameter. Data was fit using nonlinear regression.

The selection of microscope objective in epi-fluorescence work can affect the light spot size because a higher power objective can reduce light to a smaller spot. This can help to reduce detector bandbroadening. However, high power objectives also tend to have a smaller effective diameter, thus accepting a smaller excitation beam. In this case where LED light can not be perfectly collimated, the small acceptance area of the objective will result in decreased light transmission. Table 4.1 outlines the different options in choosing an objective. The LaserCheck meter used to measure the power of the LED here is designed for collimated light input which is not achieved with an LED. Consequently, the values reported here display a trend, but the absolute values can not be trusted.

As mentioned in Sections 3.3.1 and 3.3.7, the use of a 20 × objective for right-angle measurements causes detector bandbroadening. Detector bandbroadening was studied for the epi-fluorescence configuration using 75 μm i.d. capillary and a 40× objective. Progressively smaller sample injections were made until a plateau in efficiency was observed. At this point, it was assumed that injector bandbroadening had been mitigated, leaving only detector bandbroadening and longitudinal diffusion as sources of extracolumn bandbroadening. The results are shown in Figure 4.9. As can be seen, smaller injections significantly increase the efficiency, to approximately 200,000 plates (approximately 300,000 plates/m). There is a small decrease in peak height as a result of decreasing injection size which, in most cases, can be tolerated. Using the 63× objective further reduced the spot size and thus increased efficiency, as seen in Figure 4.10. In this case, increasing injection size had a detrimental effect of efficiency, but a beneficial effect on peak height. It is necessary then, to choose between efficiency and

Table 4.1 Spot size and light power delivered by various microscope objectives.

Microscope objective power	Spot size (mm)	Power at 485 nm (μW)
6.3×	1.2	304
10×	1.0	297
20×	0.5	179
40×	0.3	85
63×	0.2	25.6

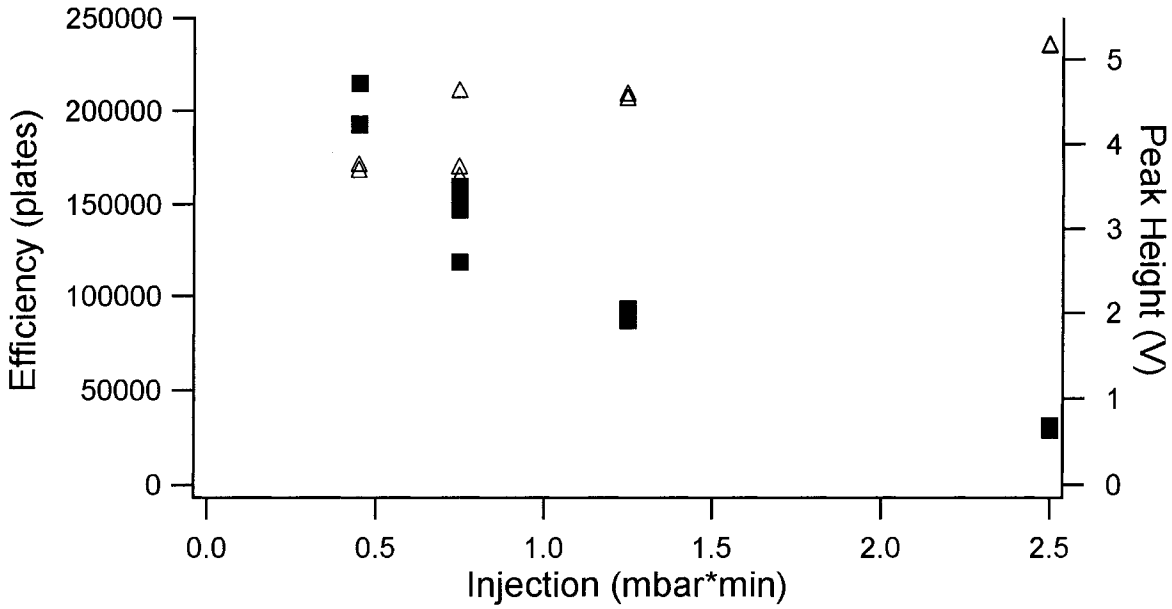

Figure 4.9 Effect of injection size on efficiency and peak height. Epi-fluorescence geometry is used here with a 40× objective. Sample was 10 nM fluorescein, injected at 25 mbar for 3 s. Electrophoresis was performed with 25 mM soldium borate BGE at 25 kV. Closed squares (■) indicate efficiency and open triangles (△) indicate peak heights.

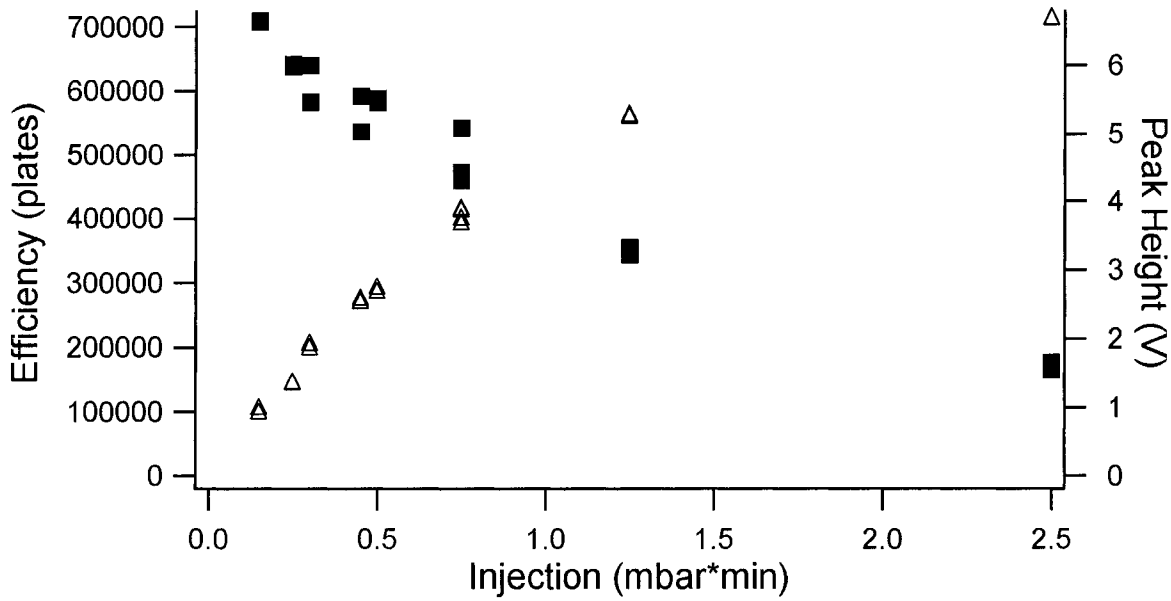

Figure 4.10 Effect of injection size on efficiency and peak height. Epi-fluorescence geometry is used here with a 63× objective. Sample was 10 nM fluorescein, injected at 25 mbar for 3 s. Electrophoresis was performed with 25 mM soldium borate BGE at 25 kV. Closed squares (■) indicate efficiency and open triangles (△)indicate peak heights.

sensitivity when using the epi-fluorescence configuration with the 63× objective. Efficiencies reached 700,000 plates (10^6 plates/m). While no plateau in efficiency was observed in this study, the lowest injection pressure and time used are near the limits of what the instrument can be expected to reliably deliver (5 mbar for 1.8 s). Thus it is likely that injector bandbroadening has been nearly eliminated. Fortunately, the observed efficiency of 700,000 plates approaches the theoretical limit of 1,100,000 plates for this separation.

Limits of detection were also improved when using the epi-fluorescence detector. Table 4.2 lists the LODs by continuous flow analysis, dynamic range, instrument sensitivity and efficiency for each of the detection geometries described in this chapter. It is clear from Table 4.2 that the epi-fluorescence geometry with the 63× objective gives the best combination of limits of detection with efficiency. This performance is attributed to the small light spot size obtained by the 63× objective. As mentioned above, the efficiency of this detector configuration is only 36% below the theoretical upper limit. Also, the limit of detection is competitive even with that obtained in a larger flow cell, discussed in Section 4.3.4.

4.3.3.3 Sheath Flow Measurements

Another method of reducing scatter background is to use a post-capillary, sheath flow detector. Round capillary walls, such as used above, scatter the excitation light which, in spite of filtering, contains some light at the detection wavelengths. As well, the capillary is weakly fluorescent due to impurities in the silica.[40, 41] The sheath flow cuvette was designed to eliminate these problems. The cuvette consists of a rectangular

Table 4.2 Sensitivity and efficiency in the different detection configurations studied here. All measurements except for sheath flow made in 75 μm i.d. capillary. The analyte was fluorescein.

Geometry	LOD (pM)[a]	DR (nM)[a]	S (V/nM)[a]	N (plates)[b]
Right angle	52	0.1 – 30	0.24	400,000
Epi with 40x	18	0.01 – 3	0.84	200,000
Epi with 63x	6	0.01 – 10	0.66	700,000
Sheath[c]	ND	ND	ND	800,000

[a] Measured by continuous flow.

[b] Measured by capillary electrophoresis.

[c] Measured in 50 μm capillary. All others in 75μm capillary.

DR = dynamic range

ND = not determined by continuous flow

flow cell with a square inner channel. Since the excitation and captured emission light are perpendicular, the flow cell is designed to present both these light beams a perpendicular, optical-grade surface. Both a sample and sheath fluid pass through the cuvette. Low-pressure flow in the laminar flow regime creates minimal mixing between the two streams. The sheath fluid is introduced at a greater flow rate than the sample stream, leading to a narrowing of the sample stream. The sheath fluid is identical to the background electrolyte, ensuring that the sample and sheath fluid streams have the same refractive index. Detection is spatially filtered to exclude any residual scattering near the cuvette walls, thus detecting only the sample portion of the overall fluid stream. Consequently, the only source of scattered excitation light is the Rayleigh and Raman scattering performed by the solvent. When using an ideal light source such as a laser it is unnecessary to use a bandpass filter for the excitation light due to the minimal scatter in the sheath flow detector. It is not clear whether one can omit the use of a excitation bandpass filter when using an LED for excitation. Avoiding the excitation filter would allow the full spectrum of the LED to excite the sample, providing greater excitation efficiency. Figure 4.11 shows the effect of omitting the excitation filter on an electropherogram of 30 nM fluorescein. There are a number of differences between the experiments with and without the excitation filter, summarized in Table 4.3. The addition of an excitation filter lowers the background signal. In order to properly compare the experiments with an excitation filter against those without, the PMT voltage should be adjusted until the background signal for the two experiments are equal. Use of the excitation filter results in better sensitivity, in spite of the use of less excitation light. Yet even with better sensitivity and a quieter baseline, the limits of detection are

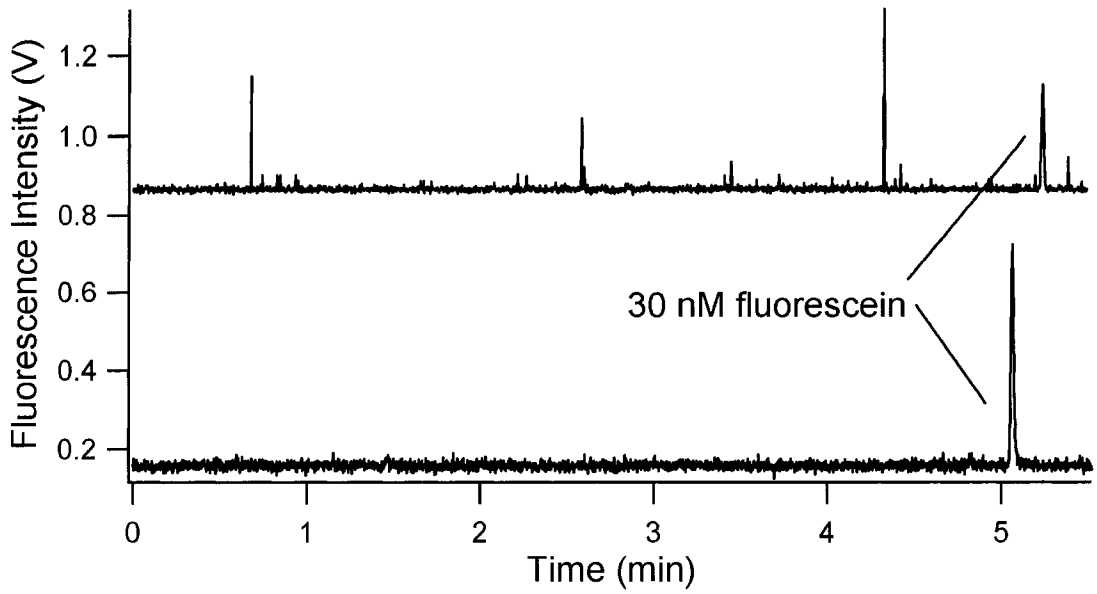

Figure 4.11 Electropherograms of 30 nM fluorescein, illustrating the effect of a bandpass filter in the excitation beam. These data were obtained with (lower trace) and without (upper trace) an excitation bandpass filter. Both traces have essentially the same background signal, but the upper trace is offset for clarity. Experimental conditions are given in Table 4.3 and Section 4.2.2.2.

Table 4.3 Comparison of experimental conditions in Figure 4.10, and their effect on the figures of merit for each method.

	Unfiltered	**Filtered**
PMT voltage (V)	600	650
Background signal (V)	0.16	0.17
Sensitivity (V/μM)	7.09	19.5
LOD (nM)	0.8	1.7

essentially equal, at ~ 1 nM (Table 4.3). False peaks in the upper trace of Figure 4.11 are identified by their narrow width. If these spikes are treated as peaks, their efficiency is approximately 11,000,000 plates, or ten times the theoretical maximum efficiency for fluorescein. Clearly these spikes do not result from analyte molecules. Instead, the numerous false peaks are attributed to particulate matter or air bubbles from the sheath fluid passing through the point of detection. These cause scatter events which can either obscure or artificially enhance true signal peaks. Eventually, the optics and the spectral filtering for on-column measurements were improved (Section 4.3.3.2), giving better limits of detection than in the sheath flow configuration. Also, on-column measurements require significantly less operator skill for optical alignment and achieving a stable sheath flow, and thus are much more robust compared to sheath flow detection. As well, sheath flow detection is more sensitive to an excessively large excitation beam. The optics, including a pinhole filter in the excitation beam, must be adjusted to produce a small beam waist at the cost of LED light collection efficiency. This further supports the use of on-column measurements, which were used for the remainder of the experiments described here.

It was also envisioned that the sheath flow detector could be used to reduce detector bandbroadening. Although suffering from a large illuminated area, using a high sheath flow rate would accelerate analyte molecules through the detector, reducing peak width. It has been shown that a high sheath flow rate will have only a small detrimental effect on a CE separation due to pressure-induced laminar flow opposite the direction of the eof.[42] While good efficiencies were observed in the sheath flow cuvette (Table 4.2), little dependence of efficiency on sheath flow rate was found (Figure 4.12).

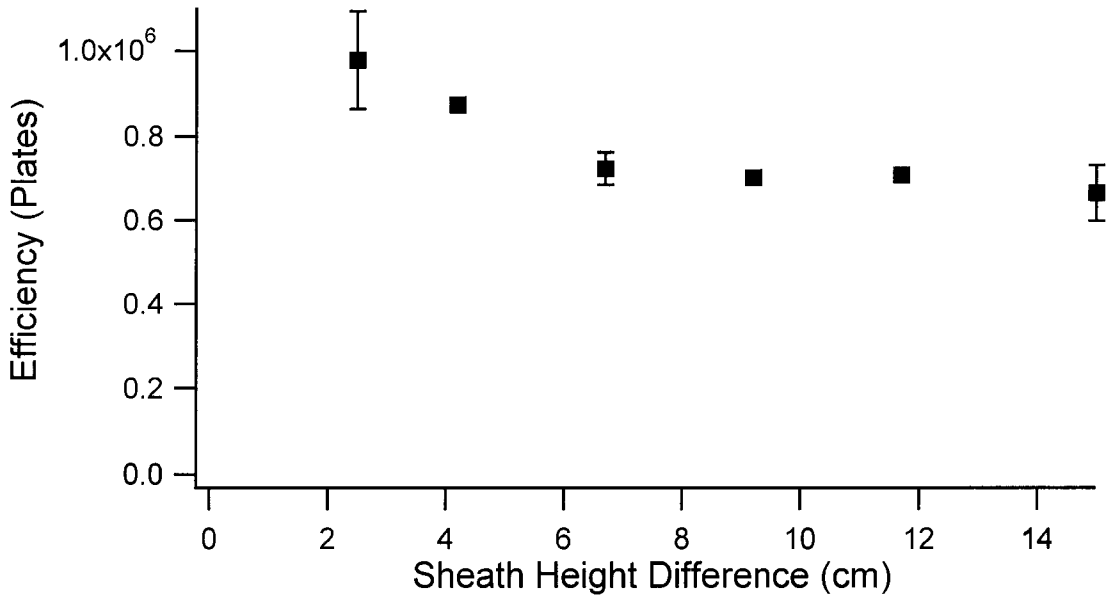

Figure 4.12 Effect of sheath flow rate on peak efficiency in the sheath flow cuvette. The sheath height difference is proportional to the flow rate. Sample of 1 μM fluorescein was injected at 10 mbar for 1.2 s. Electrophoresis was performed with 25 mM soldium borate BGE at 25 kV. Error bars represent one standard deviation for two trials.

4.3.4 Pinhole Size

It is not immediately obvious which size of pinhole is optimal for sensitivity and LOD. When selecting a pinhole which images less than the entire capillary inner diameter, the background signal is reduced by spatially filtering the light scattered by the round capillary walls (Figure 3A *vs.* 3C). However, this also results in reduced sensitivity, proportional to (pinhole diameter)^2, as shown in Figure 4.13. Increasing the pinhole size such that the imaged spot is greater than the capillary i.d. increases sensitivity proportional to the pinhole size (Appendix 12), but the background signal becomes so large that the dynamic range of the detector becomes limited to two orders of magnitude. Consequently an optimum limit of detection is obtained when using a pinhole which images 90% of the capillary i.d. It should be noted however, that a low-frequency noise in the background signal caused significant fluctuation in the calculated limits of detection (46% RSD for 5 trials). The source of this low frequency noise (period ~20 s) is unknown, but is evident in Figure 4.14 between 50 and 80 s. The limit of detection under the optimized conditions (200 μm i.d. capillary, 3.5 mm pinhole) is 3 pM, as shown in Figure 4.14. Further improvements in LOD should be possible if the scatter background signal can be reduced, possibly with the help of a short-pass spectral filter (see Section 6.2.1). An LOD of 3 pM is far superior to the 3 nM LOD obtained in our previous low-power LED work[4] and the 1 nM LOD from use of a 150 mW high-power LED.[5] Further, this sensitivity approaches the 0.58 pM LOD obtained using a laser-based flow detector[43] and demonstrates that LEDs, used properly, can rival laser-based detectors. Indeed, some LIF detectors are capable of concentration limits of detection of 81 fM when coupled with time-discriminaton[44] and 15 aM when examining

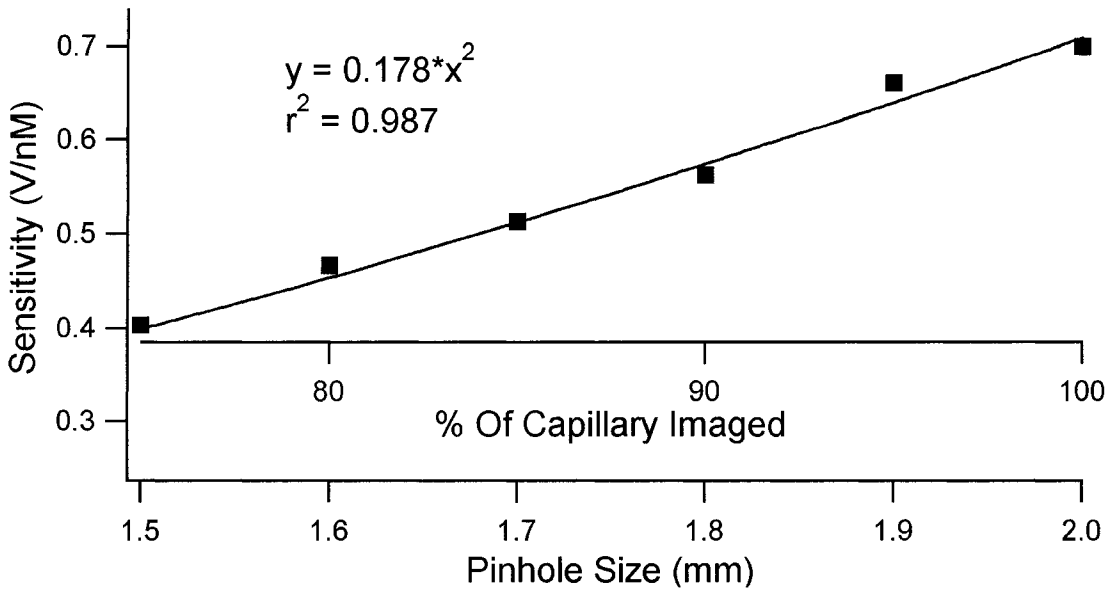

Figure 4.13 Relationship between using a smaller pinhole and sensitivity, on a 100 µm i.d. capillary. Calibration curves were constructed for each pinhole size to determine the sensitivity. The data is fit using nonlinear least-squares.

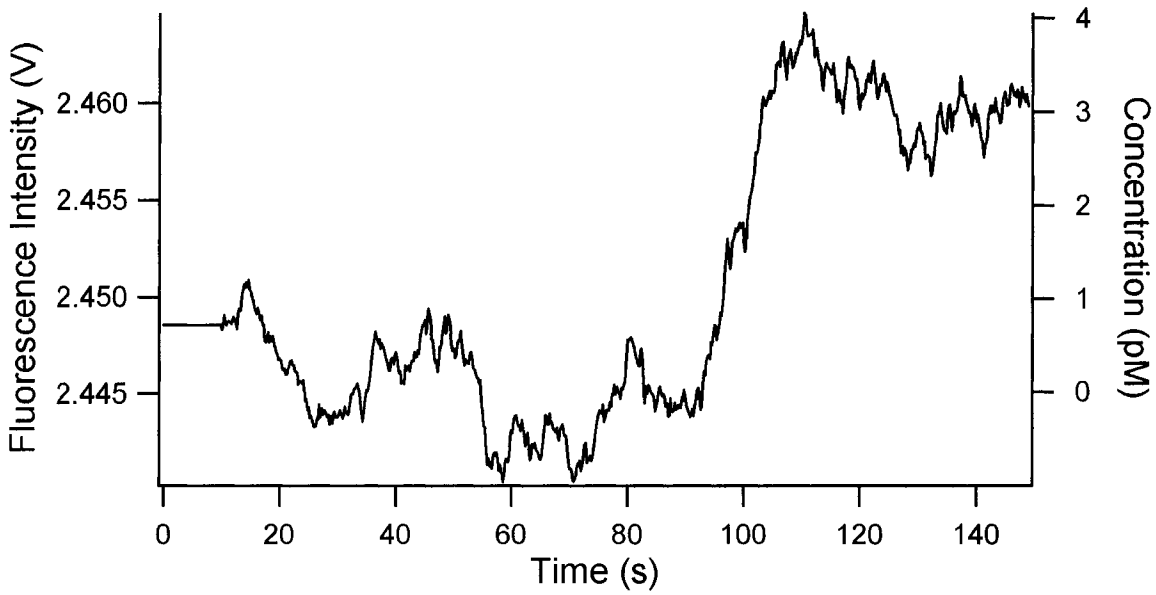

Figure 4.14 Signal trace of a continuous flow experiment using 3 pM fluorescein. At ~100 s, a step change indicates the transition from water to fluorescein. The data was smoothed using 50 point boxcar averaging.

the fluorescent product of an enzyme reaction.[45] However, we compare our results here to comparable instruments where the primary difference is the replacement of the laser by an LED. The continuous flow experiments used here have the potential to achieve lower LODs than in experiments where stationary solutions are measured. This lowering of LOD is due to the rapid replacement of any photobleached analyte in the detection window. In this work, some photobleaching is seen under stopped flow conditions (data not show). However, no photobleaching for fluorescein was observed at a spectral irradiance of 40 $W \cdot cm^{-2}$ for up to 3 s exposure,[46] whereas our experiments used <12.5 $W \cdot cm^{-2}$ under flow conditions. Furthermore, we have analyzed fluorescein by capillary electrophoresis over a wide range of flow rates and saw no evidence of photobleaching (Appendix 13). Thus it seems appropriate to compare the LODs of our detector to comparable LIF detectors for capillary electrophoresis.

4.3.5 Gel Filtration Chromatography

To demonstrate the utility of the high-power LED detector as a fluorescence detector in chromatography, a gel filtration chromatography experiment was performed to separate bovine serum albumin (BSA) from a fluorescent label, fluorescein isothiocyanate (FITC). Figure 4.15 shows a typical separation of labelled BSA from the excess FITC. The peak due to excess FITC, beginning at 8.2 min, saturates the PMT. The dynamic range of the detector spans from 0.025 to 2.5 nM, or two orders of magnitude. The limit of detection for FITC-labelled BSA is 25 pM. This LOD is comparable to the LOD for continuous flow measurements after accounting for the dilution factor caused by the column. The LOD in this work is 50-fold greater than

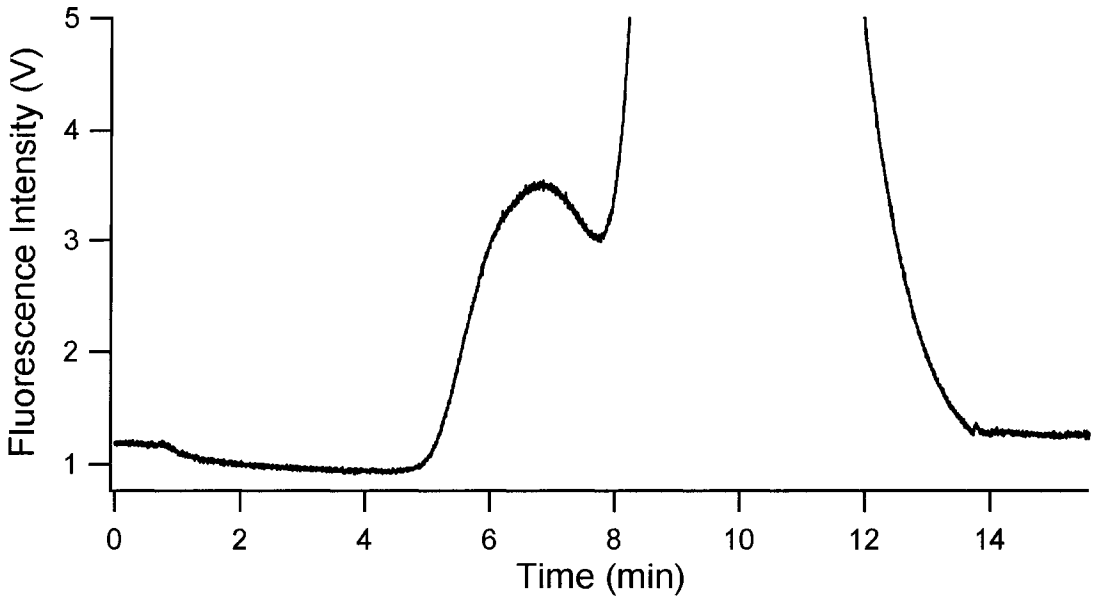

Figure 4.15 Gel filtration separation of 0.8 nM BSA from excess FITC label. The first peak is FITC-labelled BSA and the second, saturating peak is excess FITC. The column eluent is directed through 200 μm i.d. tubing, and a 3.5 mm pinhole is used to spatially filter the fluorescent signal.

reported in a laser-based detector,[43] but nonetheless provides limits of detection which are very competitive with other LED-based work.[4, 5]

4.4 Conclusion

The introduction of powerful LEDs into fluorescence detectors allows for high sensitivity at a very low cost. To make efficient use of the LED light, consideration has been given to spectral filtering, optical arrangement, detector cell size, and spatial filtering. A limit of detection of 3 pM was observed for continuous fluorescence measurements of fluorescein with the right-angle detector geometry. A LOD of 25 pM was observed for FITC-labelled BSA separated by gel filtration chromatography.

4.5 References

(1) Dasgupta, P. K.; Zhang, G. F.; Li, J. Z.; Boring, C. B.; Jambunathan, S.; Al-Horr, R. *Anal. Chem.* **1999**, *71*, 1400-1407.

(2) Manor, R.; Datta, A.; Ahmad, I.; Holtz, M.; Gangopadhyay, S.; Dallas, T. *IEEE Sensors Journal* **2003**, *3*, 687-692.

(3) Chen, S. J.; Chen, M. J.; Chang, H. T. *J. Chromatogr. A* **2003**, *1017*, 215-224.

(4) de Jong, E. P.; Lucy, C. A. *Anal. Chim. Acta* **2005**, *546*, 37-45.

(5) Kuo, J. S.; Kuyper, C. L.; P.B., A.; Fiorini, G. S.; Chiu, D. T. *Electrophoresis* **2004**, *25*, 3796 - 3804.

(6) Su, A. K.; Lin, C. H. *J. Chromatogr. B* **2003**, *785*, 39-46.

(7) Yang, B. C.; Tan, F.; Guan, Y. F. *Talanta* **2005**, *65*, 1303-1306.

(8) Yang, B. C.; Guan, Y. F. *Anal. Sci.* **2003**, *19*, 633-634.

(9) Bruno, A. E.; Maystre, F.; Krattiger, B.; Nussbaum, P.; Gassmann, E. *Trends Anal. Chem.* **1994**, *13*, 190-198.

(10) Guo, Y. L.; Uchiyama, K.; Nakagama, T.; Shimosaka, T.; Hobo, T. *Electrophoresis* **2005**, *26*, 1843-1848.

(11) Hofmann, O.; Wang, X. H.; deMello, J. C.; Bradley, D. D. C.; deMello, A. J. *Lab on a Chip* **2005**, *5*, 863-868.

(12) Miyaki, K.; Guo, Y. L.; Shimosaka, T.; Nakagama, T.; Nakajima, H.; Uchiyama, K. *Analytical and Bioanalytical Chemistry* **2005**, *382*, 810-816.

(13) Yang, B. C.; Guan, Y. F. *Talanta* **2003**, *59*, 509-514.

(14) Li, Q. Y.; Dasgupta, P. K.; Temkin, H.; Crawford, M. H.; Fischer, A. J.; Allerman, A. A.; Bogart, K. H. A.; Lee, S. R. *Appl. Spectrosc.* **2004**, *58*, 1360-1363.

(15) McGuinness, C. D.; Sagoo, K.; McLoskey, D.; Birch, D. J. S. *Meas. Sci. Technol.* **2004**, *15*, L19-L22.

(16) McGuinness, C. D.; Sagoo, K.; McLoskey, D.; Birch, D. J. S. *Appl. Phys. Lett.* **2005**, *86*.

(17) Sluszny, C.; He, Y.; Yeung, E. S. *Electrophoresis* **2005**, *26*, 4197-4203.

(18) Lee, D. S.; Chang, B. H.; Chen, P. H. *Sensors and Actuators B-Chemical* **2005**, *107*, 872-881.

(19) Wu, J. Y.; Delwiche, M. J.; Cullor, J.; Smith, W. *Biosystems Engineering* **2005**, *90*, 143-151.

(20) Yu, L. J.; Yuan, L. L.; Feng, H. T.; Li, S. F. Y. *Electrophoresis* **2004**, *25*, 3139-3144.

(21) Zukauskas, A.; Novickovas, A.; Vitta, P.; Shur, M. S.; Gaska, R. *J. Raman Spectrosc.* **2003**, *34*, 471-473.

(22) Kang, J. S.; Piszczek, G.; Lakowicz, J. R. *Biochimica Et Biophysica Acta-Proteins and Proteomics* **2002**, *1598*, 196-196.

(23) O'Hagan, W. J.; McKenna, M.; Sherrington, D. C.; Rolinski, O. J.; Birch, D. J. S. *Meas. Sci. Technol.* **2002**, *13*, 84-91.

(24) Hauser, P. C.; Liang, C. L. C.; Muller, B. *Meas. Sci. Technol.* **1995**, *6*, 1081-1085.

(25) Li, J. Z.; Dasgupta, P. K. *Anal. Chem.* **2000**, *72*, 5338-5347.

(26) Li, J. Z.; Dasgupta, P. K. *Anal. Sci.* **2003**, *19*, 517-523.

(27) Li, J. Z.; Dasgupta, P. K.; Genfa, Z.; Hutterli, M. A. *Field Analytical Chemistry and Technology* **2001**, *5*, 2-12.

(28) Li, J. Z.; Dasgupta, P. K.; Li, G. G.; Motomizu, S. *Anal. Chem.* **2003**, *75*, 6753-6758.

(29) Li, J. Z.; Dasgupta, P. K.; Tarver, G. A. *Anal. Chem.* **2003**, *75*, 1203-1210.

(30) Toda, K.; Dasgupta, P. K.; Li, J. Z.; Tarver, G. A.; Zarus, G. M.; Ohira, S. *Anal. Chem.* **2001**, *73*, 5716-5724.

(31) Toda, K.; Dasgupta, P. K.; Li, J. Z.; Tarver, G. A.; Zarus, G. M.; Ohira, S. *Anal. Sci.* **2001**, *17 Supplement*, i407 - i410.

(32) Toda, K.; Ohira, S.; Tanaka, T.; Nishimura, T.; Dasgupta, P. K. *Environmental Science & Technology* **2004**, *38*, 1529-1536.

(33) http://www.luxeon.com/.

(34) Cheng, Y. F.; Dovichi, N. J. *Science* **1988**, *242*, 562-564.

(35) Wu, S. L.; Dovichi, N. J. *J. Chromatogr.* **1989**, *480*, 141-155.

(36) Grama, L.; Somogyi, B.; Kellermayer, M. S. Z. *Proc. Natl. Acad. Sci. U. S. A.* **2001**, *98*, 14362-14367.

(37) Harris, D. C. In *Quantitative Chemical Analysis,* 5th ed.; Harris, D. C., Ed.; W.H. Freeman and Co.: New York, 1999, pp 89-90.

(38) Fischer, A. L. *Photonics Spectra* **2006**, *40*, 90-92.

(39) Jenkins, F. A.; White, H. E. In *Fundamentals of Optics,* 4th ed.; Fry, R. A., Vinnicombe, A. T., Eds.; McGraw-Hill: New York, 1976.

(40) Piruska, A.; Nikcevic, I.; Lee, S. H.; Ahn, C.; Heineman, W. R.; Limbach, P. A.; Seliskar, C. J. *Lab on a Chip* **2005**, *5*, 1348-1354.

(41) Wabuyele, M. B.; Ford, S. M.; Stryjewski, W.; Barrow, J.; Soper, S. A. *Electrophoresis* **2001**, *22*, 3939-3948.

(42) Cheng, Y. F.; Wu, S. L.; Chen, D. Y.; Dovichi, N. J. *Anal. Chem.* **1990**, *62*, 496-503.

(43) Eggertson, M. J.; Craig, D. B. *Biomedical Chromatography* **2000**, *14*, 156-159.

(44) Bachteler, G.; Drexhage, K. H.; Ardenjacob, J.; Han, K. T.; Kollner, M.; Muller, R.; Sauer, M.; Seeger, S.; Wolfrum, J. *J. Lumin.* **1994**, *62*, 101-108.

(45) Craig, D. B.; Wong, J. C. Y.; Dovichi, N. J. *Anal. Chem.* **1996**, *68*, 697-700.

(46) Kamholz, A. E.; Schilling, E. A.; Yager, P. *Biophys. J.* **2001**, *80*, 1967-1972.

CHAPTER FIVE. DNA Separations

5.1 Introduction

Electrophoretic separations of DNA have made tremendous gains since their humble beginnings in the slab gel format. Automated capillary array instruments have helped to greatly increase the speed and reduce the cost of sequencing the genome of an organism.[1] However, medical practitioners continue to express an interest in improving sequencing technology. Knowing a person's entire genome can allow doctors and geneticists to identify which diseases or medical conditions that individual is prone to contracting. This knowledge allows for very early preventative medicine to be employed. Currently, the cost of sequencing the genome of a complex organism is roughly $10M. Future goals are to reduce this cost to $100,000 or $1000.[2] Clearly, these ambitious goals will require innovations from all branches of science. In this chapter, the applicability of the LED-fluorescence detector for genomic studies is evaluated.

5.1.1 Sequencing Basics

Sequencing refers to any technique used to determine the primary sequence of an unbranched biopolymer (usually protein or DNA). DNA sequence is fundamentally related to the central dogma of biochemistry, simplified as DNA $\rightarrow$ RNA $\rightarrow$ protein $\rightarrow$ cellular processes. All cellular processes are carried out by enzymes (proteins). DNA, transcribed to RNA, determines which proteins will be produced by an organism. Thus, knowing the genome allows one to predict which proteins might be expressed and which

cellular processes are relevant to a given organism. Knowledge of DNA sequence is also critical for manipulation of the DNA molecule, used for gene insertion and genetic engineering. The nucleotides of which DNA is comprised are shown in Appendix 14.

The concept of DNA sequencing was introduced almost simultaneously by Maxam and Gilbert at Harvard University and Sanger at Cambridge. Gilbert[3] and Sanger[4] shared the 1980 Nobel Prize in Chemistry "for their contributions concerning the determination of base sequences in nucleic acids". Gilbert and co-workers devised a sequencing method whereby radiolabelled DNA is chemically degraded by four separate reactions, each specific to a different base. The labelled, degraded strands of DNA are separated by electrophoresis and visualized by autoradiography.[3] This technique is known as chemical degradation, or the Maxam-Gilbert method. The method developed by Frederick Sanger has become known as the chain termination, dideoxy, or Sanger method. The names "chain termination" and "dideoxy" arise from the fact that this technique involves the enzymatic extension of a strand of DNA *complementary* to the DNA of interest, or "template" strand. This chain extension is terminated by the presence of dideoxy nucleotides, which are incorporated into the DNA strand. However, once a strand incorporates a dideoxy nucleotide, it is then no longer recognized by the polymerase enzyme, resulting in chain termination.[4] It is interesting to note that the Maxam and Gilbert paper has been cited nearly 7000 times as of November 2006, and the Sanger paper nearly 63,000 times, undoubtedly making it one of the most-cited scientific papers to date. Relative to the Sanger technique, the Maxam-Gilbert method has a number of disadvantages including slower and less reliable reactions, and the use of several hazardous chemicals. Thus, for all but a few specialized applications, the Sanger

method has become by far the most widely used approach for DNA sequencing.[5] However, a new sequencing technique, based on chemiluminescent reactions specific to each nucleobase, has recently emerged. Known as *pyrosequencing*, this method boasts much improved throughput, since on average 200,000 sequencing reactions can be performed in parallel on a PicoTiter Plate™. A strand of complementary DNA is formed to the target genomic DNA by a modified polymerase reaction. This reaction is modified to produce chemiluminescence every time a chain extension event occurs. Chemiluminescence from each well is collected by a CCD camera beneath the PicoTiter plate, which monitors all the wells simultaneously.[6] It remains to be seen whether pyrosequencing can compete with a new 10,000 capillary array electrophoresis system, replying on Sanger reaction technology.[7]

5.1.2 Sequencing Reactions

Although there are various minor modifications possible, the basic concepts of DNA sequencing are illustrated in Figure 5.1. In step 1, four reaction tubes are prepared, each containing a different dideoxynucleotide (ddNTP). The reaction tubes are placed in a thermocycler where the template DNA is denatured to give single-stranded DNA (ssDNA; step 2a). A primer is a relatively short strand of DNA (15-20 bases) whose sequence is complementary to the target DNA. Addition of a primer complementary to the 3' end of the target DNA ensures that the polymerase reaction, explained below, proceeds from the end of the target DNA rather than some randomly selected site in the middle of the molecule. Slightly below the DNA's melting temperature, fluorescently labelled primer can anneal to the ssDNA without mismatches or the formation of

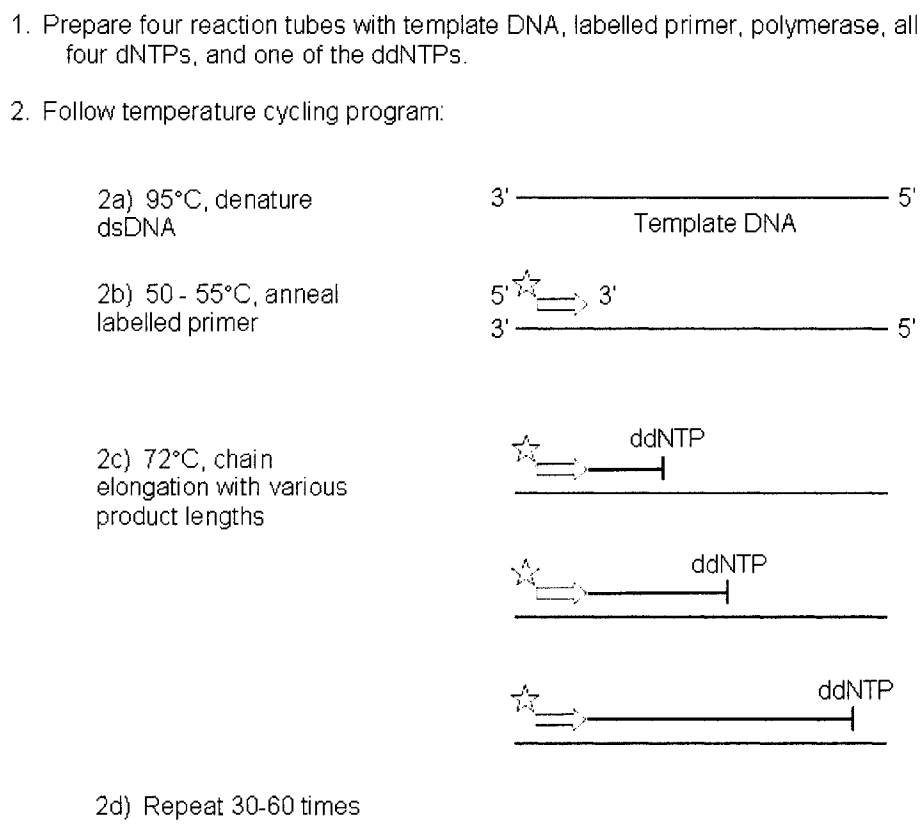

Figure 5.1 Process of DNA sequencing. Straight lines represent template (target) DNA, stars represent a fluorescent tag, arrows represent the primer, and lines with a vertical tail are newly synthesized, complementary DNA, terminated with a ddNTP.

secondary structure (step 2b). At 72°C, the optimum temperature for *Thermus aquaticus* (Taq) DNA polymerase, the primer is extended at the 3' end by incorporating deoxynucleotides (dNTPs) and, occasionally, a ddNTP. The ddNTP causes termination of the primer strand which can not be extended by the polymerase, hence the name(s) of the method. The dNTPs are present in a 100-fold molar excess compared to the ddNTPs, and the random incorporation of ddNTPs into the newly formed DNA strand results in a *distribution* of extended primer fragment sizes. This temperature cycling can be repeated several times in order to obtain more primer fragments, thus increasing the sensitivity of the method. Prior to analyzing the fragments, the sample is heated once more to separate the template DNA from the fragments, then diluted with formamide or concentrated urea solution to prevent annealing of any DNA.

5.1.3 Sequencing Separations

Determining the DNA sequence from these fragments is based on their size, and molecular biologists classically use slab gel electrophoresis for this purpose. The four uniquely terminated reactions are placed in parallel lanes in a slab gel, and a solution of standard size markers is run in parallel. A schematic of such a run is shown in Figure 5.2. The left lane in Figure 5.2 is a size ladder which contains DNA fragments of known size, thereby acting as an internal standard. The other lanes are the reaction products of the four uniquely terminated reactions, and the fragments in these reactions allow one to determine the sequence of nucleobases *complementary* to the template DNA. Clearly it is necessary to achieve single-base resolution in this electrophoretic separation. A typical primer length is 18 nucleotides, and each sequencing reaction is expected to have excess

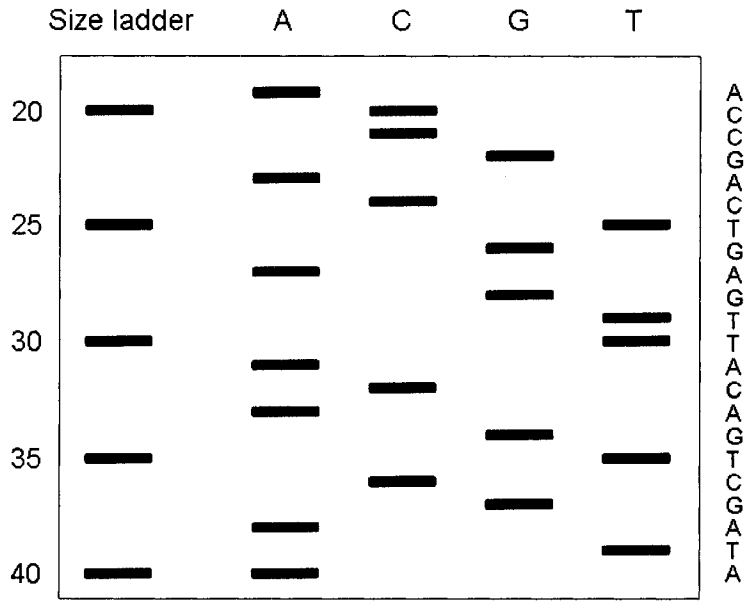

Figure 5.2 Schematic of DNA sequence determination by multi-lane slab gel electrophoresis. The size of the DNA strands, determined from the bands in the size ladder, is indicated on the left. Subsequent nucleobases beyond the primer in the extended DNA strand can be deduced from the size of the fragments, and is indicated on the right.

primer present (bands omitted from Figure 5.2). The shortest reaction product in this fabricated example appears in lane A, where the sequence has been terminated with ddATP. The presence of the DNA size ladder allows the reader to confirm that the size of this fragment is 19 bases. Because the labelled, complementary strand incorporates an A immediately after the primer, the template DNA must have contained a T. This process of deduction is continued until the entire DNA sequence is determined. This process typically required 12 hours for electrophoresis, 12 hours for autoradiography of the radiolabelled gel, and several more hours to determine the DNA sequence. The latter was "*an error-prone and mind-numbing exercise*".[1] Many improvements to this format have since been made. The use of radiolabelling has been replaced with laser-induced fluorescence detection, slab gel electrophoresis has been replaced with capillary arrays, and manual sequence reading has become entirely automated. The advantage of capillary (gel) electrophoresis over slab gel electrophoresis is typically claimed as the improved heat dissipation in small capillaries, allowing for higher electric fields and thus, faster separations. However, in the case of high throughput DNA sequencing, the primary benefit of using capillaries is not their heat dissipation but rather the ease of automation. Current DNA sequencers employ an array of 96 capillaries with detection performed by a linear sheath flow array or confocal detection. The detection methods are specifically described below in Section 5.1.4. For a discussion of sheath flow detection, see Sections 4.2.2.2 and 4.3.3.3.

5.1.4 Detection Techniques

A host of labelling techniques are possible for DNA sequencing. The label can be placed on the ddNTPs, on the dNTP, or on the primer. Labelled ddNTPs are still used occasionally, but the use of labelled dNTPs is now quite rare. The most common labelling scheme involves labelling the primer since energy-transfer primers can be made which require only one laser for four-colour sequencing (see below). Initially, a single fluorophore or radiolabel was used for this purpose, but it soon became apparent that throughput could be quadrupled by using a four-colour fluorescence detector.[8] Smith *et al.* used a different fluorophore for each of the four bases, with approximately 30 nm spacing between each fluorescence emission maximum. Excitation was performed using two common emission lines from a single argon-ion laser (488.0 and 514.5 nm). The ~100 nm span of excitation maxima for the fluorophores meant than even with two-colour excitation, there was significant variation in emission intensity.[8] Prober *et al.* introduced a system whereby a single laser wavelength could be used to excite four fluorophores with closely spaced excitation spectra. Fluorescence from the different fluorophores could be distinguished by their characteristic emission ratio viewed through two different emission filter sets.[9] Eventually Mathies' group introduced energy transfer (ET) dyes.[10] These contain a common donor fluorophore on the primer and one of four acceptor fluorophores located 10 nucleotides further along the primer chain. The emission maximum of each emitter fluorophore is at least 25 nm from the maxima of other fluorophores. These doubly-labelled primers can all be excited at the same wavelength, and due to Förster resonance energy transfer (FRET), emission is primarily from the acceptor fluorophore. Each of the four sequencing reaction tubes (for A, T, G

and C) is given a primer with one of rhodamine 110, rhodamine 6G, tetramethylrhodamine or rhodamine-X acceptor dye. The reaction products are then combined prior to analysis, allowing all four bases to be determined in the same lane on a slab gel, or in the same capillary of an array. This is the labelling approach used in most commercial sequencing kits (DYEnamic™ by Amersham Biosciences and BigDye™ by Applied Biosystems) and is the format for which most commercial capillary array sequencers have been designed.

Two commercial DNA capillary array sequencers exist, the ABI Prism from Applied Biosystems and the MegaBACE from Amersham Biosciences (now GE Healthcare). These instruments differ in their detection optics. The ABI Prism uses post-capillary or postcolumn fluorescence detection, as first introduced by Dovichi and co-workers for a single capillary.[11] As shown in later developments of this instrument, the detection can be performed on an array of capillaries using the sheath-flow detection mode.[12] In this configuration, a rectangular sheath flow cuvette is employed, thus accommodating the capillary array and the flow of sheath fluid (Figure 5.3). Two laser beams at 488 and 543.5 nm are aligned co-linearly to create a beam along the long axis of the cuvette, thus simultaneously exciting all sample streams. Detection of fluorescence from each channel is continuously monitored with a CCD camera after appropriate spectral filtering. This yields a considerably greater duty cycle (the fraction of time that signal from each capillary is being monitored) compared to the MegaBACE optical configuration, described below. Consequently, this configuration claims better limits of detection.

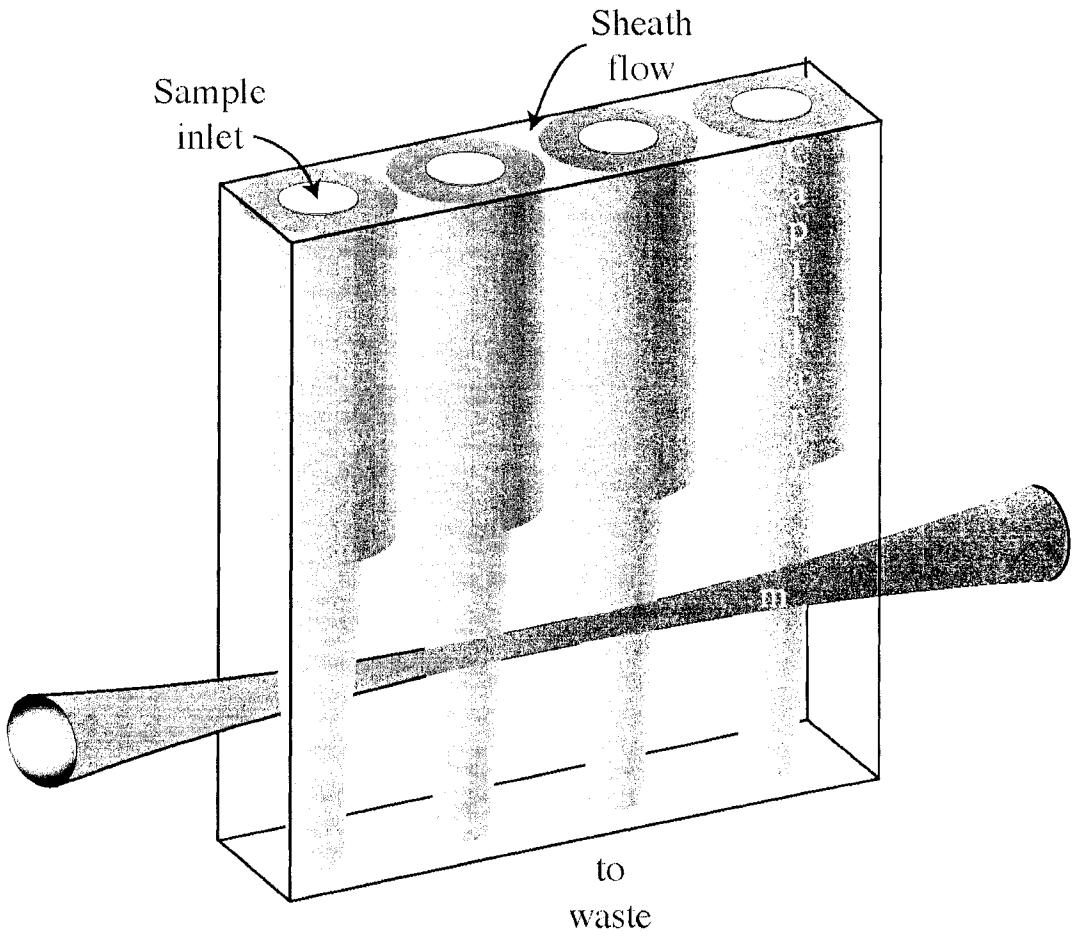

Figure 5.3 Rectangular sheath-flow cuvette for capillary array electrophoresis. The cuvette can accommodate four capillaries. Laser light is directed slightly below the end of the capillaries to excite fluorescence. Image courtesy of Dr. Norman Dovichi, Department of Chemistry, University of Washington, Seattle, WA, USA. Reproduced with permission from *Angewandte Chemie, Int. Ed.*

The MegaBACE instrument employs confocal, on-capillary fluorescence detection optics first introduced by Mathies and co-workers.[13, 14] Light from an argon-ion laser at 488 nm is expanded, collimated and reflected by a dichroic filter toward a microscope objective. The laser light is focussed on a bundle of aligned, even spaced capillaries which are mounted on a translation stage. Fluorescence light is collected by the same objective, passed through the dichroic filter, focused by a lens on a pinhole, filtered by a bandpass filter, and detected by a PMT. Later, a four-colour instrument was introduced where a separate detection channel exists for each fluorophore of the ET dyes. As shown in Figure 5.4, the emission beam is successively split by longer wavelength dichroic filters, towards a bandpass filter, lens, pinhole and PMT. Very rapid scanning is possible, allowing each capillary in the array to be sampled at 1 kHz.

5.1.5 Sieving Matrices

Capillary gel electrophoresis was first shown by Cohen and Karger, who separated proteins and peptides in SDS-PAGE mode.[15] DNA sequencing was first demonstrated in modern CE by Gesteland[16] and Smith,[17] although Karger and co-workers had previously shown single-base resolution of oligonucleotides.[18] These early studies all used chemically cross-linked polyacrylamide as the sieving matrix. This matrix is so viscous that its injection into a capillary is essentially impossible. Consequently, polymerization must be performed inside the capillary resulting in a permanently filled capillary. Cross-linked poly(acrylamide) capillaries proved susceptible to air bubble formation and gradual loss of current due to increasing resistivity near the inlet end. Zhu

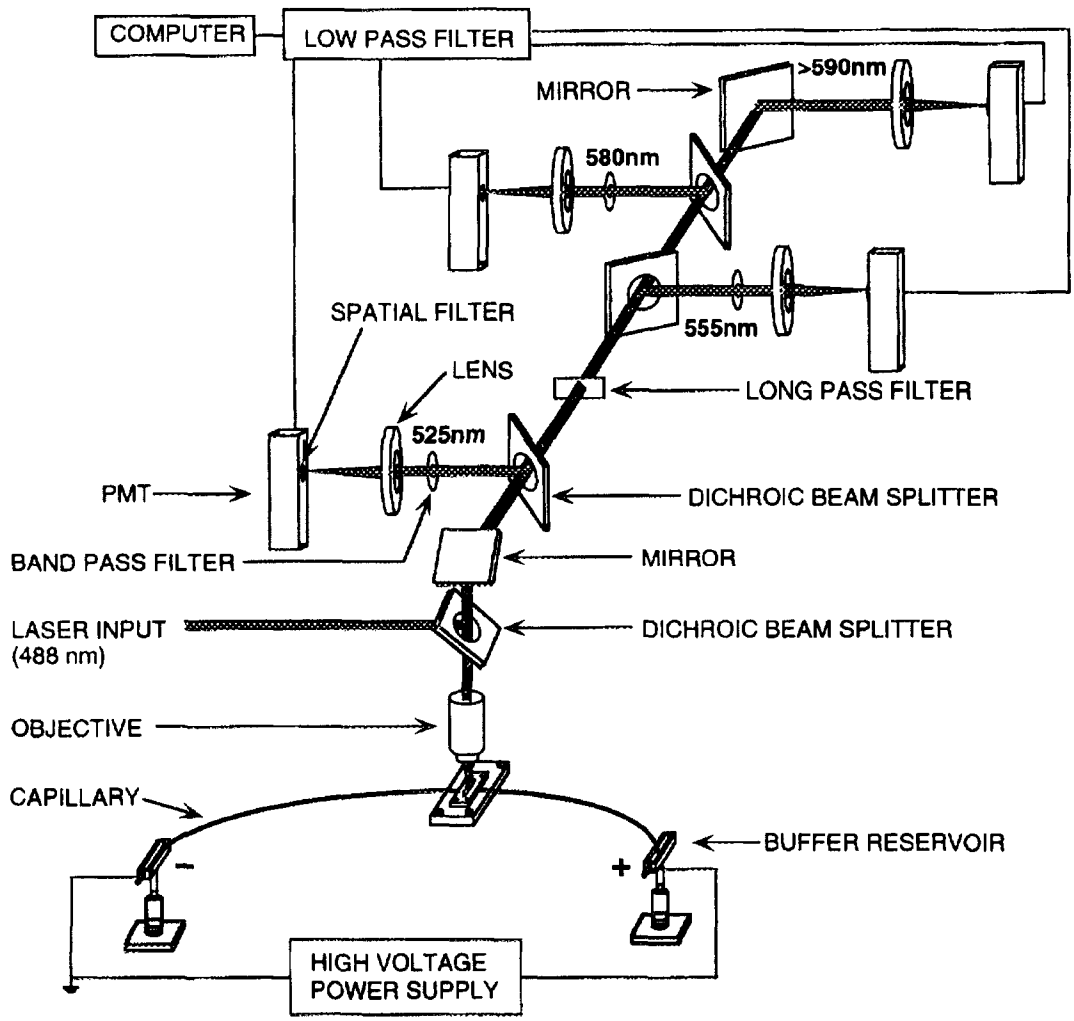

Figure 5.4 Illustration of the four-colour fluorescence detection scheme used in the MegaBACE DNA sequencer. Not shown is the translation stage which allows the detector to scan an array of capillaries. Image courtesy of Dr. Richard Mathies' Laboratory, U.C. Berkeley. Reprinted from *Analytical Biochemistry*, **231**, Ju, J.Y., Kheterpal, I., Scherer, J.R., *et al.*, Design and Synthesis of Fluorescence Energy Transfer Dye-Labeled Primers and Their Application for DNA Sequencing and Analysis, 131-140, 1995, with permission from Elsevier.

et al. introduced the use of non-crosslinked, linear polymeric matrices for sieving in CE, using hydroxypropylmethylcellulose, methylcellulose or poly(ethylene glycol) to separate DNA fragments or protein oligomers.[19] Such polymeric matrices are also called a "physical gel". Karger's group emphasized the use of linear poly(acrylamide) as a moderate viscosity, replaceable matrix for capillary gel electrophoresis.[20, 21] When present at a concentration at or above its *entanglement threshold* (also referred to as *overlap threshold*[22] or *critical aggregation concentration*[23]), the polymer strands will become tangled, forming a mesh. At low electric field strengths, the Ogston model[24] can be used to describe the passage of a molecule (of DNA in our case) through a polymer network. However, the Ogston model predicts that a DNA molecule whose radius of gyration is greater than the average pore size of the network can not penetrate the network. Quite the opposite has been observed, and consequently it is necessary to invoke the *reptation mechanism.*[25] Here the analyte polymer is presumed to elongate under the influence of the electrical field and to "snake" its way through the polymer network, head-first. In the limit of zero electric field, the mobility of an analyte is inversely proportional to its molecular length.[26] A further refinement to this model, proposed by Lumpkin *et al.*, incorporates the effect of large electric field strengths, where the DNA molecule becomes further elongated and its mobility is approximated as $\mu \approx K(N^{-1} + bE^2)$ where K is a constant, N is the number of repeating units of the analyte molecule (for our purposes the number of base pairs or molecular weight can be used), b is a function of the network pore size and E is the electric field strength.[27] This important refinement is known as the *biased reptation model.* Thus for high molecular weight DNA, mobility ceases to depend on the chain length. It has been estimated that a

practical limit of 20,000 base pairs (bp) exists for DNA separations on agarose gels,[28] however automated capillary array sequencers seldom exceed read lengths of 1000 bases.

Since these early studies on linear polymeric sieving matrices, much effort has been invested in optimizing the sieving polymer. Some of the most-studied polymers are hydroxyethylcellulose (HEC), hydroxypropylmethylcellulose (HPMC), poly(ethylene oxide) (PEO), poly(vinyl pyrrolidone) (PVP), linear poly(acrylamide) (LPA) and poly(*N*,*N*-dimethylacrylamide) (PDMA). The latter two have become the polymers of choice in automated DNA sequencers. Practical considerations regarding polymer selection include its ability to form a mesh size suitable for the desired separation, and the solution viscosity. The solution's intrinsic viscosity, $[\eta]$, is proportional to M_w^a, where a typically lies between 0.5 and 1. Above the entanglement threshold, a log-log plot of viscosity *vs.* polymer concentration shows strong positive deviation from linearity, indicating that the solution viscosity increases very rapidly above the entanglement threshold. Such behaviour serves only to lengthen the time required to replace the gel in a capillary. It is always desirable to use the polymer at the lowest concentration while still producing an acceptable separation.

5.1.6 LED-Fluorescence Detectors for DNA Separations

With recent improvements in LED technology, several groups have begun to employ LEDs for DNA sensing applications. Liu and Amirkhanian adapted a commercial capillary array to accept an array of LEDs, allowing detection of a DNA digest below 5 μg/mL.[29] Webster *et al.* were able to detect 6 μg/mL DNA using a pulsed blue LED with a lock-in amplifier for detection.[30] Single-molecule detection of DNA has

been achieved using a 150 mW LED.[31] The excellent sensitivity achieved here was attributed to the large DNA molecule (~ 48 kbp), which incorporated many intercalating dye molecules.[31] LEDs have also been used for real-time PCR detection of DNA, where a 20 μL sample vial was illuminated from below and detected from the side. A limit of detection of 0.01 fM was achieved after at least 30 PCR cycles (10^9-fold enhancement), giving a detector LOD of around 10 nM.[32] Chen and Ugaz have adapted a commercially-available microscope to accept an LED and an emission filter. Casting a micro-slab gel allowed real-time visualization of the separation. No limits of detection were reported.[33] Using a liquid core waveguide capillary, an LOD of 5 μg/mL was achieved with modulation of the LED.[34] Finally, a bubble cell for fluorescence detection on chip has been fabricated. This allowed for a 17-fold improvement in LOD, reaching as low as 0.1 μg/mL using a detector cell with 75 × 500 μm cross-section. Not surprisingly, peak efficiency was severely degraded in this detector.[35]

This chapter investigates whether the high-power LED fluorescence detector can be used to achieve superior sensitivity in genomics applications such as DNA sequencing and sizing a DNA digest.

5.2 Experimental

5.2.1 Apparatus

The instrument used in this chapter is identical to the epi-fluorescence detector described in Section 4.2.2.2. Both the 40× and 63× objectives were employed. Only 75 μm capillaries were used. Data was collected at 10 Hz, using a Pentium III 800 MHz PC.

5.2.2 Chemicals

Boric acid, ethylenediaminetetraacetic acid (EDTA) and urea were purchased from BDH (Toronto, ON, CA). Tris(hydroxymethyl)aminomethane (tris) was from ICN Biomedicals, Cleveland, OH, USA). Sodium hydroxide (10 M solution), acetone, isopropanol and formamide were from Fisher (Nepean, ON). Poly(vinylpyrrolidone) (PVP, average MW = 1,300,000), acrylamide (99+%, electrophoresis grade) and hydroxypropylcellulose (HPC, average MW = 100,000) were from Aldrich (Milwaukee, WI). Fluorescein sodium salt, 3-(trimethoxysilyl)propylmethacrylate (γ-methacryloxypropyltrimethoxysilane, MAPS, minimum 98%), ammonium persulfate (APS, approx. 99%), *N,N,N′,N′*-tetramethylethylenediamine (TEMED, approx. 99%, for electrophoresis), 4-morpholineethanesulfonic acid (MES, 98%) and 4-(2-hydroxyethyl)piperazine-1-ethanesulfonic acid (HEPES, ≥ 99.5%) were from Sigma (St. Louis, MO). A fluorescein-labelled DNA ladder (Sizer™ 50-500) was purchased from Amersham Biosciences (now GE Healthcare, Baie d'Urfé, QC). A DNA digest (ϕX174 RF DNA, *Hae* III Fragments, 0.5 μg/μL, discontinued) and SYBR-Gold (10,000× concentrate) were from Invitrogen (Carlsbad, CA). POP-6, CE buffer (Applied Biosystems, Foster City, CA) and single-stranded DNA from bacterial phage M13mp18 (abbreviated M13) were gifts from the Molecular Biology Services Unit (MBSU) of the Department of Biological Sciences at the University of Alberta. A poly-AT oligomer template[36] and FAM-(fluorescein) labelled primer suitable for both the AT oligomer and M13 were purchased from Integrated DNA Technologies, Inc. (Coralville, IA, USA). Their sequences were:

Primer = 5'-fluorescein-TCC CAG TCA CGA CGT TGT-3'

AT oligomer = 5'-$(T_5A_5)_5T_5$AC AAC GTC GTG ACT GGG-3'

Ultrapure water was obtained from a Nanopure water system (Barnstead, Dubuque, IO). Buffers were prepared by dissolving an appropriate amount of the conjugate acid in ultrapure water and adjusting the pH with 10 M NaOH while stirring.

A note on safety: acrylamide is a potent neurotoxin and care should be taken to avoid exposure, especially ingestion. Gloves should always be worn when working with acrylamide.

5.2.3 Sequencing Reactions

A 9.2 μM (203.3 μg/mL) stock solution of the AT template was made in 0.1 TE buffer (1 mM tris·HCl with 0.1 mM EDTA). The stock solution of primer was prepared at 35 μM (203.3 μg/mL). Working solutions were 0.1 μM AT template, 0.1 μM M13 template and 2.0 μM primer. DNA sequencing was performed using a Thermo Sequenase™ Dye Primer Manual Cycle Sequenase Kit (76260; USB Corp., Cleveland, OH, USA), as per the manufacturer's instructions. The reagents of the kit were thawed on ice, and the concentrated reaction buffer was diluted 1:10. Autoclaved 0.5 mL microcentrifuge tubes were used for the master reaction mixes. A master reaction mix was prepared by combining 9.8 μL distilled water, 2.5 μL of a DNA template working solution, 2.5 μL of the primer working solution, 2.2 μL of the diluted buffer and 1.0 μL of Taq polymerase (20 U/μL). This mixture was divided evenly into four thin-walled, 0.2 mL tubes for M13, or two tubes for the AT template. The four M13 tubes received 1 μL of either ddA, ddT, ddG or ddC terminator mix, containing 300 μM of each dNTP and 3

μM of the ddNTP. The two M13 tubes received 1 μL of ddA or ddT terminator mix. The reaction tubes were placed in a thermocycler (Eppendorf Mastercycler gradient, Westbury, NY) with a lid heated to 110 °C, preheated for 4 min. The sequencing reaction was performed at 95 °C for 30 s, 51 °C for 15 s, and 72 °C for 60 s. This cycle was performed 30 times. The reaction products were ethanol-precipitated, then re-dissolved in formamide containing 20% (v/v) 8mM EDTA.

5.2.4 DNA Fragment Labelling

Digested DNA (ϕX174 RF), was diluted 10-fold in 8 mM HEPES, 4 mM tris buffer, pH 7.6. SYBR-Gold 10,000× concentrate was diluted 125-fold in 1× TBE buffer (89 mM tris, 89 mM boric acid and 2 mM EDTA). The diluted DNA was mixed with 20 μL of the working solution of SYBR-Gold intercalating dye, giving 0.04 μg/μL DNA and 16× SYBR-Gold.

5.2.5 Electrophoresis

Various sample injection protocols were investigated, but due to irreproducible results, no optimum procedure could be determined. Hydrodynamic injections up to 200 mbar for 0.20 min were used. Because the polymer-filled capillary has much greater resistance to flow than a low-viscosity buffer alone, much greater sample injection pressure and/or time must be applied. Electrokinetic injections were also used, in the range of -5 to -15 kV for 0.05 to 0.15 min. Although electrokinetic injections suffer from a bias in favour of higher-mobility analytes, this is advantageous when using an

intercalating fluorescent dye for detection (Section 5.2.4). Larger DNA molecules incorporate many dye molecules, thus leading to a very high local concentration of fluorophore, and consequently give significantly larger signals in CGE electropherograms. The biased injection can by no means mitigate this effect, nor does it exacerbate the problem.

Separation voltages investigated ranged from -17.5 to -25 kV. The biased reptation model[37] predicts that at high field strengths, longer DNA strands will all have the same mobility. However, the practical limit of DNA separations is on the order of 20,000 base pairs[22] which is significantly larger than any samples used in this work. As no loss of resolution among larger fragments was observed when using -25 kV, this voltage seems appropriate.

The electroosmotic flow was measured in a 5% (w/v) PVP-filled capillary according to the procedure of Williams and Vigh.[38] The sample used in this case was 12.5 μM riboflavin in 1× TBE buffer. The specific procedure was as follows:

1. Sample was injected at 1000 mbar for 0.2 min
2. The capillary inlet was cleaned by dipping in water
3. PVP (in TBE) was injected at 1000 mbar for 3.0 min
4. Sample was injected at 1000 mbar for 0.2 min
5. The capillary inlet was cleaned by dipping in water
6. PVP was injected at 1000 mbar for 3.0 min
7. Electrophoresis was performed at -25 kV for 20 min, using PVP solution at the inlet and outlet capillary vials
8. Sample was injected at 1000 mbar for 0.2 min

9. Data collection was initiated manually concurrently with the injection of PVP at 1000 mbar until all three sample peaks were observed

The electroosmotic flow was also measured in a poly(acrylamide) wall-coated capillary and was found to be 0.095×10^{-4} $cm^2 \cdot V^{-1} \cdot s^{-1}$. This is similar to the value reported Terabe *et al*, 0.12×10^{-4} $cm^2 \cdot V^{-1} \cdot s^{-1}$.[39] Modifications of the above injection and electrophoresis pressure, voltage and time were required to observe an appropriate pattern of peaks. In bare silica, acid-rinsed capillaries using HEPES-tris buffer at pH 7.6, an eof of 1.5×10^{-4} $cm^2 \cdot V^{-1} \cdot s^{-1}$ was measured, with or without HPC. The eof of PVP-filled capillaries is discussed below in Section 5.3.1.

5.2.5.1 PVP as a Sieving Matrix

Poly(vinylpyrrolidone) was dissolved in nanopure water at a concentration of 5% (w/w). Three volumes of acetone/isopropanol (9:1 v/v) were then added to the PVP solution. Contrary to the literature procedure for PVP fractionation,[23] no phase separation was observed between the aqueous and organic phases upon standing overnight. Subsequent solutions of PVP were made either by dissolving PVP directly in 1× TBE buffer (89 mM tris, 89 mM boric acid and 2 mM EDTA), or by a modified fractionation procedure. The modified procedure began with making a 5% aqueous solution of PVP, followed by the addition of three volumes of acetone/isopropanol (9:1 v/v). This mixture was centrifuged (Allegra™ X-22R Centrifuge, Beckman-Coulter, Fullerton, CA) at 4500 rpm (3901 *g*) for 1-2 h, resulting in a phase separation. Although both phases were clear, there was clearly a difference in refractive index between the two phases, allowing one to distinguish one phase from the other. The upper phase was

discarded, leaving only a very viscous lower phase. The lower phase was decanted into a teflon-coated bowl and allowed to air-dry. The yield of fractionated PVP was typically ~50%. This polymer was redissolved at various concentrations in 1× TBE containing 7 M urea. The background fluorescence signal increased significantly when PVP solutions were introduced into the capillary. This problem was largely alleviated by vacuum degassing the polymer solutions for at least one hour prior to use.

5.2.5.2 POP-6™ as a Sieving Matrix

POP-6 solution was used as received in both bare capillaries and on capillaries covalently coated with linear polyacrylamide.[40] In some cases, 10 μL of SYBR working solution was added to 790 μL of POP-6 solution. For electrophoresis, the running buffer was either 1× TBE with 7M urea, or Applied Biosystems' CE buffer, of unknown composition.

Slight modifications to the literature procedure[40] for covalently coating a capillary with linear polyacrylamide were used, and so merit further explanation. A window was first burned into a new capillary (75/365 μm i.d./o.d.). A window can not be burned into a capillary after synthesizing the coating, as the temperature would destroy the inner polyacrylamide coating as well as the outer polyimide coating. The brittle window was protected by a temporary sheath capillary, approximately 5 cm of 544/667 μm capillary, held in place with a minimal amount of tape. The capillary to be coated was rinsed for 5-10 min with 1 M HCl, water, 1 M NaOH, water and 5% (v/v) acetic acid (HAc). In a CE vial, 1 mL of ethanol, 1 mL of 5% HAc and 60 μL of MAPS were mixed. This solution was flushed through the capillary for 5 min. The capillary ends were tightly wrapped in

parafilm, and was allowed to sit for 30 min. The MAPS solution was then rinsed through the capillary for an additional 5 min. The capillary was again sealed with parafilm and allowed to sit for one hour. During this time, 200 mg of acrylamide and 10 mg of APS were dissolved in 5 mL of nanopure water. This solution was thoroughly degassed with a stream of nitrogen. Immediately prior to using this solution, 5 μL of TEMED was added. This solution was rinsed through the capillary for 5 min and the capillary ends were again sealed. After 30 min, the now viscous acrylamide solution was rinsed from the capillary with fresh solution for 5 min. The capillary was sealed and allowed to sit for one hour. The viscous acrylamide solution was rinsed from the capillary with 5% HAc solution, which restored the capillary's original permeability. The capillary was also stored in 5% HAc, because the linear polyacrylamide coating is base-labile.

5.2.5.3 Hydroxypropylcellulose as a Sieving Matrix

Hydroxypropylcellulose was added in varying amounts to the HEPES-tris buffer (80 mM and 40 mM) at pH 7.6. This sieving matrix was used with an uncoated, acid-rinsed capillary, or in an poly(acrylamide)-coated capillary. In some cases, 10 μL of SYBR working solution was added to 790 μL of HPC solution. The aforementioned HEPES-tris buffer was used as the background electrolyte.

5.3 Results and Discussion

5.3.1 PVP Matrix

The use of PVP as a sieving matrix was first introduced by Yeung's group.[23] Two important benefits of this polymer were reported. First, solutions of PVP exhibit much lower viscosity than most other high-molecular weight entangled polymer solutions. For instance, PVP has a viscosity of 27 cP at 4.5% (w/v) at room temperature, compared to 1200 cP for a mixture of long and short PEO (1.5% of M_n = 8,000,000 and 1.4% of M_n = 600,000 PEO), or 4900 cP for linear polyacrylamide (M_n = 700,000 – 1,000,000; 6% solution).[41] This low viscosity allows for much more rapid replacement of the gel between runs. Instruments not designed to deliver very high pressures (> 200 kPa), such as that used in this thesis, can make use of this polymer while maintaining an acceptable time between runs. The second advantage of PVP as a sieving matrix is its ability to coat the capillary and suppress the electroosmotic flow. This coating ability has been attributed to the strong hydrogen bonds formed between PVP and residual silanol groups on the capillary surface. Yeung's group has reported a μ_{eof} of 6.0×10^{-6} $cm^2 \cdot V^{-1} \cdot s^{-1}$, as determined by the mobility of a neutral marker.[42] Consistent with the reported value, the μ_{eof} found here was 5.6×10^{-6} $cm^2 \cdot V^{-1} \cdot s^{-1}$, although this was determined using the three-injecting method of Williams and Vigh (Section 5.2.5).[38] However, PVP suffers from some disadvantages. Commercially available PVP has a high polydispersity index of 5-10.[43] Isolating and retaining the high-molecular weight fraction of this polymer is essential to achieving adequate viscosity for separation. The fractionation procedure in reference 22 could not be reproduced. This procedure states that three volumes of 9:1 acetone/isopropanol, added to one volume of aqueous PVP solution results in a phase

separation. Perhaps not surprisingly, no phase separation was observed. Two alternative approaches were explored. First, fractionation was induced by centrifugation as described in Section 5.2.5.1. While no attempts were made to characterize the resulting fractions, the retained fraction was found to be significantly more viscous than the discarded layer. It was apparent from the viscosity that the discarded layer contained some polymer, suggesting that only the high-molecular weight fraction was retained. The second approach was simply to avoid any fractionation procedure, rationalized by the fact that in reference 22, the M_n of PVP was 1,000,000, whereas that purchased in this work had an M_n of 1,300,000.

The low viscosity of PVP solutions made it possible to fill a capillary in approximately 15 min at 200 kPa (instrument setting of 2000 mbar). However, the overall reproducibility of electropherograms in PVP-filled capillaries was unacceptable. Hydrodynamic and electrokinetic injections were attempted, and successive runs were attempted with or without replacing the PVP matrix between runs. In almost all cases, the signal intensity and migration time reproducibility was extremely poor (75 – 125 %RSD and 7 – 16 %RSD, respectively). Consequently, the use of PVP was abandoned. A number of partially successful experiments were conducted however. In the analysis of DNA sequencing products, it was found that the sensitivity of the detector was marginal. Early DNA sequencing reactions were too dilute for adequate detection. Subsequent reactions were scaled up as described in Section 5.2.3, which gave a higher concentration of sequencing products in the injected sample solution. Figure 5.5 shows the best *resolution* obtained in the separation of sequencing products for M13 DNA. Clearly the sensitivity is slightly too low for proper peak identification. In contrast,

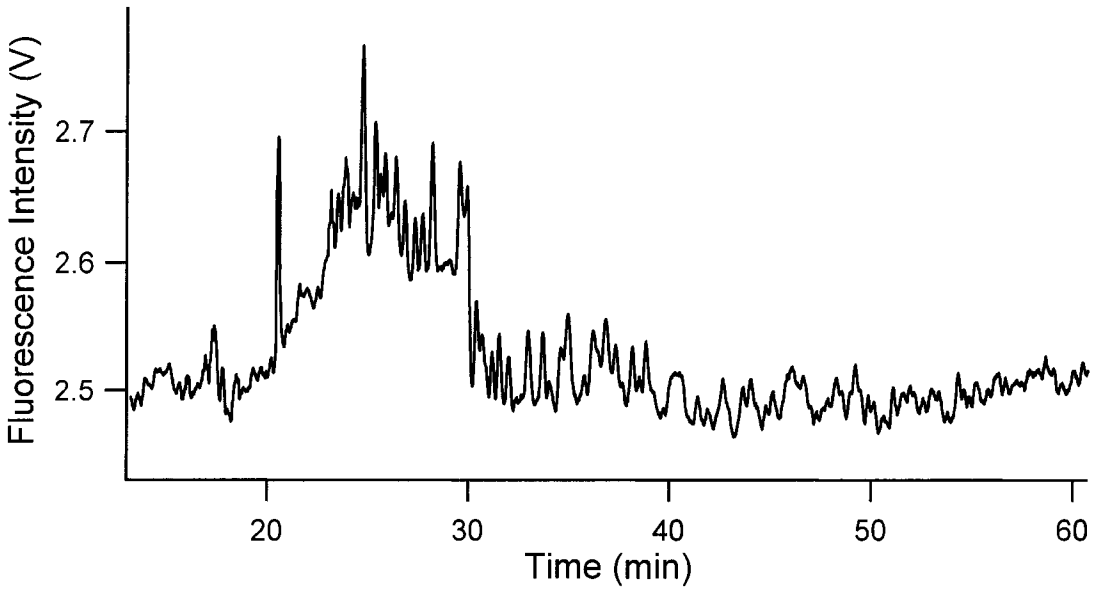

Figure 5.5 Separation of sequencing products of M13 DNA, terminated with ddATP. Conditions: Fragments were separated using 5% (w/v) extracted (high-MW) PVP in 1× TBE; sample was injected at 75 mbar for 6 s; electrophoresis occurred at -25 kV in 1× TBE BGE.

Figure 5.6 shows an example where adequate *sensitivity* could be achieved, but not adequate resolution.

The separation of a DNA ladder is shown in Figure 5.7. A poor peak efficiency of ~54,000 plates/m is obtained for the peak at 100 bp and the separation efficiency degrades to below 10,000 plates for the later peaks. These efficiencies are considerably worse than the 1.3 million plates/m achieved by Gao and Yeung.[23] Clearly, single-base resolution can not be achieved under these conditions.

5.3.2 POP-6™ Matrix

POP-6 consists of relatively low-mass, linear poly(*N*,*N*-dimethylacrylamide).[44] The solution was found to be extremely viscous and filling the capillary with this polymer took over two hours at 2000 mbar. Initially, it was assumed that polyacrylamide-coated capillaries were required when using POP-6 as a sieving matrix. It is difficult to determine and reproduce the exact experimental setup used in automated sequencers, as the reagents are almost always purchased from the manufacturer, and whose composition is unknown to the operator. Thus, early attempts at using POP-6 utilized a coated capillary, as described in Section 5.2.5.2. Similar to the use of PVP, reproducibility was the major problem when using POP-6 as a sieving matrix. Successive injections of fluorescein standard or DNA ladder seldom gave similar results in terms of either peak height, migration time, or even the appearance of any peaks. On one occasion, a successful separation of the DNA ladder was achieved, shown in Figure 5.8. Well-separated peaks are observed with efficiencies as high as 780,000 theoretical plates. Given the peak spacing and efficiency, this is an example where single-base efficiency

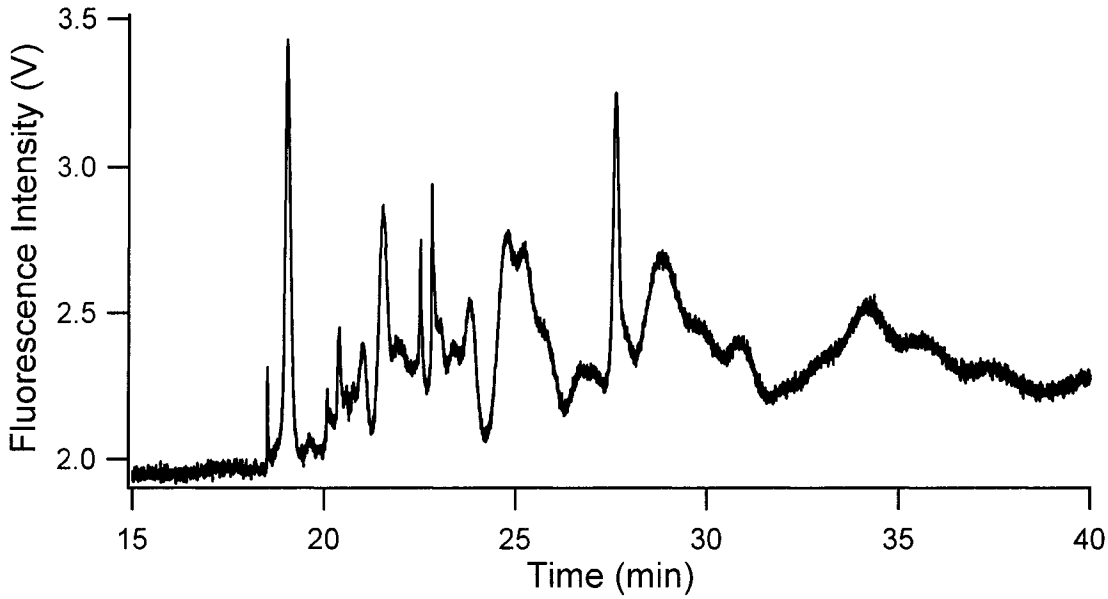

Figure 5.6 Separation of sequencing products of M13 DNA, terminated with ddCTP. Conditions: Fragments were separated using 3% as-received PVP, in 1× TBE; sample injected at 175 mbar for 9 s; electrophoresis occurred at -25 kV in 1× TBE BGE.

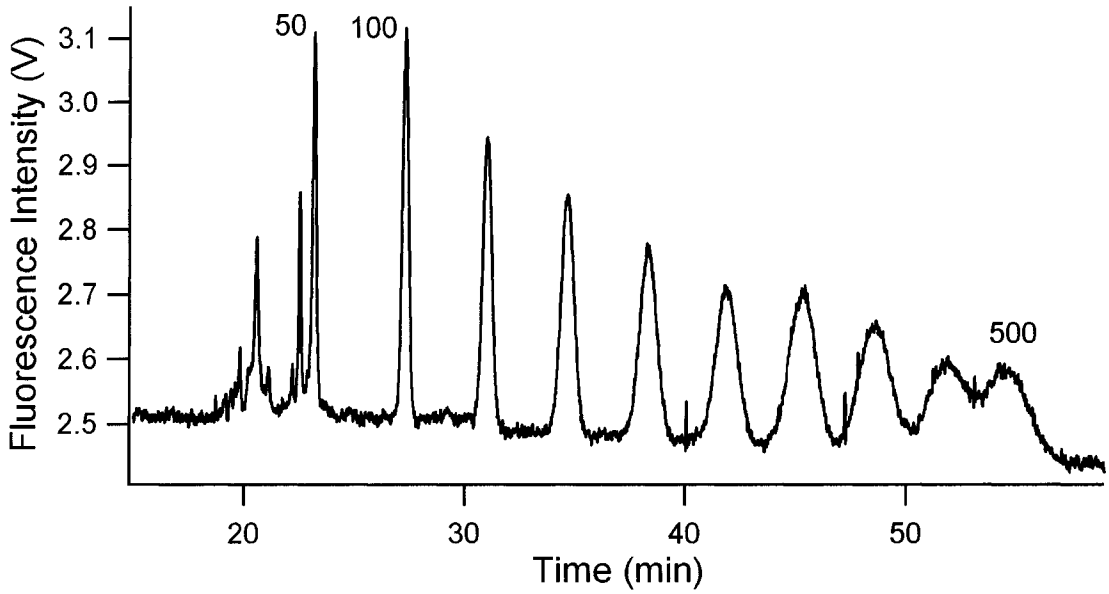

Figure 5.7 Separation of a DNA ladder using PVP as the sieving matrix. The DNA ladder contains DNA fragments of 50, 100, 150, ... 500 bases, as indicated by the peak numbers. Conditions: Fragments were separated using 5% (w/v) extracted (high-MW) PVP in 1× TBE; sample injected at 200 mbar for 9 s; electrophoresis occurred at -25 kV in 1× TBE BGE.

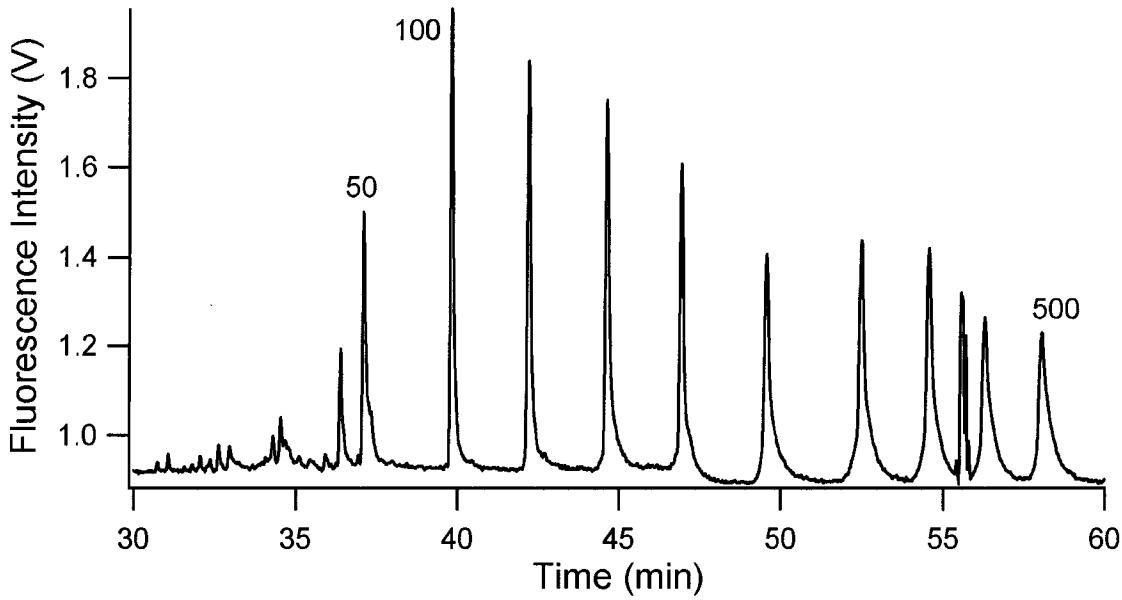

Figure 5.8 Separation of a DNA ladder using POP-6™ sieving matrix. The DNA ladder contains DNA fragments of 50, 100, 150, … 500 bases, as indicated by the peak numbers. Conditions: Fragments were separated using POP-6; sample injected at -10 kV for 6 s; electrophoresis occurred at -25 kV in 1× CE buffer from Applied Biosciences.

could conceivably be achieved. Modelling the insertion of 49 evenly-spaced peaks between peaks 100 and 150 reveals that a resolution of 0.16 would result, with peaks overlapping at 86% of their maximum height. This is indeed slightly poorer than work from Karger's group which allowed a resolution of 0.24.[45] However, given that sequencing instruments will routinely give "acceptable" readouts where peaks might overlap at 90% of their maximum height, Figure 5.8 would appear to be an acceptable separation for sequencing. Regrettably, the separation could not be reproduced.

Later experiments were conducted using bare silica capillaries, as it was discovered that POP-6 is a self-coating polymer.[44] No improvements in reproducibility were observed upon making this change.

5.3.3 HPC Matrix

HPC has been used successfully with an uncoated capillary.[46] The literature procedure used an extensive acid rinse to protonate the capillary walls, thereby allowing HPC to hydrogen-bond and form an eof-suppressing coating. A MES-tris buffer at pH 6.1 allows for adequate protonation of the capillary wall, without denaturing DNA (DNA denaturation occurs at pH ~4). A pH of 6.1 was not compatible with the fluorescent dye chosen in this work, SYBR-Gold. This dye exhibits optimum fluorescence between pH 7.5 and 8.3. Thus, a HEPES-tris buffer at pH 7.6 was employed. At pH 6, silica has an eof near 2×10^{-4} $cm^2 \cdot V^{-1} \cdot s^{-1}$, while at pH 7.6 this increases to 4×10^{-4} $cm^2 \cdot V^{-1} \cdot s^{-1}$.[47] The eof measured in an acid-rinsed capillary using HEPES-tris buffer was 1.5×10^{-4} $cm^2 \cdot V^{-1} \cdot s^{-1}$. Nonetheless, separation of a DNA digest was possible with this buffer, as shown in Figure 5.9. This separation clearly shows the effect of fragment length on fluorescent

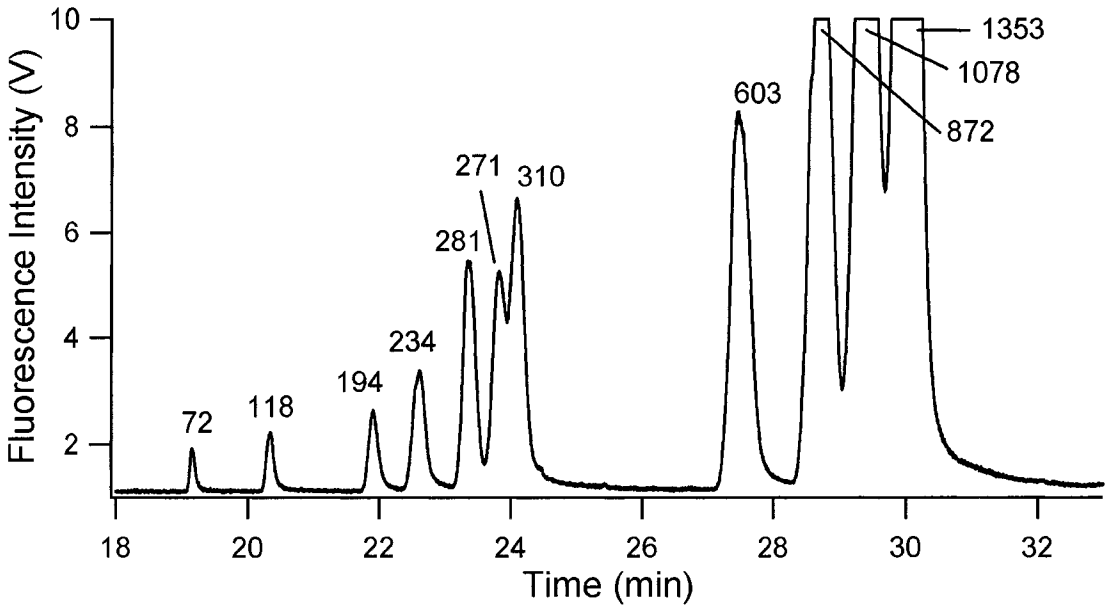

Figure 5.9 Separation of a DNA digest with HPC sieving matrix. The numbers above peaks are the number of bases in the DNA fragment. Conditions: Fragments were separated using 3.5% (w/v) HPC in HEPES-Tris buffer (80 and 40 mM) pH 7.5; sample was injected at -5 kV for 3 s; electrophoresis occurred at -20 kV in HEPES-tris buffer.

intensity. Longer fragments of DNA will incorporate more of the intercalating dye and have a greater local concentration of fluorescent dye and hence, a stronger signal. Figure 5.9 also illustrates the anomalous (reversed) migration of fragments 271 and 281 bp in length.[48] The efficiency of the 603 bp peak is approximately 10^5 plates/m, which is an order of magnitude worse than the 10^6 plates/m reported by Landers *et al.*[46] The sensitivity of the 603 bp peak in Figure 5.9 is comparable to that in reference 46, based on a visual inspection of the peak's signal-to-noise, and after correcting for the difference in sample concentration (2.5 μg/mL in reference 46 and 40 μg/mL in this work). However, when attempting to work at the same sample concentration as was used in reference 46 (or even 25 μg/mL), no signal was observed. It is unclear why the separations presented in this thesis gave low efficiency or a sudden decrease in sensitivity below 40 μg/mL.

The reproducibility of separations in HPC was improved by using a poly(acrylamide) coated capillary, due in part to the minimal eof in this capillary. Migration times became much more stable (< 4%) and, more importantly, the appearance of peaks in the electropherogram were consistently observed. This seemingly mandatory appearance of peaks was by no means a certainty when using other sieving matrices or uncoated capillaries with HPC. A significant drawback of using poly(acrylamide) capillaries was a noisier background signal, which showed many peaks (or spikes) not attributed to analyte species. These spikes are too narrow to be injected fluorescent species, since the peak efficiency is often an order of magnitude greater than the theoretical maximum. It is unclear whether or how the poly(acrylamide) coating is

responsible for this noisy background, shown in Figure 5.10. Neither boxcar averaging nor Savitzky-Golay smoothing proved effective in removing these background spikes.

5.4 Conclusions

DNA separations using an LED-fluorescence detector appear feasible, although more optimization is required before this becomes a routine analysis. Problems with separation reproducibility are the primary obstacle limiting these efforts. The use of PVP is attractive due to its low viscosity and eof suppression. But its use is hindered by a fractionation procedure which can not be re-created, unpredictable electrophoresis behaviour, and the need to de-gas PVP solutions for hours prior to use. POP-6™ was investigated on the assumption that a commercially available product should yield consistent results, however this expensive polymer did not live up to its name, "performance optimized polymer". Finally, HPC was used with reasonable success, as the DNA separations were usually successful when using this sieving matrix. Complications with HPC included electroosmotic flow in an uncoated capillary and a noisy background with a polyacrylamide-coated capillary. Some suggestions for improving the separation are given in Section 6.2.2, while improving the detector sensitivity is discussed in Section 6.2.1.

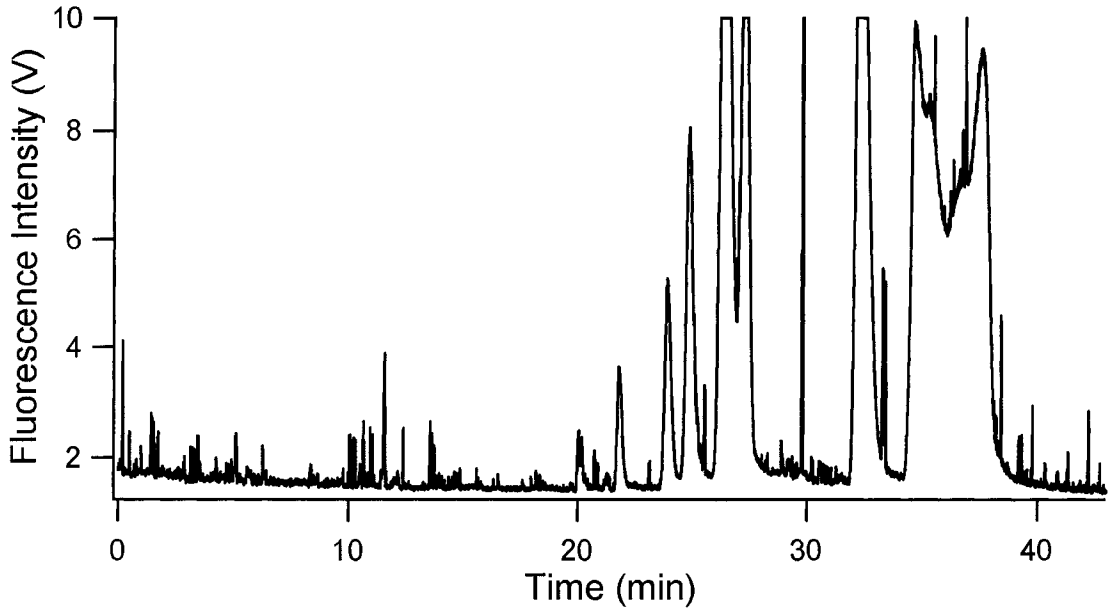

Figure 5.10 Separation of a DNA digest using a polyacrylamide-coated capillary and HPC sieving matrix. The numbers above peaks are the number of bases in the DNA fragment. Conditions: Fragments were separated using 3.5% (w/v) HPC in HEPES-Tris buffer (80 and 40 mM) pH 7.5; sample was injected at -5 kV for 6 s; electrophoresis occurred at -20 kV in HEPES-tris buffer.

5.5 References

(1) Dovichi, N. J.; Zhang, J. Z. *Angew. Chem., Int. Ed.* **2000**, *39*, 4463-4468.

(2) Fredlake, C. P.; Hert, D. G.; Mardis, E. R.; Barron, A. E. *Electrophoresis* **2006**, *27*, 3689-3702.

(3) Maxam, A. M.; Gilbert, W. *Proc. Natl. Acad. Sci. U. S. A.* **1977**, *74*, 560-564.

(4) Sanger, F.; Nicklen, S.; Coulson, A. R. *Proc. Natl. Acad. Sci. U. S. A.* **1977**, *74*, 5463-5467.

(5) Alphey, L. *DNA Sequencing: From Experimental Methods to Bioinformatics*; BIOS Scientific Publishers, Ltd.: Oxford, 1997.

(6) Margulies, M.; Egholm, M.; Altman, W. E.; Attiya, S.; Bader, J. S., *et al. Nature* **2005**, *437*, 376-380.

(7) Forest, C. R.; Thilly, W. G.; Hunter, I. W. In *21st International Symposium on Microscale Bioseparations (MSB)*: Vancouver, BC, Canada, 2007.

(8) Smith, L. M.; Sanders, J. Z.; Kaiser, R. J.; Hughes, P.; Dodd, C., *et al. Nature* **1986**, *321*, 674-679.

(9) Prober, J. M.; Trainor, G. L.; Dam, R. J.; Hobbs, F. W.; Robertson, C. W., *et al. Science* **1987**, *238*, 336-341.

(10) Ju, J. Y.; Ruan, C. C.; Fuller, C. W.; Glazer, A. N.; Mathies, R. A. *Proc. Natl. Acad. Sci. U. S. A.* **1995**, *92*, 4347-4351.

(11) Swerdlow, H.; Wu, S.; Harke, H.; Dovichi, N. J. *J. Chromatogr.* **1990**, *516*, 61-67.

(12) Zhang, J. Z.; Voss, K. O.; Shaw, D. F.; Roos, K. P.; Lewis, D. F., *et al. Nucleic Acids Res.* **1999**, *27*, E36.

(13) Huang, X. H. C.; Quesada, M. A.; Mathies, R. A. *Anal. Chem.* **1992**, *64*, 967-972.

(14) Kheterpal, I.; Scherer, J. R.; Clark, S. M.; Radhakrishnan, A.; Ju, J. Y., *et al. Electrophoresis* **1996**, *17*, 1852-1859.

(15) Cohen, A. S.; Karger, B. L. *J. Chromatogr.* **1987**, *397*, 409-417.

(16) Swerdlow, H.; Gesteland, R. *Nucleic Acids Res.* **1990**, *18*, 1415-1419.

(17) Drossman, H.; Luckey, J. A.; Kostichka, A. J.; D'Cunha, J.; Smith, L. M. *Anal. Chem.* **1990**, *62*, 900-903.

(18) Cohen, A. S.; Najarian, D. R.; Paulus, A.; Guttman, A.; Smith, J. A., *et al. Proc. Natl. Acad. Sci. U. S. A.* **1988**, *85*, 9660-9663.

(19) Zhu, M. D.; Hansen, D. L.; Burd, S.; Gannon, F. *J. Chromatogr.* **1989**, *480*, 311-319.

(20) Heiger, D. N.; Cohen, A. S.; Karger, B. L. *J. Chromatogr.* **1990**, *516*, 33-48.

(21) Ruizmartinez, M. C.; Berka, J.; Belenkii, A.; Foret, F.; Miller, A. W., *et al. Anal. Chem.* **1993**, *65*, 2851-2858.

(22) Grossman, P. D.; Soane, D. S. *Biopolymers* **1991**, *31*, 1221-1228.

(23) Gao, Q. F.; Yeung, E. S. *Anal. Chem.* **1998**, *70*, 1382-1388.

(24) Ogston, A. G. *Trans. Faraday Soc.* **1958**, *54*, 1754-1757.

(25) de Gennes, P. G. *J. Chem. Phys.* **1971**, *55*, 572-579.

(26) Lerman, L. S.; Frisch, H. L. *Biopolymers* **1982**, *21*, 995-997.

(27) Lumpkin, O. J.; Dejardin, P.; Zimm, B. H. *Biopolymers* **1985**, *24*, 1573-1593.

(28) Hervet, H.; Bean, C. P. *Biopolymers* **1987**, *26*, 727-742.

(29) Liu, M. S.; Amirkhanian, V. D. *Electrophoresis* **2003**, *24*, 93-95.

(30) Webster, J. R.; Burns, M. A.; Burke, D. T.; Mastrangelo, C. H. *Anal. Chem.* **2001**, *73*, 1622-1626.

(31) Kuo, J. S.; Kuyper, C. L.; P.B., A.; Fiorini, G. S.; Chiu, D. T. *Electrophoresis* **2004**, *25*, 3796 - 3804.

(32) Lee, D. S.; Chang, B. H.; Chen, P. H. *Sens. Actuators, B* **2005**, *107*, 872-881.

(33) Chen, X. J.; Ugaz, V. M. *Electrophoresis* **2006**, *27*, 387-393.

(34) Wang, S. L.; Fan, X. F.; Xu, Z. R.; Fang, Z. L. *Electrophoresis* **2005**, *26*, 3602-3608.

(35) Tseng, W. L.; Lin, Y. W.; Chen, K. C.; Chang, H. T. *Electrophoresis* **2002**, *23*, 2477-2484.

(36) Cohen, A. S.; Najarian, D. R.; Karger, B. L. *J. Chromatogr.* **1990**, *516*, 49-60.

(37) Slater, G. W.; Noolandi, J. *Phys. Rev. Lett.* **1985**, *55*, 1579-1582.

(38) Williams, B. A.; Vigh, G. *Anal. Chem.* **1996**, *68*, 1174-1180.

(39) Kim, J. B.; Otsuka, K.; Terabe, S. *J. Chromatogr. A* **2001**, *912*, 343-352.

(40) Hjerten, S. *J. Chromatogr.* **1985**, *347*, 191-198.

(41) Fung, E. N.; Yeung, E. S. *Anal. Chem.* **1995**, *67*, 1913-1919.

(42) Walbroehl, Y.; Jorgenson, J. W. *Anal. Chem.* **1986**, *58*, 479-481.

(43) Personal communication with Sigma-Aldrich Technical Service.

(44) Albarghouthi, M. N.; Barron, A. E. *Electrophoresis* **2000**, *21*, 4096-4111.

(45) Kotler, L.; He, H.; Miller, A. W.; Karger, B. L. *Electrophoresis* **2002**, *23*, 3062-3070.

(46) Sanders, J. C.; Breadmore, M. C.; Kwok, Y. C.; Horsman, K. M.; Landers, J. P. *Anal. Chem.* **2003**, *75*, 986-994.

(47) Lukacs, K. D.; Jorgenson, J. W. *J. High Resolut. Chromatogr.* **1985**, *8*, 407-411.

(48) Product manual for ϕX174 RF DNA/*Hae* III Fragments

CHAPTER SIX. Conclusions and Future Work

6.1 Conclusions

A number of novel detection schemes for fluorescence have been reported in this thesis. All were designed to illustrate the potential of reducing the size, complexity and cost of the light source without sacrificing sensitivity. The violet diode laser, having previously been used for the analysis of amino acids[1] and uroporphyrins,[2] was used in detecting myoglobin by a novel labelling scheme. While diode lasers offer a useful alternative to traditional lasers, the cost of research-grade diode lasers remains relatively high at several thousand dollars. As a further cost-saving measure, the use of LEDs was investigated. Standard LEDs with a 250 × 250 μm emitter deliver approximately 5 mW of light. The small emitter area allowed the light to be collimated and focussed with relatively high efficiency. Tight focussing of the light onto the capillary inner channel results in maximum use of the light available and avoids detector bandbroadening. The LEDs emission spectrum is polychromatic, and for most fluorophores the LED emits weakly at the detection wavelength. Scattering of the LED light at the detection wavelength can give a very high background signal, but this source of background signal can be strongly attenuated by placing a bandpass filter between the LED and the capillary. The bandpass filter is chosen to block LED light at the detection wavelength from reaching the capillary, thus reducing the background signal. High-quality bandpass filters are well worth the extra cost, especially for small Stokes-shift fluorophores, because high-quality filters have a steeper transition from blocking to transmitting. This

steeper transition allows for the use of wider bandwidth filters which are spectrally closer together. This then, allows more exctitation light to be passed and less scatter background to be transmitted.

The recent introduction of high-power LED packages appears to offer sufficient light output to achieve detection limits comparable to lasers. But the increased power of these LED packages stems from the use of a larger emitting chip: 680 × 680 μm for Cree LEDs (up to 350 mW) and 2 × 2 mm for Luxeon LEDs (up to 750 mW). This large emitting area limits the size to which the LED light can be focussed; a problem which is compounded by the highly divergent light output of these packages. Using an epi-fluorescence configuration removes the spatial constraints near the capillary, as only a single microscope objective is required. A high-power (63 ×), short working distance microscope objective allows the Luxeon LED to be focussed to approximately 150 μm, thus making use of significantly more light than was achieved using a 90-degree configuration. The high-power LED was shown to achieve limits of detection an order of magnitude higher than comparable laser-based detectors, with three orders of magnitude savings in cost. Thus, significant savings in space and cost can be achieved by using high-power LEDs rather than lasers.

6.2 Future Work

6.2.1 Instrument Refinements

A moderately high background signal was seen in all high-power LED work. As well, a noisy background signal was seen when using sheath flow detection (Section

4.3.3.3) or a polymeric sieving matrix (Section 5.3.4). The elevated, noisy background shows that the long-wavelength LED light is not completely attenuated by the excitation bandpass filter. Lowering the background signal would allow the PMT to operate at a higher bias, thus improving sensitivity. The addition of a second bandpass or shortpass filter in series with the excitation bandpass filter should help to reduce the scatter background signal. The emission spectrum of the high-power LED used throughout this thesis is centered at a shorter wavelength than the fluorescein excitation spectrum, which suggests that selecting an appropriate filter should be relatively straightforward. It becomes significantly more difficult to find an appropriate filter when the LED emission is centered at wavelengths longer than the fluorophore's excitation maximum (Section 3.3.6). Nonetheless, one should ensure that the newly added has sufficient blocking at the detection wavelength in order to maximally attenuate the background signal.

A second option is to digitally filter the signal to suppress a noisy background.[3] This noisy background was apparent when using a sieving matrix for CGE (see Figure 5.6). The spikes in the background signal are significantly sharper than the electrophoretic peaks, and a carefully chosen digital cutoff frequency could potentially remove these spikes from the background signal. This filtering would have no effect on the average value of the background signal.

6.2.2 Separation Improvements

The DNA separations presented in Chapter Five were not optimized. One possible cause for the low resolution obtained in Chapter Five is that all separations were performed at room temperature. The lack of capillary thermostatting used in our

instrument meant that literature conditions could not always be reproduced. For instance, PVP has been used at room temperature[4], 65 – 83 °C,[4] and with temperature gradients in the range of 61 – 74 °C.[5] POP-6™ is typically used at 42[6] to 50°C.[7] In contrast, HPC is usually used at room temperature.[8] Indeed the HPC sieving matrix was most successful in this work. Performing DNA separations at the elevated temperatures mentioned above has three advantages. First, a shift occurs in the length of the DNA chain at which biased reptation (see Section 5.1.5) becomes significant. At elevated temperatures, the onset of biased reptation occurs at higher molecular weight than at ambient temperature, extending the maximum length of DNA than can be separated. Second, elevated temperature removes secondary structure of the DNA polymer, which makes migration behaviour more predictable. Third, elevated temperature decreases the viscosity of the sieving matrix, which shortens the run time. Elevated temperature however, comes with two disadvantages: the pore structure of the sieving matrix is changed and the dynamic wall coating begins to desorb. The result is poor separation of short DNA fragments, and gradually increasing run times due to increasing eof, respectively.[9]

As it is not possible to re-create the capillary temperatures used in the aforementioned works, the use of sieving matrices other than cellulose derivatives might be met with limited success. A simpler separation mechanism is emerging which threatens to render polymeric sieving matrices obsolete. The use of end-labelled free solution electrophoresis (ELFSE)[10] makes it possible to separate DNA by size, in the absence of a sieving matrix. By attaching a monodisperse "drag-tag" to one[11] or both[12] ends of the DNA molecules, small molecules will experience a relatively large increase in their electrophoretic friction, while that of large DNA molecules will be relatively small.

Thus, a size-based separation of DNA can be achieved in free solution. While producing monodisperse, drag-tag labelled DNA is no simple task, performing the separations should be much simpler than traditional DNA separations using a sieving matrix.

6.2.3 Technological Developments

A deep-UV (nominally 190 – 290 nm) LED has recently become commercially available and has been used as a light source for fluorescence detection in CE.[13] The advantage of working in the deep-UV is that protein native fluorescence can be excited, thus eliminating any perturbations of the proteins caused by extrinsic fluorophores. While these deep-UV LEDs are available from 250 – 365 nm, they produce only 0.5 mW of power from a chip. This LED package actually contains two chips placed side-by-side. With a total chip area of 2.5 × 2.5 mm, the emitted power density is very low. With this LED, Sluszny *et al.* obtained a detection limit of 20 nM for conalbumin.[13] Until the emitted power of these chips is increased, the resulting limits of detection will remain poor. However, a potential improvement on the reported 20 nM LOD is the use of an excitation bandpass filter, which was not used by Sluszny *et al.* The authors justified this choice based on the manufacturer's claim that the LED emission at the tryptophan emission wavelength of 350 nm is 4000-fold less intense than at its peak wavelength. Nonetheless, the work in Chapter Three of this thesis has clearly shown that the use of an excitation filter is critical, and is therefore worth exploring.

A cost-saving measure is envisioned when working in the deep-UV: replacing the emission filter with a simple glass disc. Low-grade glass or Pyrex® absorb strongly in the deep-UV (Figure 6.1), making them long-pass filters. Glass, for instance, has 50%T

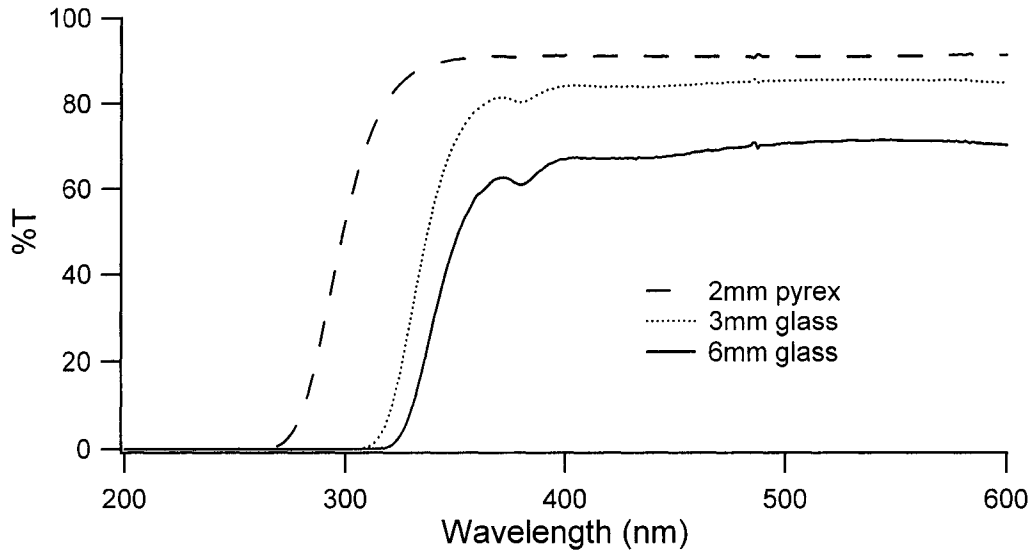

Figure 6.1 Transmission spectra of glass (3 and 6 mm thick) and Pyrex (2mm thick).

at 338 nm and reaching OD ≥ 4 for a disc approximately 3 mm thick. Thus, well-polished glass might effectively remove scattered LED light. As well, glass provides significantly higher transmission than the bandpass filters available at a detection wavelength of 350 nm (70 – 80%T compared to 25%T). Of course multiple discs can be combined to achieve sufficient blocking of LED light, at the expense of transmittance in the transmitting region. The Pyrex disc, although more transmissive at 350 nm, has a cut-off wavelength too close to the LED emission, and will not likely be effective as an emission filter.

6.2.4 Other Applications of LEDs

While the first quantum dots were multiple-layered materials,[14] the term quantum dot can now include particles made of a single semiconductor material. Quantum dots are nanometre-sized particles which, due to their size, exhibit quantum confinement. Quantum dots are fluorescent particles with very wide absorption spectra (deep-UV to visible) and often narrow emission spectra (~ 30 nm) which can be centered anywhere from 300 – 2500 nm.[15] Quantum dots have been exploited as Förster resonance energy transfer (FRET) donors for analytical applications such as DNA sensing.[16] A logical extension of this concept would be to use quantum dots as a FRET donor in four-colour detection for DNA sequencing. Due to the wide absorption spectra and large Stokes' shifts of quantum dots, they appear well-suited to excitation by LEDs. It might be possible to excite quantum dots with LED light that has not been passed through an excitation filter, thus preserving maximal excitation intensity. Ideally, the large Stokes' shift will ensure that no LED excitation light is transmitted toward the detector. While

not always a replacement for organic fluorophores, quantum dots are seen as a complementary technology.[17] In this case, the extremely high resistance to photobleaching would be useful with the high light intensity of a high-power LED that has not passed through an excitation filter.

Another fluorescent tool with broadband excitation is the molecule epicocconone, which was only recently isolated and characterized from the fungus *Epicoccum nigrum* (Figure 6.2).[18] Epicocconone has excitation maxima at 395 and 520 nm, and a broad emission maximum at 610 nm. As with quantum dots, epicocconone is a molecule that might easily be excited by an LED without prior spectral filtering due to the broad emission spectrum and large Stokes' shift. Alternatively, the emission maximum at 395 nm can easily be exploited by the 400 nm violet diode laser (Chapter Two). Epicocconone can be used to noncovalently stain proteins, producing mass detection limits of 100 pg.[19] This sensitivity is considerably better than when using the common protein stains: SYPRO™ dyes, silver staining, or Coomassie Brilliant Blue. Epicocconone is also fluorogenic, in that it is weakly fluorescent when present in water, but highly fluorescent in the presence of proteins or SDS. The protein staining is reversible in the presence of strong base or acid, which is compatible with Edman degradation for protein sequencing.[20]

In conclusion, growth in the solid-state lighting industry has given rise to LEDs which produce a remarkable amount of light. These LEDs are designed with quite different goals in mind than what is ideal for an analytical chemist. Nonetheless, LEDs designed for ambient lighting retain several properties of an "ideal" light source. Thus

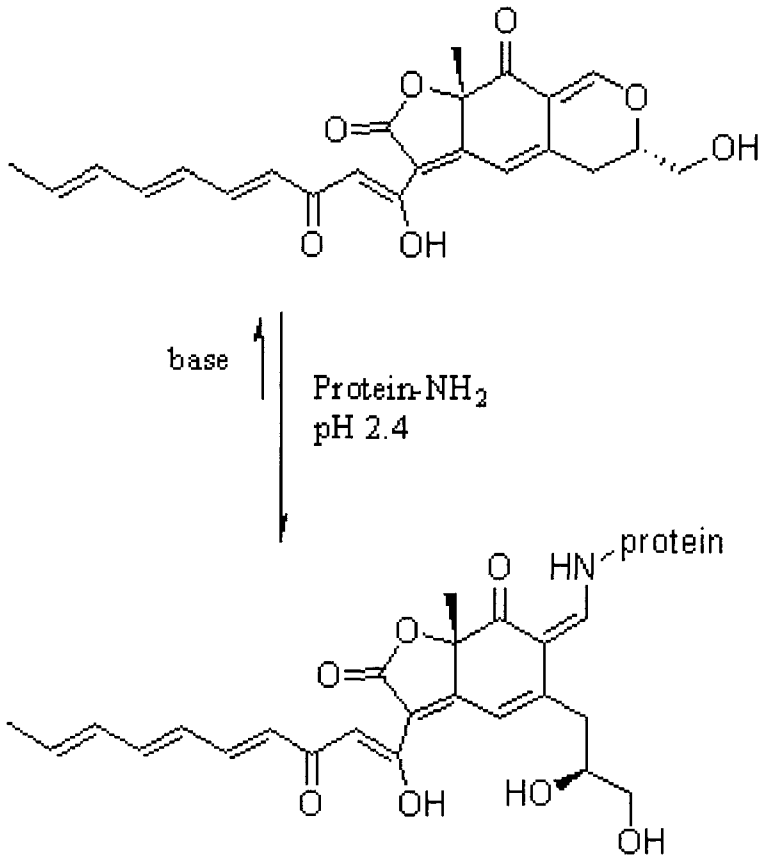

Figure 6.2 Reaction scheme for the reversible labelling of a protein amine group with epicocconone (top). The epicocconone-protein conjugate is most stable at pH 2.4.

for now, LEDs can be considered a "pretty good" light source for high-sensitivity measurements, with extremely low cost.

6.3 References

(1) Melanson, J. E.; Lucy, C. A. *Analyst* **2000**, *125*, 1049-1052.

(2) Melanson, J. E.; Lucy, C. A. *Electrophoresis* **2002**, *23*, 1689-1694.

(3) Chen, D. Y.; Dovichi, N. J. *Journal of Chromatography B-Biomedical Applications* **1994**, *657*, 265-269.

(4) Gao, Q. F.; Yeung, E. S. *Anal. Chem.* **1998**, *70*, 1382-1388.

(5) Gao, Q. F.; Pang, H. M.; Yeung, E. S. *Electrophoresis* **1999**, *20*, 1518-1526.

(6) Madabhushi, R. S. *Electrophoresis* **1998**, *19*, 224-230.

(7) Griess, G. A.; Hardies, S. C.; Serwer, P. *Electrophoresis* **2005**, *26*, 102-111.

(8) Sanders, J. C.; Breadmore, M. C.; Kwok, Y. C.; Horsman, K. M.; Landers, J. P. *Anal. Chem.* **2003**, *75*, 986-994.

(9) Wei, W.; Yeung, E. S. *J. Chromatogr. B* **2000**, *745*, 221-230.

(10) Volkel, A. R.; Noolandi, J. *Macromolecules* **1995**, *28*, 8182-8189.

(11) Won, J. I.; Meagher, R. J.; Barron, A. E. *Electrophoresis* **2005**, *26*, 2138-2148.

(12) Meagher, R. J.; McCormick, L. C.; Haynes, R. D.; Won, J. I.; Lin, J. S., *et al.* *Electrophoresis* **2006**, *27*, 1702-1712.

(13) Sluszny, C.; He, Y.; Yeung, E. S. *Electrophoresis* **2005**, *26*, 4197-4203.

(14) Reed, M. A.; Bate, R. T.; Bradshaw, K.; Duncan, W. M.; Frensley, W. R., *et al.* *Journal of Vacuum Science & Technology B* **1986**, *4*, 358-360.

(15) Yu, W. W.; Chang, E.; Drezek, R.; Colvin, V. L. *Biochem. Biophys. Res. Commun.* **2006**, *348*, 781-786.

(16) Zhang, C. Y.; Johnson, L. W. *Anal. Chem.* **2006**, *78*, 5532-5537.

(17) Cottingham, K. *Anal. Chem.* **2005**, *77*, 354A-357A.

(18) Bell, P. J. L.; Karuso, P. *Journal of the American Chemical Society* **2003**, *125*, 9304-9305.

(19) Mackintosh, J. A.; Choi, H. Y.; Bae, S. H.; Veal, D. A.; Bell, P. J., *et al. Proteomics* **2003**, *3*, 2273-2288.

(20) Coghlan, D. R.; Mackintosh, J. A.; Karuso, P. *Organic Letters* **2005**, *7*, 2401-2404.

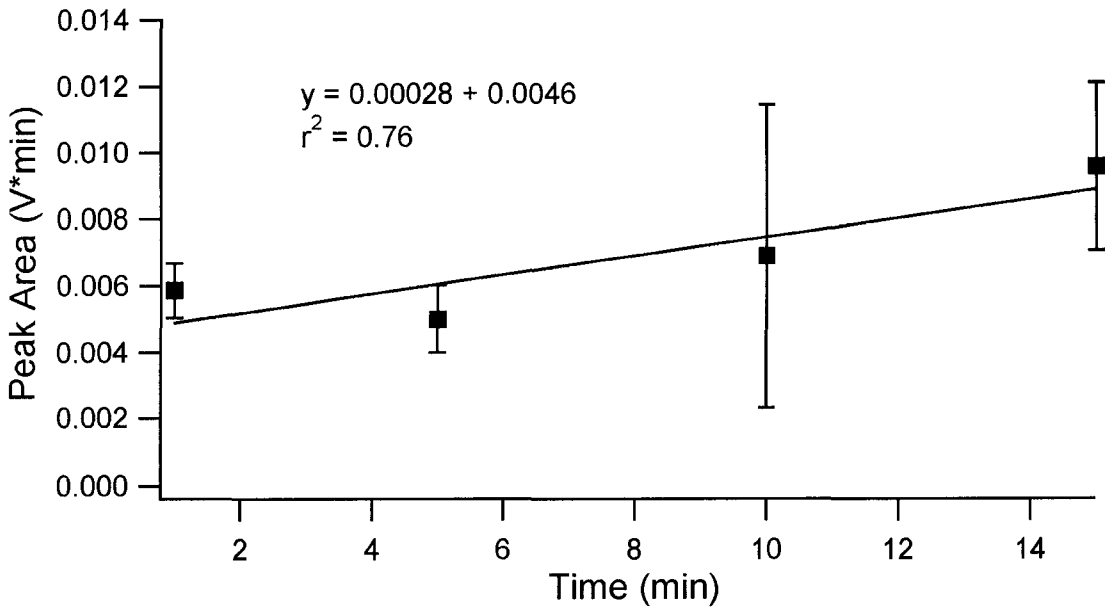

Appendix 1. Effect of urea denaturation time on myoglobin labelling efficiency. Myoglobin was labelled with PPIX by urea denaturation as described in Section 2.2.3.2 and analyzed by CE-LIF as in Section 2.2.3.4. The data is fit to a line using a linear least-squares program. Error bars represent the 95% confidence intervals for three trials.

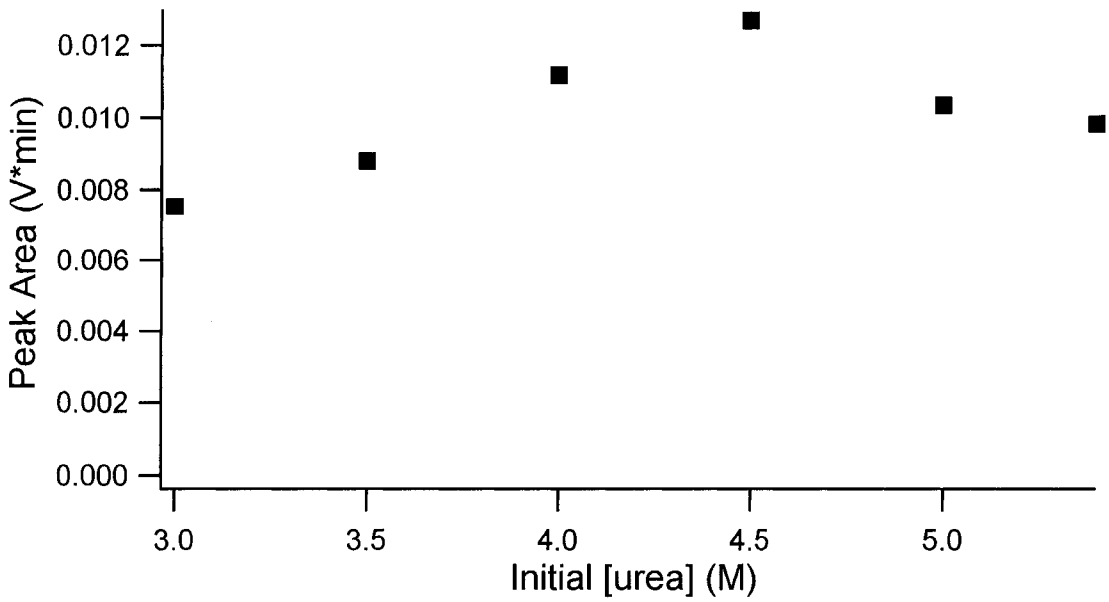

Appendix 2. Effect of initial urea concentration on myoglobin labelling efficiency. Myoglobin was labelled with PPIX by urea denaturation as described in Section 2.2.3.2 and analyzed by CE-LIF as in Section 2.2.3.4.

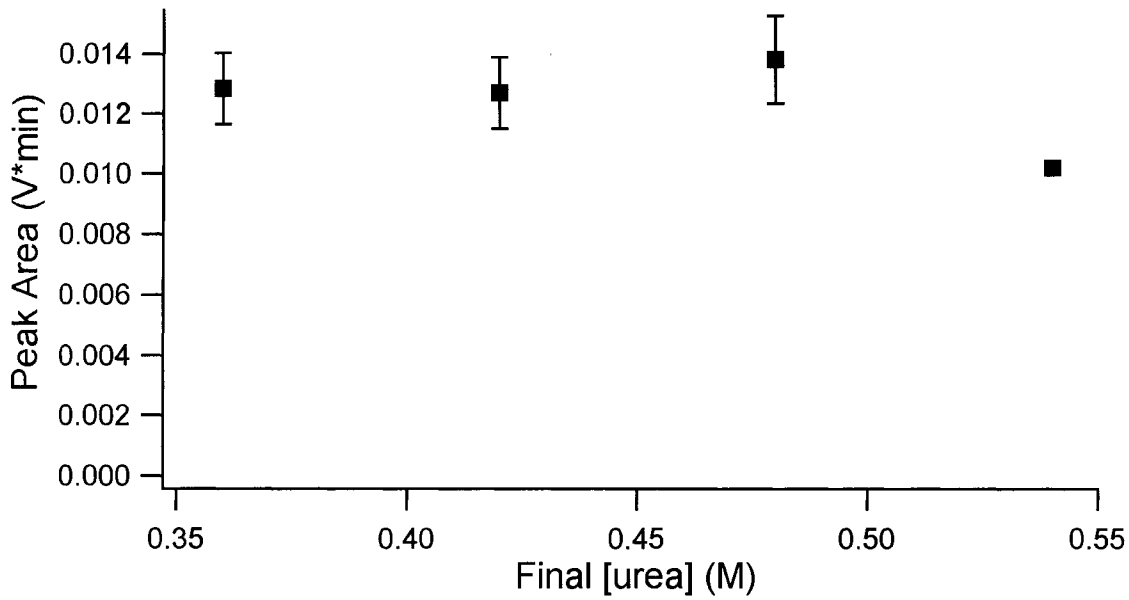

Appendix 3. Effect of total amount of urea (expressed as its final solution concentration) on myoglobin labelling efficiency. Myoglobin was labelled with PPIX by urea denaturation as described in Section 2.2.3.2 and analyzed by CE-LIF as in Section 2.2.3.4. Error bars represent one standard deviation for three trials.

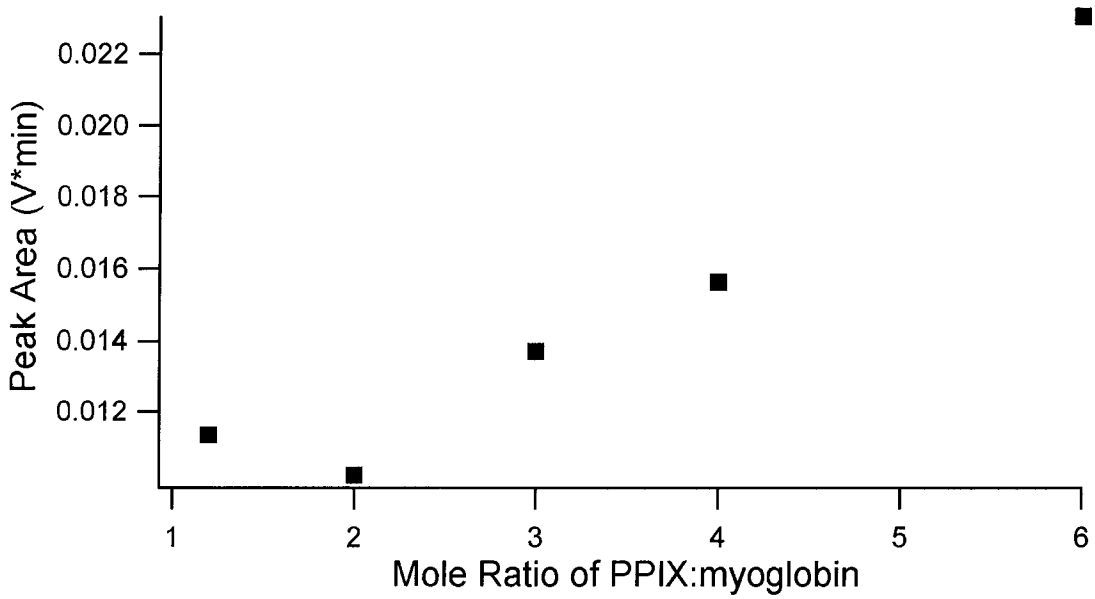

Appendix 4. Effect of a moderate excess of PPIX on the labelling efficiency of myoglobin. Myoglobin was labelled with PPIX by urea denaturation as described in Section 2.2.3.2 and analyzed by CE-LIF as in Section 2.2.3.4.

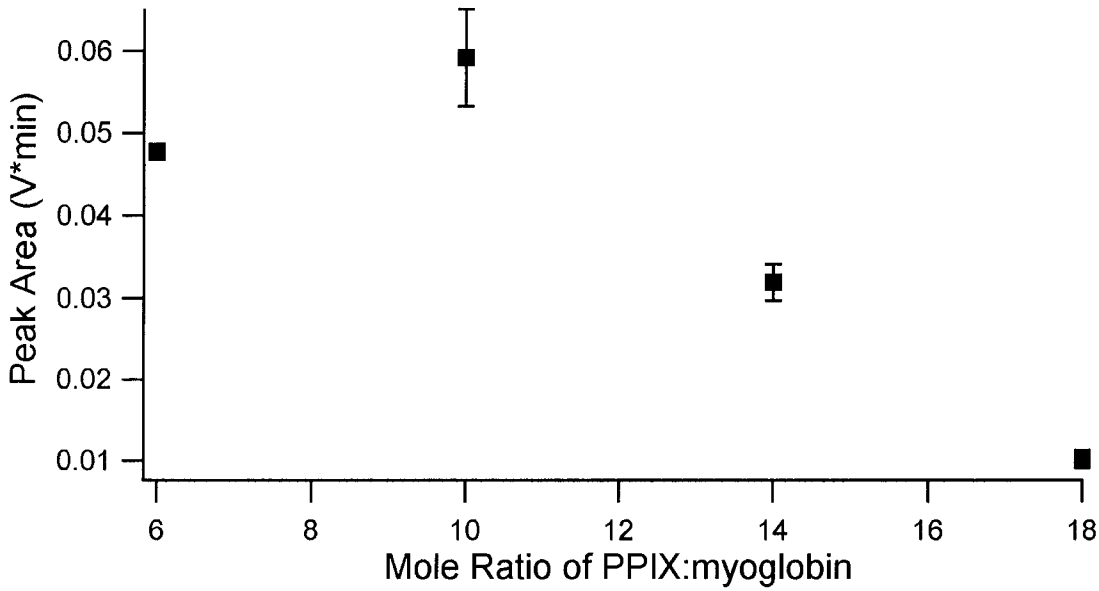

Appendix 5. Effect of a large excess of PPIX on myoglobin labelling efficiency. Myoglobin was labelled with PPIX by urea denaturation as described in Section 2.2.3.2 and analyzed by CE-LIF as in Section 2.2.3.4.

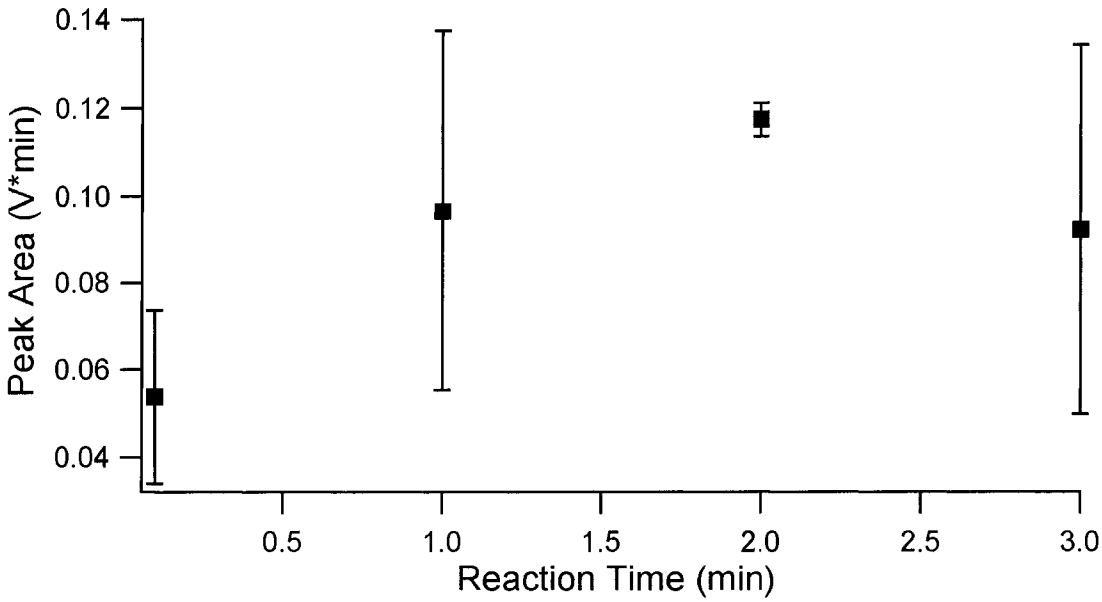

Appendix 6. Effect of reaction time on myoglobin labelling efficiency. Myoglobin was labelled with PPIX by low-pH denaturation as described in Section 2.2.3.2 and analyzed by CE-LIF as in Section 2.2.3.4. Error bars represent the standard deviation of two trials.

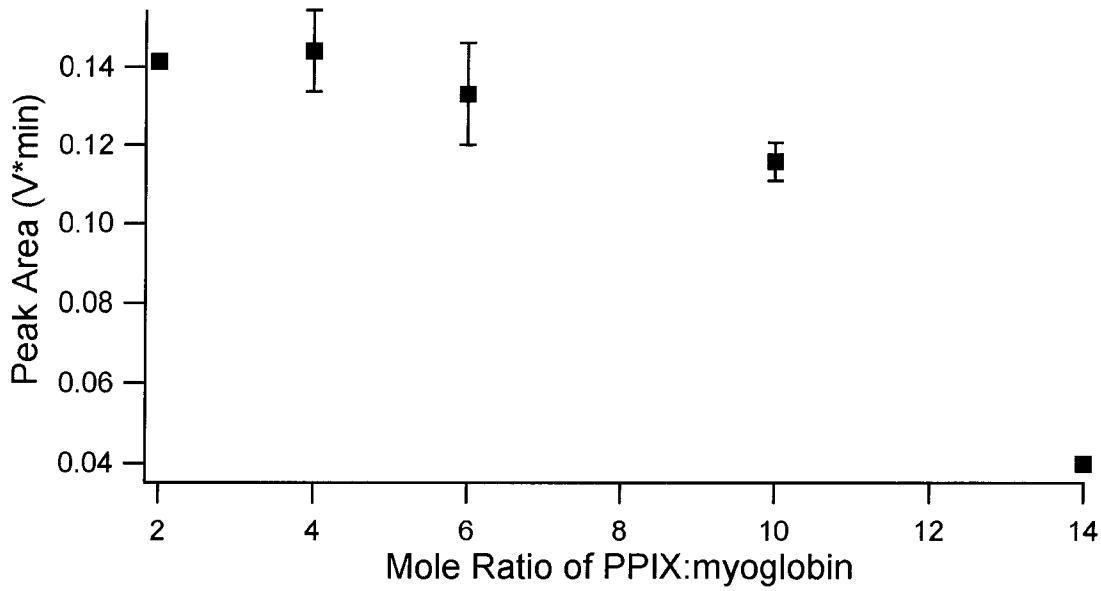

Appendix 7. Effect of mole excess of PPIX on myoglobin labelling efficiency. Myoglobin was labelled with PPIX by low-pH denaturation as described in Section 2.2.3.2 and analyzed by CE-LIF as in Section 2.2.3.4. Error bars represent the standard deviation of two trials.

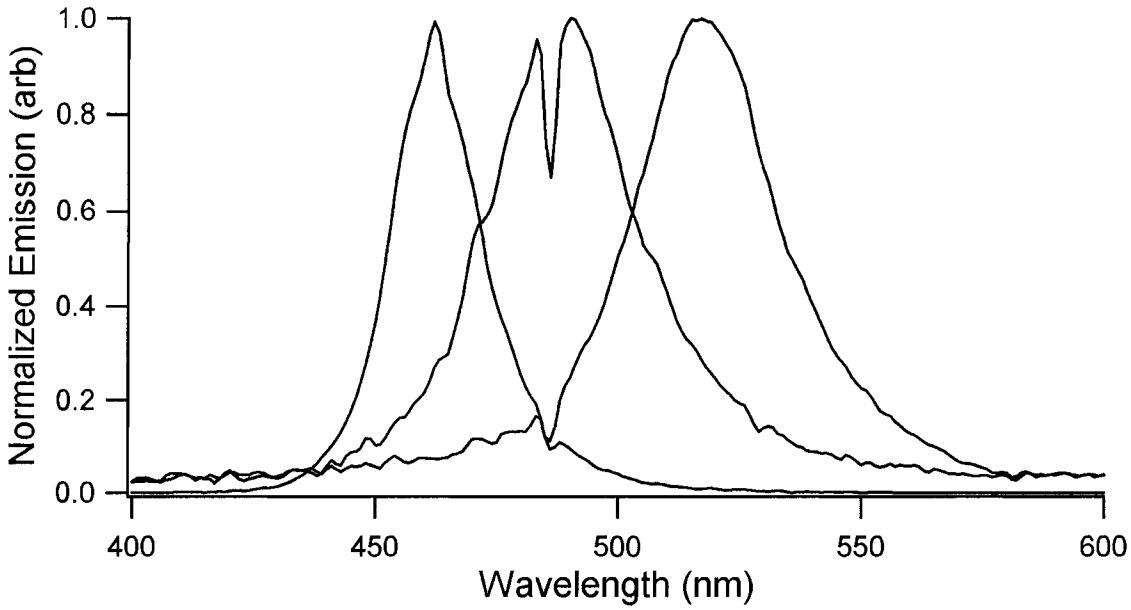

Appendix 8. Normalized spectra of three LEDs used in Chapter 3. All 490 nm LEDs purchased displayed the split emission peak, seen here. Data was smoothed using 2nd order Savitzky-Golay smoothing on 5 points.

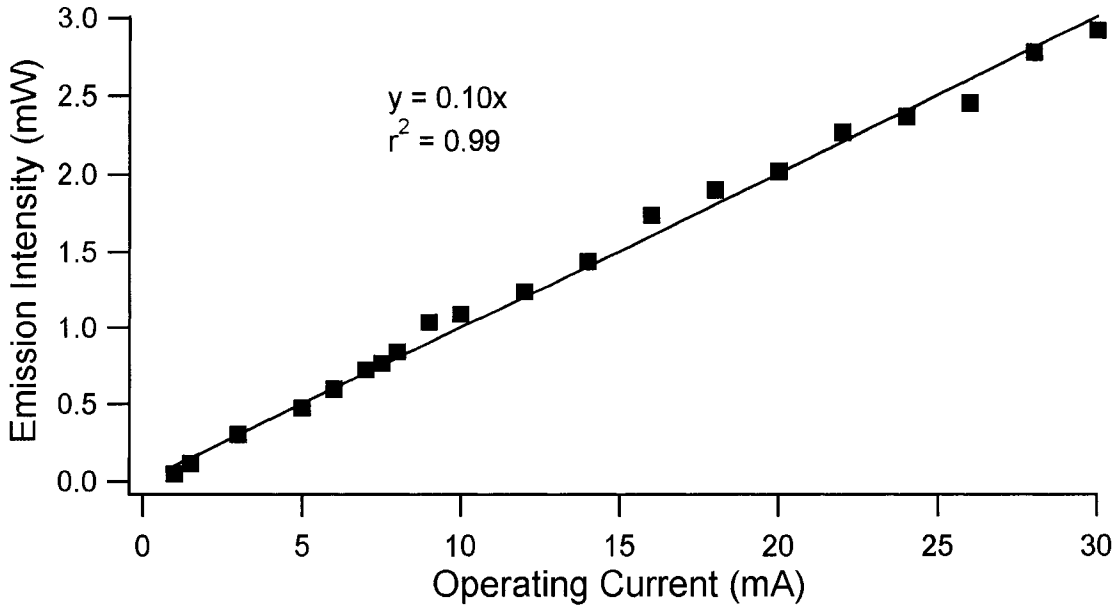

Appendix 9. Emission as a function of operating current for a 470 nm LED. The emission intensity was measured with a LaserCheck power meter. The data is fit to a line using a linear least-squares program.

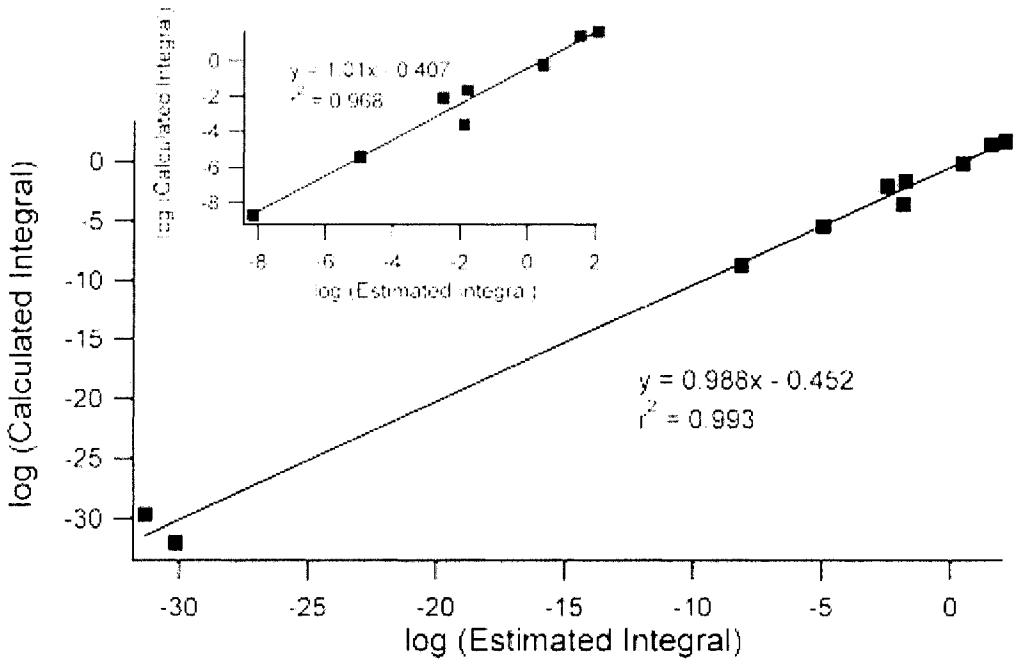

Appendix 10. Correlation between the mathematically calculated and graphically estimated methods of determining filter crosstalk. The inset shows only the upper portion of the graph with linear regression for only the data displayed. The data is fit to a line using a linear least-squares program.

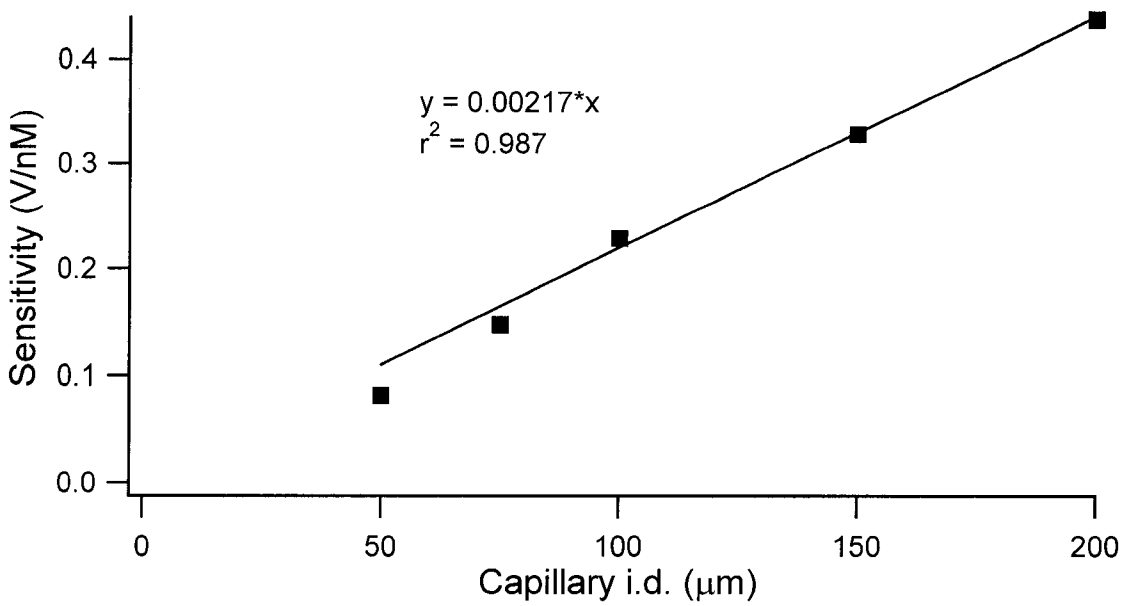

Appendix 11. Effect of capillary inner diameter on sensitivity. Sensitivity is taken as the slope of a calibration curve for each optical configuration. For each calibration curve, a different capillary i.d. was used, but not the pinhole of the collection optics was held at 1.0 mm. Increasing the capillary i.d. but not the collection pinhole allows for only one-dimensional gains in the collected fluorescence signal. The data is fit to a line using a linear least-squares program.

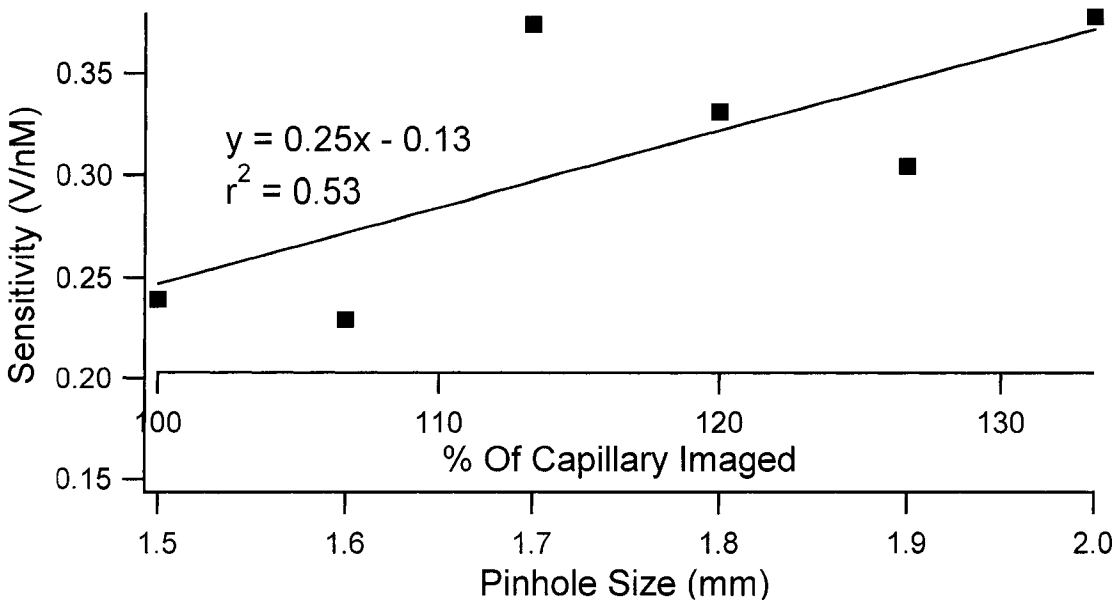

Appendix 12. Relationship between using an excessively large pinhole and sensitivity, on a 75 μm i.d. capillary. Calibration curves were constructed for each pinhole size to determine the sensitivity. While sensitivity is weakly correlated with using a larger pinhole, limits of detection and dynamic range suffer due to excess background signal. The data is fit to a line using a linear least-squares program.

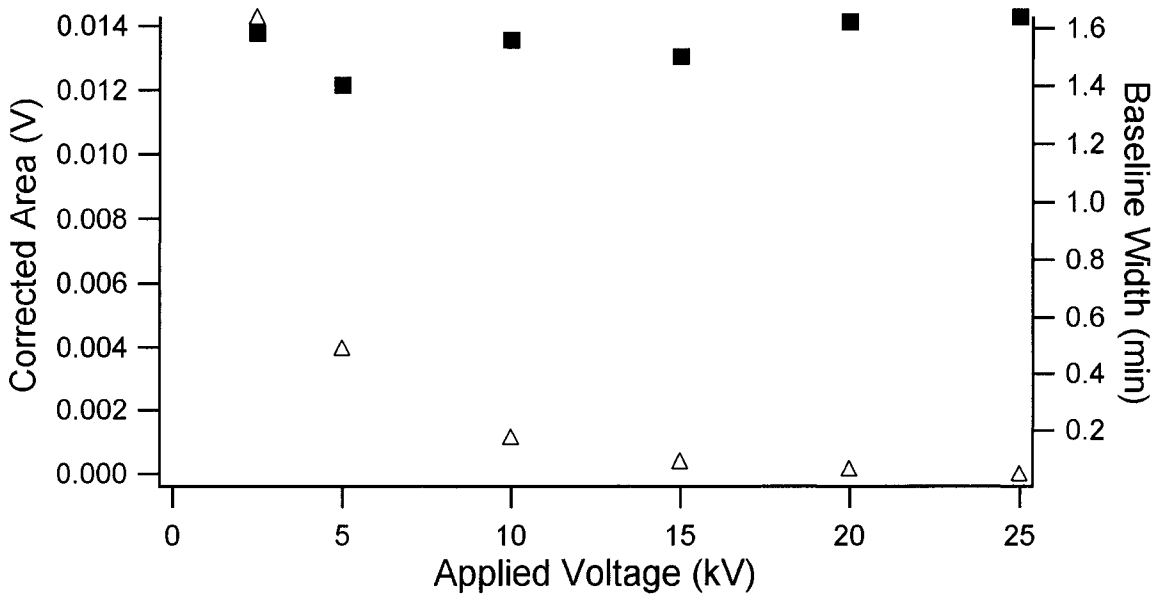

Appendix 13. Effect of analyte velocity on peak area. Slower separations cause fluorescein to spend more time in the excitation beam, but no decrease in peak area is observed. Filled squares (■) represent corrected peak area, while open triangles (△) represent the peak width at baseline.

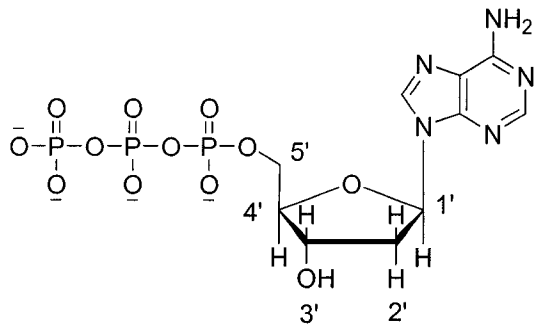

dATP

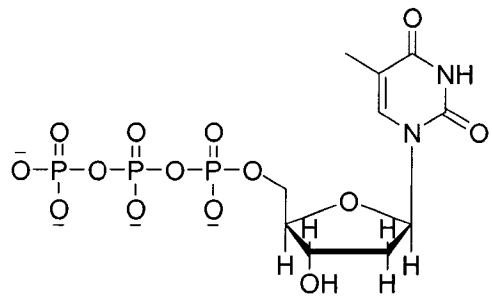

dTTP

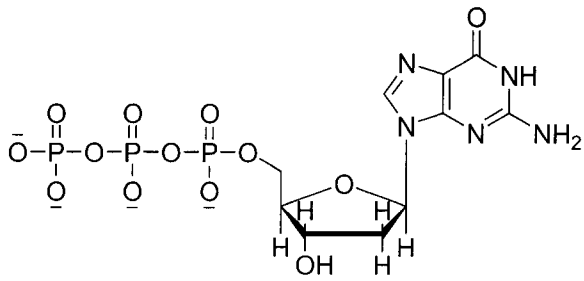

dGTP

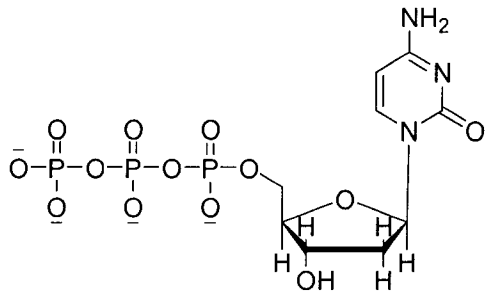

dCTP

Appendix 14. Structure of the four 2' deoxynucleotide triphosphates. Dideoxynucloetides, used to terminate the polymerase reaction, lack the hydroxide group at the 3' position. In a DNA chain, the nucleotides are held together though phosphodiester bonds linking the 3' and 5' postitions of the (deoxy)ribose moiety. Consequently, a DNA chain has a 3' and a 5' end.